

DELAYED NEUTRINO-DRIVEN SUPERNOVA EXPLOSIONS AIDED BY THE STANDING ACCRETION-SHOCK INSTABILITY

A. MAREK¹ AND H.-TH. JANKA¹

Draft version November 14, 2008

ABSTRACT

We present two-dimensional hydrodynamic simulations of stellar core collapse and develop the framework for a detailed analysis of the energetic aspects of neutrino-powered supernova explosions. Our results confirm that the neutrino-heating mechanism remains a viable explanation of the explosion of a wider mass range of supernova progenitors with iron cores, but the explosion sets in later and develops differently than thought so far. The calculations were performed with an energy-dependent treatment of the neutrino transport based on the “ray-by-ray plus” approximation, in which the neutrino number, energy, and momentum equations are closed with a variable Eddington factor obtained by iteratively solving a model Boltzmann equation. We focus here on the evolution of a $15 M_{\odot}$ progenitor and provide evidence that shock revival and an explosion are initiated at about 600 ms after core bounce, powered by neutrino energy deposition. This is significantly later than previously found for an $11.2 M_{\odot}$ star, for which we also present a continuation of the explosion model published by Buras et al. The onset of the blast is fostered in both cases by the standing accretion shock instability (SASI). This instability exhibits highest growth rates for the dipole and quadrupole modes, which lead to large-amplitude bipolar shock oscillations and push the shock to larger radii, thus increasing the time accreted matter is exposed to neutrino heating in the gain layer. As a consequence, also convective overturn behind the shock is strengthened, which otherwise is suppressed or damped because of the small shock stagnation radius. When the explosion sets in, the shock reveals a pronounced global deformation with a dominant dipolar component. In both the $11.2 M_{\odot}$ and $15 M_{\odot}$ explosions long-lasting equatorial downflows supply the gain layer with fresh gas, of which a sizable fraction is heated by neutrinos and leads to the build-up of the explosion energy of the ejecta over possibly hundreds of milliseconds. A “soft” nuclear equation of state that causes a rapid contraction and a smaller radius of the forming neutron star and thus a fast release of gravitational binding energy, seems to be more favorable for the development of an explosion. Rotation has the opposite effect because in the long run it leads to a more extended and cooler neutron star and thus lower neutrino luminosities and mean energies and overall less neutrino heating. Neutron star g-mode oscillations, although we see their presence, and the acoustic mechanism play no important role in our simulations. While numerical tests show that our code is well able to follow also large-amplitude core g-modes if they are instigated, the amplitude of such oscillations remains small in our supernova runs and the acoustic energy flux injected by the ringing neutron star is minuscule compared to the neutrino energy deposition.

Subject headings: supernovae — hydrodynamics — neutrinos

1. INTRODUCTION

The physical processes that start the explosion of massive stars are still not well understood, although this is of crucial importance for predicting supernova and remnant properties, nucleosynthesis conditions and yields, and the observable signals from supernovae like neutrinos and gravitational waves. Neutrinos are thought to be the main agent of energy transport and energy loss from collapsing stars, an expectation that was spectacularly verified by the detection of two dozen neutrinos in connection with Supernova 1987A. Colgate & White (1966) suggested already 40 years ago that the intense flux of neutrinos radiated from the nascent neutron star might deposit the energy needed to reverse the stellar collapse. The detailed physics of this neutrino-driven mechanism, however, was worked out only later, based on numerical

results of Wilson (1985). Bethe & Wilson (1985) showed that neutrinos deposit their energy behind the stalled supernova shock front mainly by the absorption of ν_e and $\bar{\nu}_e$ on free neutrons and protons, respectively, which are the most abundant nuclear species in the postshock layer. Provided the neutrino luminosities are sufficiently large, this energy input was found to be so strong that the stagnating shock can be “revived” and thus accelerates outward to propagate through the overlying, still collapsing layers of the star.

The viability of this neutrino-heating mechanism has recently been demonstrated for stars near the lower mass end of supernova progenitors for stiff as well as soft nuclear equations of state (Kitaura, Janka, & Hillebrandt 2006; Janka, Marek, & Kitaura 2007; Janka et al. 2008). The investigated progenitor with a main-sequence mass of $8.8 M_{\odot}$ (Nomoto 1984, 1987) can be considered as representative of the $\sim 8\text{--}10 M_{\odot}$ range. The cores of such stars consist of oxygen, neon, and magnesium instead of iron and possess an extremely steep density gradient at their surface. The latter fact leads to a very rapid de-

Electronic address: amarek@mpa-garching.mpg.de
Electronic address: thj@mpa-garching.mpg.de

¹ Max-Planck-Institut für Astrophysik, Karl-Schwarzschild-Str. 1, D-85748 Garching, Germany

crease of the mass accretion rate onto the forming neutron star, enabling the stalled shock to continue its expansion. This creates favorable conditions for neutrino energy deposition, thus allowing a neutrino-driven baryonic wind to be launched, which is sufficiently powerful to eject the gravitationally loosely bound outer layers of the star. The new results confirm qualitatively previous simulations by Mayle & Wilson (1988), although the more sophisticated treatment of the neutrino transport in the new models, which were computed with the PROMETHEUS-VERTEX code, leads to the predictions of a lower explosion energy and a lower neutron excess in the ejecta.

In case of more massive progenitors, Wilson & Mayle (1988, 1993) could obtain explosions only by assuming that the neutrino luminosities and thus the neutrino energy deposition behind the stalled shock were boosted by enhanced neutrino transport in the neutron star. According to Wilson & Mayle this could happen, e.g., because of the presence of neutron-finger instabilities below the neutrinosphere. The existence of neutron-finger unstable conditions, however, was repudiated on grounds of a detailed analysis of the neutrino transport conditions in supernova cores (Bruenn & Dineva 1996). Nevertheless, numerical simulations (Buras et al. 2006b; see also Dessart et al. 2006) showed that Ledoux convection occurs inside the proto-neutron star and later than about 200 ms after bounce leads to accelerated lepton number and energy losses because of significantly increased muon and tau neutrino luminosities. The fluxes of ν_e and $\bar{\nu}_e$, which are mostly responsible for the shock heating, however, hardly change on a post-bounce timescale of some hundred milliseconds, and the mean energies of the radiated neutrinos and antineutrinos of all flavors even decrease compared to models that ignore convection.

A potentially stronger multi-dimensional effect that is clearly supportive for delayed shock revival, was discovered to be convective overturn in the layer behind the stagnant shock. In this region neutrino heating tends to create a negative entropy gradient, because the energy deposition is maximal just outside of the gain radius (Herant et al. 1994; Burrows, Hayes, & Fryxell 1995; Janka & Müller 1996). Cooler matter that is accreted by the shock is carried in narrow downdrafts closer to the gain radius, where it readily absorbs energy from the neutrinos. At the same time, heated matter with its higher entropy becomes buoyant and starts rising and expanding, thus reducing energy loss by the reemission of neutrinos and pushing the shock farther out. Convective overturn therefore improves the efficiency of the neutrino energy transfer because it allows more matter to be exposed to strong heating near the gain radius. Effectively this means that the mass in the gain layer grows and that gas stays there for a longer time. This is reflected by an increase of the mean timescale τ_{adv} needed by accreted matter to move inward from the shock to the gain radius. A larger value of τ_{adv} implies that the ratio of the advection timescale to the neutrino-heating timescale, τ_{heat} , gets closer to unity, which is a necessary condition for a model to approach an explosion (see the analysis in Buras et al. 2006b; Thompson, Quataert, & Burrows 2005; Murphy & Burrows 2008).

Convection in the flow between shock and gain layer, however, is subject to strong damping because the gas

is falling rapidly and the time for seed perturbations to grow is therefore short until the gas crosses the gain radius and reaches the Ledoux-stable cooling region (Foglizzo, Scheck, & Janka 2006). Convective activity is therefore *not* able to develop in the gain layer despite the negative entropy gradient there, unless the initial density perturbations are sufficiently large or the ratio of advection timescale to convective growth timescale, τ_{conv} , exceeds a critical value (for more details, see Scheck et al. 2008). Two-dimensional (2D) supernova simulations (Buras et al. 2006a,b) with the PROMETHEUS-VERTEX code, employing a sophisticated energy-dependent description of the neutrino transport, indeed show that convective overturn in the hot-bubble region becomes much less vigorous than in previous multi-dimensional models with a grey neutrino diffusion scheme (e.g., Herant et al. 1994; Burrows et al. 1995; Fryer 1999; Fryer & Warren 2002, 2004), mainly because the accretion shock in the new models lingers at rather small radii and the correspondingly high infall velocities in the postshock region are unfavorable for the growth of convection. Scheck et al. (2008), performing parametric hydrodynamic studies of the post-bounce accretion phase in collapsing stellar cores, found that convection is suppressed when (i) the neutrino heating is too weak to produce a steep entropy gradient behind the shock, or (ii) the rapid contraction of the nascent neutron star leads to shock retraction and thus causes very short infall timescales of the gas between shock and gain radius.

In such a situation, however, the standing accretion shock instability (SASI; Blondin, Mezzacappa, & DeMarino 2003), which is a generic hydrodynamic instability of the shocked accretion flow to non-radial deformation modes, can exhibit particularly large growth rates (cf. Scheck et al. 2008) and becomes the dominant multi-dimensional phenomenon to initiate shock expansion. This was seen in the studies by Scheck et al. (2008) and is confirmed by the linear stability analysis of Yamasaki & Yamada (2007). The SASI stimulates large-amplitude bipolar shock oscillations, which create strong entropy variations in the postshock flow and thus trigger violent secondary convection. This helps pushing the stalled shock to larger radii and therefore stretches the time accreted matter is exposed to neutrino heating in the gain layer, establishing healthy conditions for the success of the neutrino-driven mechanism.

Such a decisive role of the SASI was indeed observed in case of an $11.2 M_{\odot}$ progenitor, whose collapse and explosion were simulated with the PROMETHEUS-VERTEX code (Buras et al. 2006b). Only when the setup of the numerical grid did not prohibit the growth of the lowest (dipolar and quadrupolar) SASI modes², which have the largest growth rates, could an explosion be obtained. Convection alone was too weak to yield sufficient support for the neutrino-heating mechanism. Instead it was the SASI in the first place which pushed the shock farther out and helped to bring the ratio of advection timescale to neutrino-heating timescale closer to the critical value of unity, which is necessary for reversing accretion to ex-

² In previous simulations with failed explosions (Buras et al. 2003a) the computational volume was constrained to a lateral wedge of 90 degrees ($\pm 45^\circ$) around the equatorial plane, using periodic boundary conditions. This setup prevented the occurrence of the dipole and quadrupole SASI modes.

plosion.

The underlying physical mechanism that is responsible for the SASI phenomenon is still controversial and currently a matter of vivid debate. Fogliizzo et al. (2007) explain the SASI by an advective-acoustic cycle (see also Fogliizzo 2001, 2002, 2008). This interpretation is in agreement with many properties of the instability observed in the hydrodynamic simulations of Scheck et al. (2008) and of Ohnishi, Kotake, & Yamada (2006). In contrast, Blondin & Mezzacappa (2006) and Blondin & Shaw (2007) advocate a purely acoustic cycle as the cause of the low-mode SASI and see this hypothesis supported by their numerical studies.

In this paper we will present evidence that the SASI-aided neutrino-heating mechanism may initiate an explosion not only in the case of an $11.2 M_{\odot}$ progenitor as recently seen by Buras et al. (2006), but in a wider mass range of progenitor stars. We study here a $15 M_{\odot}$ model (s15s7b2 from Woosley & Weaver 1995) which is frequently used in previous and present core-collapse studies because it can be considered as representative of stars in a larger mass interval. Stellar evolution calculations by Woosley, Heger, & Weaver (2002), for example, produced a very similar core structure also for other supernova progenitors up to about $20 M_{\odot}$ (see model s20.0 in Figs. A.2 and A.3 of Buras et al. 2006b). We discuss results of a 2D simulation in which a modest amount of rotation was assumed and which develops an explosion at 600 ms after core bounce, and compare it with non-exploding spherically symmetric (1D) simulations on the one hand, and 2D models without rotation on the other, in which two different equations of state (EoSs) for supernova matter are used, namely the Lattimer & Swesty (1991) EoS with a soft nuclear phase and the Hillebrandt, Wolff, & Nomoto (1984; see also Hillebrandt & Wolff 1985) EoS with a significantly stiffer nuclear phase (Hillebrandt 1994). Both are consistent with current neutron star mass determinations but the former leads to significantly more compact proto-neutron stars than the latter. The rotating pre-collapse iron core has a spin period of about 12 seconds. This is roughly a factor of ten more rapid than predicted by recent stellar evolution models including magnetic fields (Heger, Woosley, & Spruit 2005), but considerably slower than necessary for magnetohydrodynamics to be important in triggering the explosion, which requires pre-collapse spin periods of 2–3 seconds (Burrows et al. 2007a, Thompson et al. 2005).

We have also evaluated our simulations for the presence of gravity waves in the nascent neutron star. Burrows et al. (2006, 2007b) found in their 2D supernova models that the anisotropic accretion flow (as a consequence of the SASI) excited the neutron star to vigorous g-mode oscillations, in particular also the dipole ($l = 1$) mode. Later than about one second after bounce, the amplitude of these oscillations became very large (about 3 km) at the neutron star surface and the neutron star as a whole showed a large-amplitude periodic displacement along the z -axis of the numerical grid (Burrows et al. 2007c). As a consequence, a sizable acoustic energy flux was driven into the surrounding gas and was transporting a significant amount of acoustic energy to the stalled supernova shock. Burrows et al. did not find any neutrino-driven explosions in their models. However, at

late times (typically at $t > 1$ s after bounce), and therefore much later than the shock is revived by the neutrino-heating mechanism in the $11.2 M_{\odot}$ simulation of Buras et al. (2006b) and in the $15 M_{\odot}$ model discussed here, the acoustic energy flux caused by the core g-mode oscillations became dominant compared to neutrino heating and was able to cause an explosion. In our simulations the g-mode oscillations of the newly formed neutron star have always such small amplitudes that the acoustic energy input to the developing blast is negligible compared to neutrino energy deposition. In order to figure out whether our neutrino-hydrodynamics code is able to deal with this potentially important physical effect, we have also performed numerical tests. These demonstrate that our code is well able to track large-amplitude g-modes, also of dipole character, if such modes are excited in the neutron star core. We do not find any reason why our third-order hydrodynamics scheme with the chosen numerical resolution should not be able to follow the long-term excitation of neutron star oscillations by anisotropic accretion and turbulence in the SASI region between neutron star and shock front. Whether the excitation could be more efficient at times later than currently followed in our simulations (at most about 630 ms after bounce) remains unanswered and must be left for future exploration.

The reason why Burrows et al. (2006, 2007b) did not see any neutrino-driven explosions, which is in contrast to our findings, is not clear. However, the numerical approaches of both groups and the included physics are different in many aspects, and therefore it is not astonishing that for example the rate of neutrino energy deposition behind the supernova shock differs significantly between the calculations. While our “ray-by-ray plus” treatment of neutrino transport is highly sophisticated in dealing with the energy dependence of the problem but describes its dependence on the polar angle only approximately, Burrows et al. applied a 2D neutrino diffusion scheme, in which the energy dependence was only incompletely taken into account, because energy-bin coupling was ignored and Doppler effects due to the motion of the stellar fluid were neglected. In addition, the Tucson collaboration made use of a different numerical method to solve the hydrodynamics equations, e.g. the gravitational force was implemented in the momentum equation in an uncommon, momentum-conserving way. In their VULCAN code they employed a polar grid only in the outer regions of the computational volume but cartesian coordinates in the central part. They performed their simulations with the nuclear EoS of Shen et al. (1998), which is significantly stiffer than the Lattimer & Swesty (1991) EoS, though fairly similar to the Hillebrandt & Wolff EoS (Marek et al., in preparation; see also Janka et al. 2007). Moreover, their models were computed with purely Newtonian gravity, whereas a significantly stronger relativistic gravitational potential according to Marek et al. (2006) is applied in our models.

In fact, Newtonian 2D simulations in which the confluence of neutrino heating, the SASI, and nuclear burning produced explosions of 11 and $15 M_{\odot}$ progenitors, have recently been reported by Bruenn et al. (2006) and Mezzacappa et al. (2007) and seem to support the successful shock revival found in an $11.2 M_{\odot}$ star by Buras et al. (2006b). All these results were obtained with the EoS of

Lattimer & Swesty (1991). Like Buras et al. (2006b), the Oak Ridge group employed for the neutrino transport in two dimensions the “ray-by-ray-plus” approximation to deal with the lateral dimension. Their transport scheme, however, was based on a flux-limited diffusion description, in which the energy-dependence of the transport was treated in full detail. We consider the discrepant results obtained by the Tucson and Oak Ridge collaborations as additional motivation for us to contribute to the discussion by presenting our current simulations in this publication.

The paper is structured as follows: In Sect. 2.1 we give a brief summary of the numerical scheme and physics input used in the presented simulations, an overview of which follows in Sect. 2.2. Section 3 contains our results. For reference, we present in Sect. 3.1 results of our 1D simulations for the two employed nuclear EoSs, then describe the dynamical evolution of our exploding model in Sect. 3.2, compare the different computational runs in Sect. 3.5, and discuss our neutrino results in Sect. 3.6. An analysis of neutron star g-modes including numerical tests is presented in Sect. 4. In Sect. 5 we summarize our findings and draw conclusions.

2. METHODS AND MODELS

In this section we briefly summarize the basic properties of our numerical code and the input physics used in this work. We then give a compilation of the core-collapse simulations whose results are described afterwards.

2.1. Numerical approach and input physics

The core-collapse and post-bounce calculations presented in this work are performed with the PROMETHEUS-VERTEX neutrino-hydrodynamics code, details of which were published by Rampp & Janka (2002) and Buras et al (2006a). The code module that integrates the nonrelativistic hydrodynamics equations is a conservative and explicit Eulerian implementation of a Godunov-type scheme with higher-order spatial and temporal accuracy. The self-gravity of the stellar gas is treated in an approximation to general relativity, in which the monopole term of the Newtonian potential is replaced by an effective relativistic scalar potential that was constructed from close comparison of the Newtonian and relativistic equations of motion (for details, see Marek et al. 2006). For this effective relativistic monopole potential we consider the Cases A and R of the Marek et al. paper. The higher-order terms of the gravitational potential are taken as solutions of the Poisson equation for the two-dimensional gas distribution (see Müller & Steinmetz 1995).

The time-implicit transport routine solves the moment equations of neutrino number, energy, and momentum in spherical symmetry, employing a variable Eddington factor for closing the set of equations (Rampp & Janka 2002). The closure factor is obtained from a simplified Boltzmann equation, whose integro-differential character is tackled by iterating the coupled system of Boltzmann and moment equations until convergence is achieved. Our treatment of the neutrino transport and of neutrino-matter interactions is energy dependent and includes the full redistribution of neutrinos in energy and momentum space by scattering reactions with electrons, positrons,

and nucleons. Effects caused by the motion of the stellar fluid are taken into account as well as general relativistic redshifting and time dilation. In two spatial dimensions the transport is based on the “ray-by-ray plus” approximation, in which spherically symmetric transport problems are solved for the conditions present in the radial “rays” corresponding to the different lateral bins of the polar grid. This means that we assume the local neutrino phase-space distribution to be axially symmetric around the radial direction and thus to depend only on one instead of two angles, as a consequence of which the neutrino pressure tensor remains diagonal and the lateral component of the neutrino flux vanishes. This simplifies the transport from a five dimensional, time-dependent problem (with variables being the radius, energy, polar angle, and two angles that characterize the neutrino momentum direction) to only four dimensions and reduces the complexity of the moment equations significantly (see Appendix B in Buras et al. 2006a) at the expense of neutrino shear and non-radial flux of the neutrinos, which are disregarded in such an approach. However, the moment equations still contain the terms that account for the advection of trapped neutrinos with the stellar fluid motion in the lateral direction. Moreover, the lateral component of the neutrino pressure gradient is included in the hydrodynamics equations.

Comparison of our approximative treatment of general relativity with fully relativistic simulations revealed excellent agreement in spherical symmetry and still good agreement in two dimensions when the rotation did not become too extreme (see Marek et al. 2006, Liebendörfer et al. 2005).

A state-of-the-art treatment of the interactions of neutrinos (ν) and antineutrinos ($\bar{\nu}$) of all flavors (Buras et al 2006a, Marek et al. 2005) is applied in our simulations, including all relevant β -processes, thermal processes, and the scattering off electrons, positrons, nucleons, and nuclei. In neutral-current and charged-current neutrino-nucleon reactions the effects of nucleon recoil and thermal motions as well as nucleon correlations in the dense medium are taken into account (see Buras et al. 2006a, and references therein). Neutrino-nucleon scattering just like neutrino-electron scattering is therefore a channel for energy exchange between neutrinos and the stellar medium and fosters neutrino thermalization, thus leading to a noticeable reduction of the mean energy and a spectral pinching of radiated neutrinos, in particular of muon and tau flavor (Keil, Raffelt, & Janka 2003). Electron captures on heavy nuclei are described by making use of the improved data of Langanke et al. (2003), who constructed a table for the capture rates of a large ensemble of nuclei in nuclear statistical equilibrium. Also interactions of neutrinos of different flavors, scatterings as well as neutrino-antineutrino pair conversion (Buras et al. 2003b) are included in our treatment.

We employ two different nuclear equations of state (EoSs) in our simulations. On the one hand, we use a soft version of the compressible liquid drop EoS of Lattimer & Swesty (1991; see also Lattimer et al. 1985; “LS-EoS”) with an incompressibility modulus of bulk nuclear matter of 180 MeV and a symmetry energy parameter of 29.3 MeV. On the other hand we perform simulations with the considerably stiffer EoS of Hillebrandt & Wolff (1985, see also Hillebrandt et al. 1984; “HW-

EoS”), which is based on a Hartree-Fock calculation, assuming a Skyrme force for the nucleon-nucleon interaction with parameters given by Köhler (1975). Its incompressibility has a value of 263 MeV and the symmetry energy was chosen to be 32.9 MeV. Details of the calculation can be found in Hillebrandt et al. (1984) and Hillebrandt & Wolff (1985). Both EoSs yield different maximum masses of stable, nonrotating neutron stars. In case of the LS-EoS the maximum gravitational mass is $1.84 M_{\odot}$, whereas it is $2.21 M_{\odot}$ for the HW-EoS, which are both compatible with measured neutron star masses (Lattimer & Prakash 2007). Both EoSs also lead to a significantly different evolution of the radius of the nascent neutron star as a function time (see Fig. 7 in Janka et al. 2007). While the LS-EoS produces rather compact neutron stars with a radius of $R_{\text{ns}} = 11.9$ km for a cold star with $1.4 M_{\odot}$ and $R_{\text{ns}} = 10.0$ km for a cold star near the maximum mass, the corresponding radii are 13.94 km and 13.5 km, respectively, for the HW-EoS (cf. Marek 2007).

We apply the nuclear EoS (either LS or HW) only above a transition density ρ_{EoS} . In the low-density regime, $\rho < \rho_{\text{EoS}}$, the EoS includes the ideal gas contributions of electrons and positrons (of arbitrary degrees of relativity and degeneracy), photons, and a mixture of non-relativistic classical Boltzmann gases of neutrons, protons, α particles, and 14 kinds of heavy nuclei. Coulomb lattice corrections of the pressure, energy density, entropy, and adiabatic index are taken into account. Above a temperature of $T_{\text{NSE}} = 0.5$ MeV the nuclear constituents are assumed to obey nuclear statistical equilibrium (NSE), whereas below this temperature only nuclear burning of silicon and oxygen (and similarly neon and magnesium), and carbon (implemented according to the “flashing” treatment by Rampp & Janka 2002, Appendix B.2) can change the composition. The value of ρ_{EoS} is chosen such that a smooth transition of pressure, internal energy density, and chemical potentials as functions of density is guaranteed. During the collapse phase ρ_{EoS} is set to $6 \times 10^7 \text{ g cm}^{-3}$ in case of the LS-EoS and $1.5 \times 10^9 \text{ g cm}^{-3}$ for the HW-EoS, while after core bounce, when α particles can reach a significant mass fraction and an error in the LS-EoS (Fryer, private communication) is potentially relevant (see, however, Buras et al. 2006a), we use $\rho_{\text{EoS}} = 10^{11} \text{ g cm}^{-3}$.

2.2. Investigated models

Except for a simulation with an $11.2 M_{\odot}$ progenitor from Woosley et al. (2002), for which we show results from a continuation of the model run published by Buras et al. (2006b), all core-collapse and supernova calculations in this work are based on the $15 M_{\odot}$ progenitor s15s7b2 from Woosley & Weaver (1995) and are listed in Table 1. Details of the $11.2 M_{\odot}$ model and a comparison of 1D and 2D results can be found in the Buras et al. (2006b) paper. Two of the $15 M_{\odot}$ calculations are conducted in spherical symmetry, one with the LS-EoS (indicated by “LS-1D” in the model name) and another one with the HW-EoS (labeled by “HW-1D”). These are compared with four 2D (axially symmetric) simulations, two of which (M15LS-2D and M15HW-2D) are computed without rotation, using the EoSs also employed in the 1D models. In the other two simulations (i.e., our reference long-time run, M15LS-rot, and Model M15LS-rot9) we

impose rotation on the progenitor core with initially a constant angular frequency of 0.5 rad s^{-1} (corresponding to a rotation period of about 12 s) inside the Fe core and an $r^{-3/2}$ decline outside (see Fig. 1 in Müller et al. 2004 and Sect. 3.4 in Buras et al. 2006b). This rotation rate is roughly a factor ten faster than current predictions for pre-collapse stellar cores by Heger et al. (2005), but too slow for the free energy reservoir in the secularly evolving proto-neutron star to be sufficient to power magneto-hydrodynamic explosions (see Burrows et al. 2007a and Thompson et al. 2005).

In all of our nonrotating models we have implemented for the monopole of the gravitational potential the effective relativistic potential according to Case A of Marek et al. (2006), which in that paper was identified to yield the best results in comparison to spherically symmetric, fully relativistic simulations. For models with core rotation, however, the best choice of the effective gravitational potential is less obvious. While for slow rotation Case A still produces the most satisfactory results, this monopole term is not able to account for the relativistic gravity of rotationally deformed cores. In such a situation, Marek et al. (2006) found Case R to be the better representation, because, e.g., it leads to central densities closer to those of the relativistic calculation. Several 100 ms after core bounce even our slowly rotating pre-collapse model develops a sizable oblate deformation of the nascent neutron star. Since late-time effects are the main interest of our present investigations, we therefore decided to employ the effective relativistic TOV potential of Case R of Marek et al. (2006) in our reference long-time 2D simulation (Model M15LS-rot) and to compare this model with another simulation that includes rotation and uses Case A for the monopole term of the gravitational potential (Model M15LS-rot9).

Our models are computed with 400–1000 non-equidistant radial zones, which are chosen such that the resolution $\Delta r/r$ is typically better than three percent in the interior of the neutron star and between less than one percent and 1.5 percent around the neutrinospheres and outside of the neutron star. During the simulations the number of radial grid zones N_r is increased (Table 1 gives N_r at the beginning and at the end of the different runs) and the region of higher resolution is moved to smaller radii in order to follow the contraction of the neutron star and to ensure good resolution at the neutron star surface where the density gradient steepens with time. We make sure that at least 20 radial zones are used per density decade, corresponding to at most 12% density variation between neighboring zones. The representation of hydrostatic equilibrium as well as the accurate computation of the neutrino transport in the decoupling layer require at least this numerical resolution; in case of the transport the luminosity variation from zone to zone is a limiting factor. Convergence tests for our code showed that insufficient radial resolution in particular in this region may not only lead to bloated surface layers of the neutron star and to an overestimation of the neutrino luminosities, but as a consequence also to artificial explosions even of spherically symmetric models. In order to make sure that our exploding 2D simulation, Model M15LS-rot, is well resolved, we recomputed a significant part of the crucial evolution phase of this model with about

half the radial zone width in the neutron star surface layer. This high-resolution run, Model M15LS-rot-hr, is not listed in Table 1, but some of the plots will also show results from this calculation for comparison.

Our 2D simulations are performed with 128 or 192 equidistant lateral zones from pole to pole of the spherical coordinate grid (Table 1). Comparing results for both resolutions we found excellent quantitative agreement of the neutron star and neutrino properties (which implies that the lateral resolution is sufficient for describing neutron star convection) and very good qualitative agreement of the shock evolution (because of the chaotic character of hydrodynamic instabilities in the hot-bubble region, a detailed quantitative agreement cannot be expected). At the grid center, however, a small region (1.7 km in radius or six radial zones) is computed in spherical symmetry to avoid the most severe limitation of the hydrodynamics timestep due to the Courant-Friedrich-Lewy condition.

In the transport module of our code we usually employ 17 geometrically distributed energy bins for neutrinos between 0 and 380 MeV. One of our models, M15LS-rot9, is computed only with nine energy bins, which leads to a reduced steepness of the high-energy tail of the neutrino spectrum roughly three orders of magnitude and more below the spectral peak. Spherically symmetric test calculations, however, show that this lower accuracy of the neutrino transport has hardly any influence on the hydrodynamic evolution of the supernova core and also causes only small differences (of order 10%) in the luminosities and mean energies of the radiated neutrinos. Using nine instead of 17 energy bins reduces the CPU time requirements of a simulation by nearly a factor of seven.

The 2D runs without rotation are started at core bounce after mapping the corresponding 1D models to the 2D grid and imposing random zone-to-zone variations of the radial velocity component (or density) with an amplitude of one percent. The rotating models are computed in 2D from the onset of the collapse with random perturbations and the initial rotation law imposed on the spherically symmetric progenitor star (for details, see Buras et al. 2006b).

Running 2D models with a sophisticated energy-dependent treatment of the neutrino transport for many hundred milliseconds after bounce poses a considerable numerical challenge, because the rapid variations of the accretion flow in the presence of violent hydrodynamic instabilities in the postshock region do not allow the (implicit) neutrino transport timestep to become larger than about 2×10^{-6} s and therefore about 500,000 timesteps and 3×10^{18} floating point operations were needed for our most advanced 2D model MS15LS-rot, which was evolved to more than 600 ms after bounce. For this reason, CPU-time limitations did not permit us to follow all of our 2D models to such very late post-bounce times. Although the set of calculations of Table 1 is not finished in this sense (and currently we have no way to do that in an acceptable time frame), it nevertheless allows for some interesting conclusions concerning the possibility of getting neutrino-driven explosions late after bounce and the dependence of this result on the properties and the neutrino emission of the forming neutron star.

3. RESULTS

In this section we discuss our simulations, starting with the 1D results for reference, then continuing with the exploding long-time 2D simulation, and finally turning to the other 2D models, which allow us by comparisons to better understand the factors that are decisive for the explosion in the successful run.

3.1. Spherically symmetric $15 M_{\odot}$ simulations

In Fig. 1 the results of our two 1D simulations are shown in overview. The collapse of the stellar core until bounce is somewhat faster with the softer (i.e. here: its adiabatic index in the subnuclear regime is lower) LS-EoS, and the maximum density reached at bounce is $3.6 \times 10^{14} \text{ g cm}^{-3}$ compared to $3.0 \times 10^{14} \text{ g cm}^{-3}$ in case of the HW-EoS. The central density is measured at a distance of 1.65 km (i.e., in the sixth radial grid zone) where numerical fluctuations caused by the inner grid boundary are absent). During the post-bounce evolution the higher stiffness of the nuclear phase in the HW-EoS leads to a considerably lower central density and a clearly less rapid contraction of the nascent neutron star, visible from the larger radius of the electron neutrinosphere in the right upper panel of Fig. 1. Since the postshock layer is nearly in hydrostatic equilibrium during the quasi-stationary accretion phase of the stalled shock, the shock position R_s is a sensitive function of the neutron star radius, R_{ns} , roughly as

$$R_s \propto \left(\frac{R_{\text{ns}}^4 T_{\text{ns}}^4}{|\dot{M}| M_{\text{ns}}^{1/2}} \right)^{2/3}, \quad (1)$$

which follows from Eqs. (39), (56), and (63) of Janka (1991). Here M_{ns} is the neutron star mass, T_{ns} the temperature at the neutrinosphere, and \dot{M} (< 0) the rate of mass accretion by the shock. In case of the HW-EoS, the stagnation radius of the shock is therefore significantly larger during the phase of shock retraction ($t \gtrsim 80$ – 100 ms after bounce).

In contrast, the luminosities L_{ν} and mean energies ($\langle \epsilon_{\nu} \rangle$) of the neutrinos radiated during shock accretion are appreciably higher in case of the LS-EoS, because the larger neutrinospheric temperature of the more compact neutron star overcompensates for the smaller radius (roughly, the ν_e emission behaves like blackbody radiation and thus $L_{\nu} \propto R_{\text{ns}}^2 T_{\text{ns}}^4$ and $\langle \epsilon_{\nu} \rangle \propto T_{\text{ns}}$). Interestingly, the prompt ν_e burst during shock breakout reveals the opposite dependence on the nuclear EoS: it is more luminous in case of the HW-EoS because of a stronger deleptonization in a wider spatial region, which is facilitated by a less steep increase of the optical depth in the deleptonization region and thus an easier escape of the electron neutrinos.

We also point out that in the simulations with both EoSs the average energy of the radiated $\bar{\nu}_e$ gets very close to that of the emitted muon and tau neutrinos or becomes even slightly higher after about 200 ms of post-bounce accretion (Fig. 1, bottom right). This effect is visible in the mean spectral energies, which are defined as ratio of the energy density to the number density of neutrinos, $\langle \epsilon_{\nu} \rangle = \int_0^{\infty} \epsilon \, d\epsilon \, J_{\nu}(\epsilon) / \int_0^{\infty} d\epsilon \, \epsilon^{-1} J_{\nu}(\epsilon)$, with $J_{\nu}(\epsilon)$ being the zeroth energy moment of the specific inten-

sity³. In contrast, the rms energies of the energy spectrum, $\langle \epsilon_\nu \rangle_{\text{rms}} \equiv [\int_0^\infty d\epsilon \epsilon^2 J_\nu(\epsilon) / \int_0^\infty d\epsilon J_\nu(\epsilon)]^{1/2}$, still follow the standard order sequence, $\langle \epsilon_{\nu_e} \rangle_{\text{rms}} < \langle \epsilon_{\bar{\nu}_e} \rangle_{\text{rms}} < \langle \epsilon_{\nu_x} \rangle_{\text{rms}}$, although the difference between the last two is considerably smaller than in older simulations, in which the transport treatment of heavy-lepton neutrinos ν_x did not take into account the energy exchange through neutrino-nucleon scatterings and the production of $\nu_x \bar{\nu}_x$ pairs by nucleon-nucleon bremsstrahlung and by the annihilation of $\nu_e \bar{\nu}_e$ pairs (for more details, see Buras et al. 2003b, Raffelt 2001, Keil et al. 2003). We will come back to a closer discussion of these interesting spectral properties in Sect. 3.6.

3.2. Two-dimensional $15 M_\odot$ model with explosion

In contrast to the spherically symmetric simulations, the two-dimensional Model M15LS-rot turns out to approach an explosive runaway situation after more than 500 ms of post-bounce accretion (Figs. 2 and 3). Some snapshots of the entropy distribution in the central region (with radii between ~ 400 km and ~ 800 km) for characteristic stages of the evolution are displayed in Fig. 4.

3.2.1. Post-bounce evolution

The results of a 90-degree equivalent of Model M15LS-rot (computed with a pole-to-equator wedge of the spherical coordinate grid and with reflecting conditions at both boundaries) until 300 ms after bounce were described by Buras et al. (2006b), see Sect. 3.4 there. Postshock convection is triggered by the small-scale perturbations that evolve from a 1% random initial (pre-collapse) seed during infall. The convective activity exhibits the most rapid growth in high angular modes and visible inhomogeneities begin to show up at 50–60 ms after bounce. In the 180-degree calculation discussed here, the first large-scale differences between both hemispheres appear at about 100 ms and only shortly later (at ~ 120 ms, see also the top left snapshot in Fig. 4) low-amplitude bipolar shock oscillations set in, manifesting the development of a global, low-mode asymmetry. This can be seen in the top panel of Fig. 5, where large amplitudes of the dipolar ($l = 1$) and quadrupolar ($l = 2$) terms of a spherical harmonics decomposition of the shock radius as a function of the polar angle θ occur at $t \gtrsim 100$ ms post bounce. The plot suggests that the dipole mode gains strength slightly faster and reaches large amplitudes some ten milliseconds earlier than the quadrupole mode.

The appearance of strong low-mode, quasi-periodic shock deformation is associated with sloshing motions of the whole accretion layer between shock and neutron star. The process is very similar to the phenomenon identified as SASI in the idealized accretion setup studied by Blondin et al. (2003) and seen also in more sophisticated post-bounce accretion simulations by Scheck et al. (2008). In those calculations convective activity was initially absent and set in only later, and therefore the oscillatory growth of the SASI in the linear regime could

be clearly identified. In contrast, in the model discussed here, sufficiently strong neutrino heating and sufficiently large seed perturbations cause convective activity in the gain layer to develop readily on a short timescale after bounce. The early presence of convection masks the characteristic growth behavior of the SASI. We suspect that the acoustic waves and vorticity created by convection even accelerate the evolution of the SASI and the conditions for a linear description never exactly apply.

The growth of the SASI modes in the linear regime was analysed in detail by Blondin & Mezzacappa (2006). Their 2D axisymmetric hydrodynamic simulations with a simplified representation of the conditions in supernova cores revealed that the $l = 1$ mode is always unstable, grows faster than the $l = 2$ mode, and is the only mode that makes the transition to the nonlinear stage. Our simulations disagree with their results concerning the faster initial growth of the quadrupole mode (see the evolution during the first ~ 50 ms after bounce in the upper and middle panels of Fig. 5), which however was also seen in some model runs performed by Scheck et al. (2008). In the highly nonlinear phase we observe that the dipole and quadrupole modes are present with similar strengths. During episodes in which the $l = 2$ component dominates the low-mode power (e.g. at $t \sim 150, 290, 380, 480$ ms, see middle panel of Fig. 5), the spectrum is indeed enhanced at frequencies well above 100 Hz (Fig. 5, lower panel), consistent with the expectation that the $l = 2$ mode should be distinguished from the $l = 1$ mode by a higher frequency (Blondin & Mezzacappa 2006, Fig. 4). However, we cannot exclude that some of the activity we find associated with quadrupolar deformations is not a true $l = 2$ but a “ghost” $l = 1$ mode with the frequency of the latter, because the $l = 2$ spectra show a very broad distribution with significant power also below 100 Hz. Perturbations associated with prompt postshock convection in the first tens of milliseconds after bounce (see Marek et al. 2008) and violent neutrino-driven convection at $t \gtrsim 80$ ms, which are present in all of our simulations — different from the idealized accretion models considered by Blondin and Mezzacappa 2006, where the setup was chosen to be convectively stable —, but possibly also numerical errors must be expected to give rise to the excitation of $l = 2$ motions and thus might prevent the presence of a purer and more clearly dominant $l = 1$ mode.

In Fig. 3 the radii of the shock near the north pole and south pole are plotted as functions of time. One can well see the alternating phases of shock expansion in the northern and southern hemispheres. The snapshots in Fig. 4 at 454 ms and 524 ms after bounce capture two such moments in which the shock is inflated in opposite directions. There is an inverse relation between the typical period of these SASI oscillations and the mean shock radius. The period is about 10–12 ms when the shock is near 150 km (around 300–400 ms after bounce) and more like 15–17 ms when the average shock radius reaches 180–200 km (around 500 ms), corresponding to power maxima at typical frequencies between 50 Hz and 100 Hz. Towards the end of the simulation, as the shock expands farther, the oscillation period becomes even longer. This can be seen in the time-dependent frequency spectrum of the low-mode SASI power (obtained from a Fourier analysis of the quantity given in Eq. (2)) in the bottom panel of

³ At sufficiently large radii, where neutrinos in the bulk of the spectrum propagate nearly radially (i.e., the flux factor in the laboratory frame is near unity, which is well fulfilled at the chosen radius of evaluation at 400 km), the local energy and number densities are essentially identical with the energy and number flux densities.

Fig. 5. The power spectrum has a very broad peak in the mentioned frequency interval and decays steeply towards higher frequencies.

The middle panel of Fig. 5 displays the corresponding time evolution of the total power in the $l = 1$ and $l = 2$ modes, computed as the volume integral of the squared dipole and quadrupole amplitudes of the fractional pressure variations between average neutrinosphere radius R_ν and average shock radius R_s (cf. Blondin & Mezzacappa 2006),

$$\text{Power}(l; t) \equiv 2\pi \int_{R_\nu}^{R_s} dr r^2 a_{l,0}^2(r, t), \quad (2)$$

where $a_{l,0}(r, t)$ are the amplitudes of the spherical harmonics expansion of the normalized pressure fluctuations according to

$$\frac{P(r, \theta, t) - \langle P(r, \theta, t) \rangle_\theta}{\langle P(r, \theta, t) \rangle_\theta} = \sum_{l=0}^{\infty} a_{l,0}(r, t) \mathcal{P}_l^0(\cos \theta) \quad (3)$$

with $\mathcal{P}_l^0(\cos \theta)$ being the Legendre polynomials (the index for the azimuthal modes is $m = 0$ because of the axial symmetry of our 2D models). The combined power of the two lowest modes turns out to reflect rather sensitively the dynamical activity in the accretion layer. One should note that during phases of relative quiescence of the dipole mode the quadrupole mode is dominant and vice versa. A high level of activity is reached shortly after convection has become strong and the SASI deformation of the shock has set in ($t \gtrsim 100$ ms after bounce). The following slight reduction of the power is a consequence of the shock retraction between 100 and 150 ms post bounce. When the jump in the entropy, density, and mass accretion rate associated with the composition interface between the Si-layer and the oxygen enriched Si-shell of the progenitor reaches the shock at ~ 170 ms after bounce, transient shock inflation is triggered (cf. Figs. 1, 2, 3, and 6). As a consequence, the SASI power increases again before it decays once more during another period of shock contraction. At $t \gtrsim 400$ ms a phase of basically continuous, slow expansion of the average shock radius begins and the low-mode power grows. After 500 ms until the end of our simulation at ~ 700 ms, the low SASI modes gain another factor of 100 in power (middle panel of Fig. 5), which is accompanied by an accelerating mean shock inflation. Finally, after 550 ms, the expansion of the average shock radius speeds up strongly, and Model M15LS-rot enters a runaway situation that initiates an explosion (Figs. 2, 3, 4, and 6). The shock acceleration is supported by the onset of nucleon recombination to α -particles in the hot-bubble medium or/and by only partial dissociation of α -particles in swept-up matter as the shock reaches radii beyond 200 km and temperatures of less than ~ 1 MeV are present behind the shock (cf. the light-grey region behind the shock in Fig. 2). A nuclear binding energy of about 7 MeV per nucleon is either released by the formation of α -particles or saved when helium is not dissociated. This increases the thermal energy of the stellar gas and thus adds to the energy deposited by neutrino heating in bringing the gas in the gain layer to a gravitationally unbound state (for a further discussion of this point, see Sect. 3.4).

During the outward acceleration of the average shock radius at $t \gtrsim 550$ ms, the two-dimensional shock contour in the axisymmetric Model M15LS-rot develops a

pronounced butterfly-like shape (middle right and bottom panels of Fig. 4) with alternately stronger expansion in either the northern or the southern hemisphere (Fig. 3) and a significantly more inflated southern lobe at the end of the simulated evolution. The nearly unipolar onset of the explosion indicates the dominance of the $l = 1$ SASI mode, consistent with the fact that the amplitude of the $l = 1$ component is clearly dominant in the upper and middle panels of Fig. 5 at $t \gtrsim 600$ ms. The swelling high-entropy plumes of neutrino-heated gas in both hemispheres push the shock outward and create a kink in the shock surface near the equator. The kink feature causes accreted gas to hit the shock at an oblique angle and therefore to be deflected at passing the shock. The deflected gas streams from the northern and southern hemispheres collide and form a long-lived and waving equatorial downdraft. This accretion funnel collects the major fraction of the equatorially infalling gas and channels it towards the neutron star with supersonic velocities. The existence and stability of this feature has important consequences for the long-lasting energy input by neutrino heating into the developing explosion (see Sect. 3.4). Gas with low angular momentum, however, collapses closer to the rotation axis and creates very stable polar downdrafts in both hemispheres. These polar downdrafts are a common feature of all 2D simulations with rotation and their durability and universality can be understood by the Solberg condition, which says that a situation in which the specific angular momentum increases with distance from the rotation axis is stable (see the results and discussion in Scheck et al. 2006).

Rotation, although “modest” in the sense discussed in Sect. 2.2, has an important influence in Model M15LS-rot, but it is not crucial for the evolution after bounce and the final outcome obtained in this simulation. This will be further discussed in Sect. 3.5 by comparing the different models of our set of runs. Until the end of the computation (at ~ 615 ms), the neutron star in Model M15LS-rot has contracted to an average radius of 26 km (compared to 21 km for the 1D Model M15LS-1D) with a pole-to-equator radius ratio of 0.65 (eccentricity of 0.76). It rotates strongly differentially with an average period of 3 ms. In the gain layer the rotation period is typically longer than 10 ms.

3.2.2. Runaway conditions and explosion criteria

At $t \gtrsim 350$ ms Model M15LS-rot evolves gradually and steadily towards a situation that is more and more favorable for an explosion. This is clearly visible in a number of quantities. Not only the continuous expansion of the shock front (Figs. 2, 3, and 6) but also the mass, energy, and neutrino heating in the gain layer reveal the trend that the explosion conditions become better at later times.

Two timescales are crucial for the behavior of the gain layer: the timescale of accreted matter to be advected from the shock to the gain radius,

$$\tau_{\text{adv}} \equiv \frac{R_s - R_g}{|\langle v_r \rangle|}, \quad (4)$$

and the neutrino heating timescale of the gas in this region,

$$\tau_{\text{heat}} \equiv \frac{|E_{\text{bind}}|[R_g, R_s]}{Q_{\text{heat}}} \quad (5)$$

Here R_g denotes the average gain radius, $\langle v_r \rangle$ is the average postshock velocity, E_{bind} the total energy of the matter in the gain layer as sum of internal, kinetic, and gravitational energies, and Q_{heat} is the integrated net heating rate by neutrinos. Therefore τ_{heat} measures the time it takes neutrinos to deposit an energy equal to the binding energy $E_{\text{bind}}[R_{\text{gain}}, R_{\text{shock}}]$ of the matter in the gain layer, whereas τ_{adv} can be considered as a measure of the duration the gas is exposed to neutrino energy deposition. In multi-dimensional simulations when non-radial hydrodynamic instabilities play an important role, Eq. (4) for evaluating the advection timescale should be replaced by Eq. (8) of Buras et al. (2006b). A ratio of $\tau_{\text{adv}}/\tau_{\text{heat}} > 1$ can be considered as indicative of favorable conditions for an explosion (Janka et al. 2001, Thompson et al. 2005, Buras et al. 2006b). Of course, the definitions of both timescales contain a variety of ambiguities and uncertainties, e.g. whether the total energy or just the internal energy is the more suitable energy scale in the nominator of Eq. (5) or where and how exactly the mean advection velocity in the denominator of Eq. (4) should be measured. Therefore the timescale ratio is only a rough diagnostic number that can be indicative of the presence or absence of a generally favorable trend, but certainly $\tau_{\text{adv}}/\tau_{\text{heat}} > 1$ cannot be taken as a rigorous quantitative criterion for the onset of the successful blast. Murphy & Burrows (2008) also stress this fact and instead recommend to monitor the residence time distribution function of tracer particles, which is better able to capture the complex flow dynamics in multi-dimensional simulations. While this is unquestionably correct, the numerical effort of tracking tracer particle paths is considerably bigger than performing an analysis of the simulations on the basis of Eqs. (4) (or its multi-dimensional analog as given by Eq. (8) of Buras et al. 2006b) and Eq. (5).

Figure 7 shows that along with the growing strength of the low SASI modes (cf. Fig. 5) the advection timescale in Model M15LS-rot rises continuously after 350 ms post bounce, leading to a steady growth of the timescale ratio $\tau_{\text{adv}}/\tau_{\text{heat}}$ from about 0.6 to values larger than unity. The critical value of unity is exceeded at ~ 530 ms after bounce and the ratio remains larger than unity until the end of the simulation, i.e. for a period of time much longer than the heating timescale $\tau_{\text{heat}} \approx 20$ ms. This is a necessary condition for an explosion (see Buras et al. 2006b). Note that even after the shock starts a rapid acceleration at 550 ms, τ_{adv} can be evaluated because there is net accretion still going on. At the end of our simulation for Model M15LS-rot, about 50% of the matter swept up by the shock is still accreted onto the neutron star (the fraction is larger at earlier times), while the rest stays in the gain layer and causes a growth of the mass there at a rate of more than $0.1 M_{\odot} \text{ s}^{-1}$ (see the top panel in Fig. 8). The dominance of mass inflow towards the neutron star compared to mass outflow through the gain radius until $t \gtrsim 650$ ms after bounce cannot only be concluded from the fact that the advection timescale is still defined at such a late time. It is also suggested by the mass shell trajectories in Fig. 2 at this time, which indicate that a significant fraction of the matter in the gain layer is still crossing the gain radius with negative velocities.

The neutrino-heating timescale of the gain layer in

Model M15LS-rot levels off near 20 ms after $t \sim 350$ ms (Fig. 7, middle panel). This corresponds to a net rate of neutrino energy deposition (the “net rate” is defined as the rate of energy input by neutrinos minus the rate of energy loss by neutrino reemission) of about $4 \times 10^{51} \text{ erg s}^{-1}$ (Fig. 8, middle panel) with a mild increase with time. This increase is a consequence of the slowly growing mass and optical depth of the gain layer and of the higher mean energies of the neutrinos radiated at later times (see Fig. 1 and 14). The corresponding neutrino heating efficiency, defined as ratio of the total net energy deposition to the sum of the radiated ν_e and $\bar{\nu}_e$ luminosities, rises from about 6% at 350 ms to peak values of more than 8% at times later than 500 ms after bounce.

With the accumulation of mass in the gain layer, also the internal energy in this region grows (Fig. 9, upper right panel). The same is true for the rotation energy of the accreted matter, which rises because the gas that is accreted at later times comes from larger distances and has a higher specific angular momentum. The increase of both energies, however, is rather moderate (some 10%) compared to the growth of the kinetic energy of fluid motions in the gain layer in non-azimuthal directions. Both the energy associated with gas flows in latitudinal direction and with gas motions in radial plus lateral directions gain a factor of roughly four between 350 ms and 600 ms (Fig. 9, upper left plot). This, of course, reflects the increasingly more violent SASI and convective activity in the shocked flow. These energies are around 10^{49} erg, corresponding to ~ 0.7 MeV per nucleon, a value that is dwarfed by the neutrino heating rate (300 MeV s^{-1} per nucleon), applied for a typical timescale τ_{adv} , and by the recombination energy of nucleons to α -particles. Accordingly, the total energy per nucleon in the gain layer changes much more strongly from a mean value of about -7 MeV at 350 ms to -3.5 MeV around 600 ms and to only -2 MeV at 700 ms.

Towards the end of the computed evolution of Model M15LS-rot a sizable and steeply rising fraction of the mass in the gain layer has obtained a specific energy that is either positive or only marginally negative (Fig. 9, lower two panels). The energy of all mass in the gain layer with positive total (internal plus kinetic plus gravitational) specific energy and positive radial velocity at that time is roughly 2.5×10^{49} erg and also steeply increasing (Fig. 9), correlated with a very steep rise of the kinetic energies near the termination point of the simulation.

A variety of energy parameters therefore signals that an explosion begins to develop in Model M15LS-rot. This can also be concluded from the behavior of the advection timescale and the timescale ratio at the end of our simulation. Both show a steep increase because more and more matter in the gain region attains positive velocities and starts expanding (Fig. 7). Since a growing fraction of the matter that is accreted by the shock stays in the gain layer, the mass in this layer grows and the gas infall rate onto the neutron star is reduced. Correspondingly, less neutrinos are radiated from the accretion layer near the neutron star surface. This leads to a visible reduction of the luminosities of ν_e and $\bar{\nu}_e$ and of the mean energies of all kinds of neutrinos (Fig. 14).

3.2.3. Role of the SASI

In the last section we argued that the combination of shock expansion, critical timescale ratio, and growing mass and energy in the gain layer indicates that Model M15LS-rot approaches a runaway situation. The described behavior of these quantities is very similar to the findings of Scheck et al. (2008) for their exploding model W00F (cf. Figs. 19 and 20 in their paper). In the latter model the growth of buoyancy instabilities was initially damped due to the choice of small seed perturbations and a low neutrino-heating rate in the gain layer. In contrast, the larger perturbations that have developed in the stellar core of Model M15LS-rot during the collapse allow convection to begin in this simulation as soon as neutrino heating achieves to create a convectively unstable situation in the gain layer. Therefore the growth of the SASI and of convection cannot be studied separately in the present simulation.

Nevertheless, the large-amplitude low-mode shock oscillations seen in Model M15LS-rot only ~ 100 ms after bounce (see Figs. 3 and 5) clearly indicate the presence of the SASI, whose growth appears to be accelerated by the sonic and vorticity perturbations associated with the convective activity in the postshock region. Systematic studies by Scheck et al. (2008) showed that the SASI can play an important supportive role for neutrino-driven explosions. Scheck et al. (2008) demonstrated that SASI shock oscillations can develop even in conditions which per se are unfavorable for the growth of convection. Thus the SASI can assist the delayed revival of the stalled shock in at least two ways: (i) Large-amplitude expansion and contraction phases of the shock lead to supersonic lateral velocities in the postshock flow and the formation of sheets with very steep unstable entropy gradients. This fosters the development of secondary convection or strengthens the ongoing convective activity. (ii) SASI sloshing motions as well as strong postshock convection do not only produce large non-radial velocity components in the postshock flow but also push the accretion shock to larger radii. This again reduces the average infall velocity in the postshock layer, because the velocity in the free-fall region ahead of the shock drops like $R_s^{-1/2}$. A larger shock radius thus leads to a significantly longer advection timescale, roughly $\tau_{\text{adv}} \propto R_s^{3/2}$.

These effects help to keep accreted matter in the gain layer for a longer period of time (a consequence of which is the increasing mass in this layer). This supports the energy deposition by neutrinos and thus facilitates the explosion. So, although the kinetic energy associated with the SASI remains negligible for the explosion energetics, once the SASI and convection have pushed the shock sufficiently far out, prolonged neutrino heating and ultimately also the additional energy release by nucleon recombination (or, similarly, energy savings by only partial dissociation of nuclei in the shock-accreted gas) set up the conditions for runaway.

The contributing effects in the postshock accretion flow, the SASI, convection, and neutrino heating, however, are strongly linked and interdependent in a complex way. In such a highly nonlinear situation it is therefore extremely difficult to exactly determine the influence of each aspect individually. It is, for example, unclear which conditions are primarily responsible for the growth of the SASI power at late post-bounce times ($t \gtrsim 300$ ms), and

which role neutrino heating may play in this context. By comparing in Sect. 3.5 Model M15LS-rot with the other simulations of our sample — although it was not yet possible to carry these other runs to equally late times as our reference model — we will strive for a better understanding of the influence of at least some potentially important aspects like rotation and the contraction and growing compactness of the forming neutron star.

3.3. Two-dimensional $11.2 M_\odot$ model with explosion

As discussed in the previous sections, the strong amplification of the SASI and convective activity lead to runaway conditions and the initiation of an explosion in Model M15LS-rot for a $15 M_\odot$ star. Buras et al. (2006b) observed a similar situation in their 180-degree simulation of the collapse and post-bounce evolution of a (non-rotating) $11.2 M_\odot$ progenitor from Woosley et al. (2002). Different from our successful $15 M_\odot$ run, the neutrino-powered explosion was found to set in much earlier, namely already at about 200 ms after bounce.

The importance of the presence of low-mode SASI oscillations for the development of the blast in this case was concluded from the comparison with a simulation that was computed with the same input physics but with the lateral grid constrained to a 90-degree wedge around the equatorial plane of the polar coordinate system and periodic boundary conditions. This simulation did not show an explosion until the same post-bounce time⁴. In the latter setup the choice of the grid did not allow for the occurrence of $l = 1$ and $l = 2$ SASI modes. Interestingly, Marek (2007) obtained an explosion for the $11.2 M_\odot$ progenitor when he reran the model with a 90-degree grid extending from the pole to the equator with reflecting boundaries, thus assuming equatorial symmetry and excluding the $l = 1$ mode but giving room for the mirror symmetric $l = 2$ mode. This result was recently confirmed by Murphy & Burrows (2008) and shows that obviously the support of strong quadrupolar SASI motions makes already a significant difference compared to a case where both lowest-order spherical harmonics are suppressed.

Here we present some results for a continuation of the $11.2 M_\odot$ explosion simulation of Buras et al. (2006b). Due to the larger timesteps that were possible in this case, we could evolve the model further into the explosion. The results are therefore of interest in the present context because they provide insight into the way the explosion strengthens at evolution stages that we were unable to reach in the $15 M_\odot$ run.

Figure 10 displays the mass-shell evolution as deduced from the (mass-weighted) angle-averaged 2D data of the simulation. Grey or yellow shading of different regions gives rough information about the nuclear composition in the corresponding layers. One can see that the onset of the shock expansion coincides with only partial dissociation of helium nuclei to free nucleons in the postshock region. Whether this is causal for the shock expansion or just a consequence of it, is not finally clear. In any case,

⁴ Of course, this does not permit the conclusion that an explosion could not occur later. Such a possibility, however, seems disfavored because the sensible parameters for a runaway situation (advection timescale, neutrino heating rate, mass in the gain layer, etc.) exhibit a much more pessimistic trend than in the successful $11.2 M_\odot$ run with the 180-degree grid.

the larger abundance of α -particles reduces the consumption of thermal energy for breaking up strongly bound nuclei. Figure 10 also shows that the shock reaches the infall layers containing a mass fraction of more than 10% oxygen at $t \approx 270$ ms after bounce only after it has already propagated to more than 700 km.

At that time the shock is already half way through the supersonically collapsing inner shells of the progenitor star and on average rushes outward with a radial velocity of $10,000 \text{ km s}^{-1}$ (Fig. 11, left panel). The shock surface has a highly deformed prolate shape with an $z : x$ -axis ratio of more than 2:1 (Figs. 11 and 12). Large lobes filled with neutrino-heated, high-entropy gas expand into the northern and southern hemispheres and are continuously fed with fresh material that is channelled in a long-lived, very stable equatorial accretion funnel from behind the shock to the close vicinity of the gain radius to absorb energy there from neutrinos. The situation is very similar to what we observed in the case of our $15 M_{\odot}$ explosion model (see Sect. 3.2.1). Until the end of the simulated evolution, the outward moving, hot gas in the two big lobes (the northern one being slightly larger) has accumulated a positive total (internal plus kinetic plus gravitational) energy of nearly 2.5×10^{49} erg with a tendency of steep rise (Fig. 11, right panel).

The pronounced asphericity has the consequence that the shock reaches the silicon-oxygen interface near the equatorial plane later than in the polar directions (see the panels for $t = 250$ ms and 275 ms after bounce in Fig. 12). Therefore a wedge-like region around the equator remains for some time, where silicon and sulfur are still present with higher abundances between the shock and the oxygen layer, while the matter swept up by the shock consists mostly of iron-group nuclei and α -particles. The mass-shell plot of Fig. 10, which is constructed from the laterally averaged 2D data at each radius, is misleading by the fact that this preshock material appears to be located behind the angle-averaged shock radius (at post-bounce times $270 \text{ ms} \lesssim t \lesssim 300 \text{ ms}$). We note that the penetration into the oxygen-rich infalling shells, beginning at $t \sim 250$ ms p.b., does not have any obvious supportive or strengthening effect on the outgoing shock.

In Fig. 13 we provide information about the conditions and neutrino-energy deposition in the gain layer of the $11.2 M_{\odot}$ model. As in the $15 M_{\odot}$ case the mass in the gain layer increases when the shock begins its outward expansion. At the same time the infall (advection) timescale of matter between the shock and the gain radius increases, but continues to be well defined. Again, as in the $15 M_{\odot}$ explosion model, this suggests the presence of ongoing accretion of gas through the gain layer to the neutron star (which can also be concluded from the continued contraction of mass shells in this region in Fig. 10). Shortly after the (net) neutrino-heating rate has reached a pronounced peak of about $7.5 \times 10^{51} \text{ erg s}^{-1}$ at $t \approx 70$ ms, it makes a rapid drop to around $3 \times 10^{51} \text{ erg s}^{-1}$. This decline is a consequence of the decay of the neutrino luminosities at the time when the mass infall rate onto the shock and the neutron star decreases. The decrease occurs when the steep negative density gradient (and positive entropy step) near the composition interface between the silicon layer and the oxygen-enriched Si-layer of the progenitor star (near $1.3 M_{\odot}$) arrives at the shock (at $t \approx 100$ ms after bounce).

Nevertheless, the heating timescale shrinks essentially monotonically, which points to an evolution of the matter in the gain layer towards an unbound state, i.e., the absolute value of the total gas energy in the numerator of Eq. (5) goes to zero.

3.4. Explosion energy

In both our $11.2 M_{\odot}$ and $15 M_{\odot}$ explosions, the energy of the matter in the gain layer with positive radial velocities (“explosion energy”) reaches $\sim 2.5 \times 10^{49}$ erg at the end of the computed evolutions and rises with a very steep gradient (Figs. 9 and 11). Therefore reliable estimates of the final explosion energy cannot be given at this time. For that to be possible, the simulations would have to be continued for many hundred milliseconds more (which is numerically a challenging task and currently impossible for us with the sophisticated and computationally expensive neutrino transport and chosen resolution). This is obvious from the neutrino-driven explosion models investigated by Scheck et al. (2008; Figs. 9 and 10 there) and Scheck et al. (2006; Appendix C there) and has several reasons. (1) When rapid shock acceleration sets in, only a smaller fraction of the mass in the gain layer starts to attain positive total specific energy (see Fig. 9 for our $15 M_{\odot}$ explosion model and Fig. 24 in Buras et al. 2006b for the $11.2 M_{\odot}$ simulation), and it takes several ten milliseconds until a major part of the mass between shock and gain radius follows the outward motion of the shock and the explosion energy reaches even only some 10^{49} erg (cf. Fig. 10 in Scheck et al. 2008, Fig. 11 and Fig. 24 in Buras et al. 2006b for the $11.2 M_{\odot}$ explosion, and Fig. 9 for the exploding $15 M_{\odot}$ model). (2) Also then the energy of the explosion grows only gradually and initially roughly linearly with a rate of some 10^{50} erg per 100 ms. During this phase ongoing accretion transports fresh gas towards the gain radius, where a part of the gas absorbs energy from neutrinos and begins to rise again, while the rest of the accreted gas is advected into the cooling layer below the gain radius and is added into the forming neutron star. (3) After some time the downdrafts of accreted matter may be quenched and the inflow of gas towards regions near the gain radius may stop. Nevertheless, more neutrino-heated gas is ejected in the neutrino-driven wind that sheds off matter from the surface layer of the nascent neutron star. During this phase the increase of the explosion energy levels off, but still a significant fraction of the final energy may be added (though with a much lower rate) over timescales of several more seconds. The corresponding wind power is a very sensitive function of the neutrino emission properties (i.e., of the time-dependent luminosities and mean energies of the radiated neutrinos) and of the neutron star mass and radius. Some 10^{50} erg, in optimistic estimates even more than 10^{51} erg, of energy might be pumped into the supernova this way after the onset of the blast (see Burrows & Goshy 1993; Qian & Woosley 1996; Thompson, Burrows, & Meyer 2001). (4) The total energy injected at the explosion center has to be corrected for the negative total energy of the gravitationally bound outer stellar shells, which are going to be swept out in the blast instead of falling back to the neutron star.

Point (2) implies that simultaneous accretion and outflow of neutrino-heated gas as a generically multi-

dimensional phenomenon is an essential feature of the supernova explosion mechanism. The rate at which accreted, cool gas is channelled through the neutrino-heating region, gains energy from neutrinos, and finally rises outward again (the process described in point (2) above) decides about the power that is accumulated in ejected material. Let the corresponding outflow rate of neutrino-heated gas be a fraction ζ of the mass accretion rate \dot{M}_{acc} through the shock, i.e., $\dot{M}_{\text{out}} = \zeta \dot{M}_{\text{acc}}$. The rate at which energy is pumped into the ejecta can then be estimated very roughly as

$$\begin{aligned} \dot{E}_\nu &\sim \zeta \dot{M}_{\text{acc}} \dot{q}_\nu \tau_{\text{adv}} \\ &\sim 2 \times 10^{51} \frac{\text{erg}}{\text{s}} \left(\frac{\zeta}{0.5} \right) \left(\frac{\dot{M}_{\text{acc}}}{0.2 M_\odot/\text{s}} \right) \times \\ &\quad \times \left(\frac{\dot{q}_\nu m_{\text{B}}}{300 \text{ MeV/s}} \right) \left(\frac{\tau_{\text{adv}}}{30 \text{ ms}} \right). \quad (6) \end{aligned}$$

Here m_{B} is the baryon mass and \dot{q}_ν the average net neutrino energy deposition rate per unit of mass in the gain layer, which can be estimated by the ratio of the net neutrino heating rate in the gain layer, $\dot{E}_{\nu, \text{gain}}$ (middle panel of Fig. 8), to the mass M_{gain} in the gain layer (upper panel of Fig. 8):

$$\dot{q}_\nu \approx \frac{\dot{E}_{\nu, \text{gain}}}{M_{\text{gain}}}. \quad (7)$$

The advection timescale τ_{adv} through the gain region in Eq. (6) is a measure of the mean exposure time of the gas to neutrino heating⁵. The numerical values used in Eq. (6) are guided by the conditions at $t \gtrsim 600 \text{ ms}$ in run M15LS-rot (see Figs. 6, 7, 8, and Sect. 3.2.2), for which we therefore estimate $\dot{E}_\nu \sim (1..2) \times 10^{51} \text{ erg s}^{-1}$. In the case of our explosion simulation of the $11.2 M_\odot$ star, Eq. (6) with the numbers taken from the latest evolution stage shown in Fig. 13 yields a neutrino energy input rate to the ejecta of $\dot{E}_\nu \sim (3..6) \times 10^{50} \text{ erg s}^{-1}$, which is consistent with the growth of the positive energy in the gain layer at the end of the model run (compare Fig. 11, right panel). The energy deposition rate according to Eq. (6) is of the order of the net neutrino heating rate of the gain layer, $\dot{E}_{\nu, \text{gain}}$ (see Figs. 8 and 13). In contrast to the latter, however, it accounts for the fact that not all of the matter that absorbs energy from neutrinos in the gain layer will finally be added to the outflow (see also Sect. 3.2.2). We note that the power of the outflow of neutrino-heated matter is seriously underestimated in simulations with Newtonian instead of relativistic gravity, because in the Newtonian case the luminosities and energies radiated during the accretion phase of the less compact and cooler neutron star are considerably lower and \dot{q}_ν is correspondingly smaller.

With \dot{E}_ν from Eq. (6) and the duration τ_{acc} of the accretion phase, the explosion energy, in a crude way, can be written as

$$E_{\text{exp}} \approx \dot{E}_\nu \tau_{\text{acc}} + E_{\text{wind}} + E_{\text{burn}} - E_{\text{bind}}. \quad (8)$$

⁵ The product $\dot{M}_{\text{acc}} \tau_{\text{adv}}$ turns out to be a fairly accurate representation of the mass in the gain layer at all times after bounce. This fact confirms that the advection time according to the definition in Eq. (8) of Buras et al. (2006b), which is used to evaluate τ_{adv} in our models, is reasonable and meaningful.

Here the first term on the rhs side accounts for the total energy that is transferred by neutrinos to the ejecta during the phase of simultaneous accretion and outflow. The second term measures the integrated power of the neutrino-driven wind that starts after accretion has ceased (the phase mentioned in point (3) above). Wind matter in contrast to accreted gas must be lifted all the way out of the deep gravitational potential at the neutron star surface. The third term takes into account additional energy release by nuclear burning in shock-heated matter when the shock wave reaches layers of still unburned nuclear fuel, and the fourth term corrects for the gravitational binding energy of the overlying stellar material (as addressed in point (4) above). For stars around $15\text{--}20 M_\odot$ the last two terms can be estimated to approximately compensate each other (see Janka et al. 2001). In the neutrino-driven wind phase (when accretion of infalling gas onto the neutron star has ended) the gain radius retreats to a location closely outside of the neutrinospheres (this phase is not yet reached in both the $11.2 M_\odot$ and $15 M_\odot$ explosions discussed in this paper, see Figs. 2 and 10).

The release of nuclear recombination energy E_{rec} when free nucleons in the neutrino-driven wind ejecta assemble to α -particles and heavier nuclei, must be included as a positive contribution to the E_{wind} term so that $\dot{E}_{\text{wind}} = \dot{E}_{\nu, \text{gain}} + \dot{E}_{\text{rec}}$ during the wind phase. For matter that is accreted through the shock and gets heated by neutrinos (an effect that is accounted for in the first term on the rhs of Eq. (8)), however, such nucleon recombination does *not* necessarily mean a gain in the energy budget. The gas swept up by the shock and falling inward to the neutron star in downflows is initially composed of nuclei (iron, silicon, or oxygen, depending on the location of the shock, see Fig. 2). Compressional heating within the shock and in the downflows (or ultimately energy deposition by neutrinos) produces such high temperatures that the nuclei get disintegrated, which consumes a fair amount of dissociation energy. This energy can subsequently be recovered in the fraction of the matter that reexpands and gets blown out again. Different from the energy input by neutrinos, the recombination of nucleons, however, yields a net energy gain only when the nucleon recombination leads to a state with higher nuclear binding energy per baryon. This means that the net gain of energy by nuclear processes in the accreted material can at most be equal to the difference in the binding energy of oxygen or silicon (initially present in the accretion flow) compared to iron-group elements (the most strongly bound nuclei), which is much smaller than the complete recombination energy of free nucleons to nuclei.

For both components of the ejecta, however, for the neutrino-driven wind material as well as accreted and reexpanding matter, nuclear processes are unlikely to be the main source of the energy excess (and thus of the explosion energy) that the matter carries outward in the supernova blast. On the one hand, gas residing in the gain layer before the explosion sets in as well as matter ablated from the neutron star surface in the later neutrino-wind phase is initially at rest in the strong gravitational field very close to the neutron star and has a largely negative total energy ($\mathcal{O}(-10 \text{ MeV/nucleon})$ or more). The en-

ergy liberated by the recombination of free nucleons to nuclei in this matter, though large ($\sim 7\text{--}8.8$ MeV per nucleon), can typically only assist the revival of the stalled shock but cannot account for all the energy needed to make this matter gravitationally unbound. Neutrino energy deposition is also needed to overcome the gravitational binding and to produce the positive energy of the ejecta at infinity. On the other hand, gas that is accreted from large distances, channelled through the neutrino-heating region, and then reexpanding outward right away is initially gravitationally only weakly bound (its total specific energy is typically only of the order of $-(1\text{--}2)$ MeV per nucleon). A change of the nuclear composition in this matter by assembling heavier nuclei from lighter ones can release only a relatively small amount of energy (also of the order of $1\text{--}2$ MeV per nucleon) and can bring the gas at most to a gravitationally marginally unbound energy level. So again the ultimate energy excess that drives the supernova explosion has to come from another source. Neutrino energy deposition plays this dominant role in our simulations.

In this context it is crucial to answer the question how long accretion can continue and how long efficient energy input by neutrinos according to Eq. (6) can therefore apply. The time when accretion ends can be deduced in a crude way from the requirement that at this moment the outgoing shock (with velocity v_s and postshock velocity v_2 in the observer frame) must accelerate the postshock matter to escape velocity. The corresponding radius is therefore determined by

$$R_{\text{esc}} \approx \frac{2GM}{v_2^2} \sim 5400 \text{ km } M_{1.5} v_{s,9}^{-2}, \quad (9)$$

where $M_{1.5}$ denotes the enclosed mass normalized to $1.5 M_\odot$, $v_{s,9}$ the shock velocity in 10^9 cm s^{-1} , and the postshock velocity v_2 was determined from the preshock velocity v_1 and the shock velocity v_s by the first shock-jump condition as

$$v_2 = (1 - \beta^{-1})v_s + \beta^{-1}v_1 \approx \frac{6}{7} v_s, \quad (10)$$

with $\beta = \rho_2/\rho_1 \approx 7$ and $v_1 \sim 0$. For the duration of the accretion phase after the onset of outward shock expansion we therefore get:

$$\tau_{\text{acc}} \approx \frac{R_{\text{esc}}}{v_s} \sim 0.5 \text{ s } M_{1.5} v_{s,9}^{-3}. \quad (11)$$

This means that accretion can easily continue for half a second or even longer, if the shock expands slowly in the beginning. This is confirmed by the supernova simulations of Scheck et al. (2006), in some of which accretion was observed to still go on significantly longer than one second after the explosion had started. The explosion energy is therefore not determined by the conditions just at the moment when the outward shock acceleration begins or when the shock is in its early stage of expansion. For this reason it is impossible to conclude from our simulations that the $11.2 M_\odot$ and $15 M_\odot$ explosions will finally be weak or strong. In the multi-dimensional environment of the supernova core with accretion and shock expansion being simultaneously present, it is essential to take into account the long-lasting period of mass downflow to

the nascent neutron star⁶. Even though the neutrino-driven explosion sets in rather late after bounce in our simulation, Eqs. (6) and (11) suggest that the nonspherical nature of the gas flow in the supernova core, due to which the neutrino-heating region around the neutron star is replenished with fresh gas over a long period of time, may well allow the explosion energy $E_{\text{exp}} \sim \dot{E}_\nu \tau_{\text{acc}}$ to reach several 10^{50} erg for the $11.2 M_\odot$ progenitor and even a value around the canonical number of 10^{51} erg in the case of our $15 M_\odot$ explosion model.

3.5. Comparison of $15 M_\odot$ models

Comparing Model M15LS-rot with the other 2D simulations of our sample allows one to gain insight into various aspects that may have important influence on the post-bounce evolution.

3.5.1. High-resolution Model M15LS-rot-hr

Repeating the computation of Model M15LS-rot during the crucial phase of growing SASI power between ~ 420 ms and ~ 670 ms after bounce with finer radial zoning (Model M15LS-rot-hr) does not reveal any significant differences due to the resolution until 550 ms (cf. Figs. 6–9). Only the transient phase of damped SASI activity around 500 ms in our reference run of Model M15LS-rot (see the middle panel of Fig. 5), which leads to a short pause in the expansion of the average shock radius (Fig. 6) and a step-like interruption of the rise of the advection timescale (Fig. 7), is absent in Model M15LS-rot-hr. This suggests that the feature is just a consequence of the chaotic and stochastic behavior of the non-radial hydrodynamic instabilities that stir up the flow between shock front and forming neutron star.

The conditions that can be considered as favorable for an explosion evolve in a promising way also in Model M15LS-rot-hr. The average shock radius and the mass in the gain layer exhibit a monotonic trend of increase (Fig. 6 and top panel of Fig. 8, respectively). The advection timescale shows the same behavior. Because at the same time the neutrino-heating timescale, heating rate, and heating efficiency settle to stable levels (Figs. 7 and 8), the timescale ratio climbs to a value of ~ 1.3 , around which it fluctuates at $t \gtrsim 580$ ms. Nevertheless, after $t \sim 570$ ms the evolution of Model M15LS-rot-hr departs from that of Model M15LS-rot. The latter develops an explosion after $t \sim 570$ ms, whereas the former reveals SASI activity with a growing amplitude but no onset of strong outward shock acceleration until the end of our simulation.

An inspection of the different energies that characterize the energetic conditions in the gain layer reveals that the kinetic energy, in particular the part that is associated with the radial velocity component, begins to deviate between the two models around the time when their evolution starts to diverge (upper left panel of Fig. 9). Also the internal energy of the gain layer begins to grow faster in Model M15LS-rot than in its better resolved counterpart, but the difference appears slightly later (at ~ 590 ms instead of ~ 570 ms) and grows more gradually

⁶ A longer accretion phase of the nascent neutron star after the onset of the supernova explosion is also crucial for setting the explosion energy in case of the acoustic mechanism as discussed by Burrows et al. (2007c).

than for the kinetic energy. Other energies as well as the neutrino-heating rate do not show any peculiar differences. While the divergence of the internal energies is likely to be a consequence of the stronger shock expansion in Model M15LS-rot, which leads to growth of the mass in the gain layer, the difference of the radial kinetic energy could be causal for the discrepant later evolution of both simulations. Unfortunately, because of the complex interdependence of different effects (hydrodynamics, gravity, neutrino physics) we are not able to unambiguously track down the origin of this energy difference and to clarify whether it is really the reason or also just the result of the evolution that separates at about 570 ms.

In any case, however, it shows that in the given situation the later development of Models M15LS-rot and M15LS-rot-hr seems to be extremely sensitive to relatively small effects. An excess of order 10^{49} erg in the kinetic energy of the radial motions (and also – but a factor of ~ 4 lower – in the lateral kinetic energy, see upper left panel of Fig. 9) and a correspondingly stronger SASI and convective activity, which could be caused by chaotic fluctuations, appears to be sufficient to initiate the outward acceleration of the shock and to cause the bifurcation of the subsequent evolution of both models. This by itself is a very interesting result, which, of course, raises questions about the importance of stochastic variations or about the robustness of the explosion found in Model M15LS-rot, for example with respect to differences in the spatial resolution used in the simulations. We repeat and stress here, however, that a variety of diagnostic parameters like the growing shock radius and SASI activity as well as the large value of the ratio of advection to heating timescale, exhibit an overall trend that appears very favorable for an upcoming explosion also in the case of Model M15LS-rot-hr. Unfortunately, without being able to run this model (and any of the other $15 M_{\odot}$ simulations, in particular with high resolution) for a sufficiently long post-bounce time — which is presently prevented by the limited computer resources available to us — we have no convincing support for this reasoning.

3.5.2. Rotating Model M15LS-rot9

Model M15LS-rot9 was computed with a somewhat weaker effective relativistic gravitational potential than our standard Model M15LS-rot (Case A of Marek et al. 2006 instead of Case R; the former yields the more accurate treatment for nonrotating stellar core collapse according to comparisons with fully relativistic simulations). A comparison of these two simulations with the nonrotating Model M15LS-2D, which shares the description of the effective relativistic potential with Model M15LS-rot9 (cf. Table 1), allows us to draw conclusions on the importance of rotation and of the strength of the gravitational potential.

Model M15LS-2D without centrifugal effects but with weaker gravity is astonishingly similar to Model M15LS-rot in many of the evaluated aspects. This is true, e.g., for the neutrino luminosities at $t \gtrsim 200$ ms after bounce (bottom panel in Fig. 14) and for the neutrino-heating rate in the gain layer and the heating efficiency (Fig. 8) as well. But also the average shock radii of both models are fairly similar and therefore the advection timescales do not differ much (Figs. 6, 7). The ratio of the advection

timescale to the heating timescale shows the same trend in both cases, with a slight time lag of Model M15LS-2D (lower panel of Fig. 7). This suggests that rotation does not play an essential role for the evolution of Model M15LS-rot towards runaway. In fact, with respect to the overall long-time behavior, rotation seems to just compensate much of the influence of the stronger gravitational potential used in Model M15LS-rot.

The weaker gravity in Model M15LS-rot9 relative to Model M15LS-rot allows the shock to move farther out by ~ 20 km on average during the first 300 ms after bounce (Fig. 6). Since also the infall velocity in the preshock region is lower due to the reduced gravitational acceleration, the advection timescale is significantly longer in Model M15LS-rot9. At the same time, the accretion luminosities of neutrinos in Model M15LS-rot9, in which the neutron star is less compact and less hot, are significantly smaller (Fig. 14, bottom panel) and therefore the overall postshock heating is weaker (up to roughly a factor of two; Fig. 8) and the heating timescale is considerably longer (typically a factor of two; Fig. 7) than in Model M15LS-rot. For this reason, Model M15LS-rot9 appears to be less favorable for generating a SASI-aided neutrino-driven explosion than the nonrotating case with the same description of gravity, despite the fact that centrifugal support allows for a larger average shock radius and correspondingly higher mass in the gain layer (Fig. 8). One might therefore conclude that rotation as considered in our Models M15LS-rot and M15LS-rot9 does not improve the conditions for an explosive runaway compared to nonrotating models in which low SASI modes are able to develop (this comparison turns out to be reversed, if such modes are suppressed in the nonrotating case by a constraining choice of the grid setup; see Fig. 15 in Buras et al. 2006b).

A reliable assessment of the influence of rotation on the development of an explosion, however, requires a continuation of simulations like Model M15LS-rot9 to later times. Centrifugal effects were predicted to lead to a reduction of the critical neutrino luminosity for the revival of the stalled shock near the polar axis (see the linear analysis by Yamasaki & Yamada 2005). The effect grows strongly with higher angular momentum of the accreted matter. In combination with the fact that rotationally deformed neutron stars produce enhanced luminosities and/or higher mean energies for neutrinos radiated in the polar direction (Janka & Mönchmeyer 1989a,b; Kotake et al. 2003), this might imply more optimistic conditions at very late postbounce times when material with higher angular momentum from larger initial radii arrives at the accretion shock.

3.5.3. Nonrotating Models M15LS-2D and M15HW-2D

The comparison of Models M15LS-2D and M15HW-2D yields information about the influence of the neutron star EoS, which determines many aspects of the post-bounce evolution, most importantly the compactness of the nascent neutron star and the properties of the radiated neutrinos.

The HW-EoS used in Model M15HW-2D is clearly stiffer and the neutron star consequently less compact (see Figs. 1 and 6). The neutrino luminosities and mean energies are therefore lower (Fig. 1 and the bottom panel of Fig. 14), which leads to a correspondingly

reduced heating rate and heating efficiency in the gain layer (Fig. 8), a much longer heating timescale, and thus also to a smaller timescale ratio (Fig. 7).

While in the 1D simulation with the HW-EoS the shock position follows the behavior of the neutron star radius and expands to a larger distance from the center than in the 1D model with the LS-EoS (see Fig. 1 and Eq. (1)), the situation is different for the 2D runs. Here the sloshing of the shock in Model M15HW-2D reaches a clearly smaller amplitude than in Model M15LS-2D during most phases of the computed ~ 400 ms of post-bounce evolution. This is particularly obvious between 200 and 300 ms after bounce and points to a significantly lower strength of the SASI activity (for more details, see Marek, Janka, & Müller 2008). An inspection of the kinetic energies in Fig. 9 (upper left panel) supports this conjecture, and a quantitative evaluation reveals that the $l = 1$ and $l = 2$ SASI modes reach only 20–30% of the power they have in Model M15LS-2D. In fact, the SASI activity in Model M15HW-2D grows considerably more slowly and the low-mode power is orders of magnitude smaller than in Model M15LS-2D until nearly 200 ms after bounce (see also Marek et al. 2008).

This suggests that the compactness of the forming neutron star has a very strong influence on the growth and strength of the SASI and of convective activity in the gain layer, either directly by the conversion of gravitational binding energy to kinetic and internal energy in the accretion flow, or indirectly via the effects of larger luminosities and mean energies of the neutrinos radiated during the period of mass accretion and thus stronger neutrino heating. A more rapidly contracting and more compact neutron star is obviously more favorable in this context. Such a behavior could have different reasons, for example a softening of the EoS in the interior of the nascent neutron star as a consequence of a microphysical phase transition that is triggered by evolutionary changes (gravitational settling, neutronization, heating due to compression and conversion of electron degeneracy energy to thermal energy) in the star. We therefore emphasize that more favorable conditions for an explosion during the post-bounce accretion phase of the forming neutron star neither require a lower value of the incompressibility modulus of the EoS for nearly symmetric matter at saturation density, nor are they directly linked to the EoS properties around bounce, which affect the shock formation and prompt shock propagation but not necessarily the long-time evolution of the accretion shock.

The gradual growth of relevant parameters (heating rate, timescale ratio, kinetic energy in the gain layer, etc.) towards the end of the computed evolution appears promising for the possibility of an explosion in Model M15LS-2D at later times: many properties, of this model near the termination of the run, for example the neutrino luminosities and neutrino-heating quantities, are very similar to those of our explosion model M15LS-rot at the same time. Initially Model M15HW-2D looks less optimistic than Model M15LS-2D, but there are indications that some quantities in Model M15HW-2D might reverse their trends in the long run. For example the shock radius (Fig. 6), the kinetic energy in the gain layer (Fig. 9), the SASI power, and the low-mode shock deformation (Fig. 5) exhibit a strong rise after ~ 300 ms,

which leads to an increase of the advection timescale (Fig. 7) and also of the heating in the gain layer (Fig. 8). This improvement could be a consequence of the growing compactness of the nascent neutron star. Both simulations, Model M15HW-2D and Model M15LS-2D, however, could not yet be carried on for sufficiently long evolution periods after bounce to see which differences the two employed nuclear EoSs might ultimately could make for an explosion at even later times.

3.6. Neutrino emission

In Figs. 14 and 15 we present some results on the neutrino emission of our exploding Model M15LS-rot. In spite of the deeper effective gravitational potential used in this simulation (Case R of Marek et al. 2006), the luminosities and mean energies of the radiated neutrinos at late times after bounce ($t \gtrsim 350$ ms) are slightly lower than those in Model M15LS-1D. This is again the influence of rotation, which compensates some of the consequences of the stronger gravity in Model M15LS-rot, an effect that we have already discussed in the context of comparing Models M15LS-rot and M15LS-2D, whose neutrino luminosities become very similar after 200 ms of post-bounce evolution (see lower panel in Fig. 14).

The mean energies of the neutrinos radiated from Model M15LS-rot (averaged over all observer directions relative to the rotation axis), however, do not exhibit the crossing of $\langle \epsilon_{\bar{\nu}_e} \rangle$ and $\langle \epsilon_{\nu_x} \rangle$ seen in the 1D calculations, although both mean energies get very close (compare the middle panel of Fig. 14 with the lower right panel of Fig. 1). The reason for this difference can be understood from the upper right plot of Fig. 15, which displays the mean energies of radiated neutrinos as functions of polar angle. One can see that in the vicinity of the poles (at latitudes $\theta \lesssim 30^\circ$ and $\theta \gtrsim 160^\circ$) the mean energy of muon and tau neutrinos is clearly higher than that of electron antineutrinos, while away from the poles both are very similar and near the equator their order even reverses. This, as well as the trough-like shape of the curves (which is also present in the muon and tau neutrino flux densities, see upper left panel of Fig. 15), is a consequence of the rotational deformation of the neutrospheric region as visible in the lower two plots of Fig. 15. The superimposed short-wavelength variations of the average radiated energies and of the neutrino fluxes are caused by local downdrafts of accreted matter near the poles and close to the equatorial plane. The neutrino flux production associated with such downdrafts is visible as bright spots above and around the neutrospheres in the lower left panel of Fig. 15. Near the poles, where the downdrafts penetrate deep inward and become very hot, neutrinos of all flavors are produced in the tips of these flow structures, whereas the lower points of equatorial downflows emit only ν_e and $\bar{\nu}_e$ (this explains the absence of a local maximum of the muon and tau neutrino flux density around the equator).

Because of rotation, the density and temperature gradients at the poles (Fig. 15, bottom right) are much steeper and the radial positions of all neutrospheres there are extremely close together⁷. Most importantly,

⁷ In the context of this paper we have adopted Eq. (28) of Buras et al. (2006a) for the definition of the energy-averaged neutrosphere. This means that the average neutrosphere coincides

the region where the dominant part of the flux is generated before the flux density gets diluted due to scattering losses and the growing distance from the source, is significantly below the energy-averaged neutrinosphere for muon and tau neutrinos (see the yellow areas in the right half of the lower left plot of Fig. 15). This means that before the ν_μ and ν_τ reach their neutrinosphere, they have to diffuse through an extended scattering atmosphere that acts like a high-energy filter, i.e., that is inefficient in producing more of these neutrinos, but in which energy transfers in neutrino-nucleon and neutrino-electron scatterings down-grade high-energy neutrinos in energy space and reduce the energy flux of heavy-lepton neutrinos (Raffelt 2001; Keil et al. 2003). Moreover, ν_e and $\bar{\nu}_e$ in contrast to heavy-lepton neutrinos are abundantly absorbed and emitted by charged-current β -processes and thus are more strongly created in an extended but cooler and less dense accretion layer (visible, for example, also by a significantly more extended neutrinospheres at low latitudes). Both effects in combination are responsible for the convergence or even inversion of the mean energies of the radiated $\bar{\nu}_e$ and ν_x in equator-near regions (for a discussion of this phenomenon in the context of the non-rotating 2D models, see Marek et al. 2008). Close to the poles the extreme steepness of the density gradient and the additional enhancement of the neutrinospheric fluxes of muon and tau neutrinos and antineutrinos by convection below the neutrinospheres (see next paragraph) counteract such a strong filter effect of a scattering atmosphere. The 1D models (cf. Sect. 3.1) define a case that is more similar to the equatorial regions of the rotating model: although the mass infall rate to the nascent neutron star drops strongly after the first ~ 200 ms of massive post-bounce accretion, the energysphere of muon and tau neutrinos is considerably below the neutrinosphere and the density decline below the accretion atmosphere is sufficiently gradual to establish a thick layer of frequent neutrino scatterings between the energysphere and the neutrinosphere of heavy-lepton neutrinos.

Finally, we point out that the region of convective activity inside the nascent neutron star can be discerned in the lower left plot of Fig. 15. In the left half of this figure, which shows the flux of ν_e , a pattern of green and red stripes indicates elongated convective cells that are oriented parallel to the rotation axis. This is typical of a situation in which convection is constrained by the presence of angular momentum gradients (see the discussion in Buras et al. 2006b). The cell structure becomes visible in this image, because Ledoux convection in the newly formed neutron star is driven by negative lepton number gradients and is therefore associated with variations of the neutron-to-proton ratio. Due to the short β -equilibration timescale in the optically thick regime, such variations are tightly linked to differences in the electron neutrino density as well as flux density. In the right half of the lower left image of Fig. 15, one can see that a local maximum of the ν_μ flux coincides with the outer edge of the convective region. This suggests that convection inside the proto-neutron star causes a notice-

able enhancement in particular of the transport of muon and tau neutrinos, a fact that was discussed in detail in Buras et al. (2006b).

4. NEUTRON STAR G-MODE OSCILLATIONS

Recently Burrows et al. (2006, 2007b) discovered in their two-dimensional, Newtonian core-collapse simulations that very late after core bounce the newly formed neutron star can be excited to core g-mode oscillations with amplitudes of several kilometers. Burrows et al. did not obtain neutrino-driven explosions in their simulations, but while the shock revealed violent sloshing motions due to the SASI instability, the anisotropic gas flow around the central object remained gravitationally bound and the gas continued to be accreted. After more than one second of post-bounce evolution, however, a rapid outward acceleration of the shock set in. For an $11.2M_\odot$ progenitor, for example, Burrows et al. (2007b) saw this shock revival happening about 1.1 seconds after bounce; in a $20M_\odot$ star the outward shock expansion occurred after 1.2 seconds of post-bounce accretion. In the simulations of Buras et al. (2006b), however, the same $11.2M_\odot$ model was found to explode about 200 ms after bounce by the SASI-supported neutrino-heating mechanism (see Sect. 3.3). The very late explosions in the runs of Burrows et al. were powered by the acoustic flux that was sent by large-amplitude vibrations of the neutron star into the medium surrounding the compact remnant. On travelling outward, the pressure waves steepened into shocks and dissipated their energy in the medium behind the supernova shock, thus creating the thermal energy that provided the pressure for the shock acceleration.

Burrows et al. (2006, 2007b) estimated that the acoustic energy flux generated by this gravity-wave activity of the forming compact remnant dominates the energy deposition by neutrinos in their models at times later than about one second after bounce. A sizable fraction of the accretion power is thus converted by the oscillating neutron star, which acts as a transducer, to acoustic flux instead of neutrino emission. As long as anisotropic accretion goes on, the gravity waves are further excited and the accretor produces a steady flow of acoustic energy. In order to provide a dynamically relevant rate of energy input to the shock and possibly the supernova explosion, however, the amplitude of the core g-mode oscillations must be sufficiently large at the surface of the nascent remnant; several kilometers seem to be necessary for creating an acoustic energy flux of a few 10^{50} ergs $^{-1}$ (Eq. (1) in Burrows et al. 2007c).

A closer and independent investigation of this interesting and potentially important phenomenon is highly desirable. Many questions remain to be answered, for example: Which decisive factors does the excitation of core g-modes due to turbulence and anisotropic accretion in the SASI layer depend on and how efficient can it be? How strong is the acoustic coupling between the oscillating neutron star and its surroundings and how powerful can the acoustic energy flux become? What is the cause of the sudden increase of the g-mode activity and of its driving force at late post-bounce times in the simulations of Burrows et al. (2006, 2007b)? What are the numerical requirements for tracking this phenomenon in supernova simulations, e.g., is the momentum conserving treatment of the gravity source term in-

with the “transport sphere” where the neutrinos in the bulk of the spectrum undergo the transition from diffusion to free streaming, and not with the “energysphere” where the neutrino production effectively ceases and the neutrinos decouple energetically from the stellar matter.

roduced by Burrows et al. important? What is the influence of the grid configuration (choice of coordinates) and of the grid resolution on the treatment of g-mode excitation and de-excitation? Does the phenomenon also show up in similar strength in 3D instead of 2D simulations? In fact, Yoshida, Ohnishi, & Yamada (2007) have recently explored the generation of neutron star g-modes by external SASI- and turbulence-induced pressure fluctuations. However, they extracted the boundary condition for a semi-analytic g-mode analysis from independent hydrodynamic SASI simulations. While these latter simulations were performed with Newtonian gravity, the g-mode excitation of the neutron star was discussed on the basis of a general relativistic stellar model. This approach therefore lacks consistency in many respects. Also, Yoshida et al. (2007) left crucial points unaddressed: Does the pressure fluctuation spectrum vary with different numerical resolution for the SASI calculations? How strongly does neutrino bulk viscosity damp the g-mode excitation? Is the assumed boundary condition appropriate for representing the coupling of the neutron star core and the exterior SASI layers, and how sensitive is the result to changes of this boundary condition? A serious concern of different sort was addressed in a paper by Weinberg & Quataert (2008). They calculated the damping of the primary $l = 1$ g-mode in the core of the proto-neutron star by its coupling to higher-order modes, whose short wavelengths cannot be resolved in numerical simulations. They found that the primary mode should saturate at an energy ($\sim 10^{48}$ erg) that is much too low to make acoustic power a significant energetic driver of supernova explosions.

We do not intend to fundamentally challenge here the possibility that the acoustic mechanism might work as proposed by Burrows et al. (2006, 2007b,c), because none of our simulations was continued to the late times when they see the corresponding large-amplitude g-mode oscillations of the neutron star core in their models. In the following sections we will concentrate only on two questions: Do neutron star g-mode oscillations grow to important amplitudes in our simulations and does the associated acoustic power radiated by the neutron star contribute to the shock revival seen in our models at any significant level?

4.1. Core g-modes in our model runs

In order to answer these questions, we have performed an analysis of the gravity-wave activity in the region around and below the neutrinosphere. A direct quantitative comparison of the g-mode strength in the neutron star core between our simulations and those of Burrows et al. (2006, 2007b,c) would be desirable and could be illuminating, but information suitable for this purpose is hardly available in the published papers. Figure 7 in Burrows et al. (2006), which displays a set of time-dependent l -mode amplitudes of the spherical harmonics expansion of the fractional pressure variations $[P(r, \theta) - \langle P(r, \theta) \rangle_\theta] / \langle P(r, \theta) \rangle_\theta$ at a fixed radius of 35 km, could be considered as a basis for a straightforward comparison. However, for several reasons the displayed quantity is not the most appropriate one for diagnosing the presence of g-modes in the supernova core and neutron star. (1) The mentioned figure provided by Burrows et al. was not meant to display a signature of the core g-mode

activity but was intended to reflect the pressure fluctuations in the region between neutron star and shock. The authors evoked this measure because it is a gauge of the potential of pressure fluctuations to excite core g-mode oscillations in the more quiescent interior (A. Burrows, private communication). The primary origins of these “outer” pressure fluctuations are, of course, the SASI and neutrino-driven convection, not core pulsations. Without a well understood theory of the excitation mechanism of the large-amplitude low-order g-modes in the neutron star core, however, it is unclear what the external pressure fluctuations can tell about the fluid motions to be expected inside the neutron star. (2) Moreover, pressure fluctuations are not an optimal measure of the strength of core g-mode pulsations, which rely on buoyancy as the restoring force. This is visible, for example, from the eigenfunctions of neutron star core g-modes given by Yoshida et al. (2007), where the pressure-dependent amplitude appears unspectacular while the Lagrangian displacement amplitude can still be large. (3) Pressure fluctuations as a function of time at a fixed radius do not reflect the evolution of the conditions at a certain enclosed mass, but they also include a long-time evolutionary trend due to the shrinking of the forming neutron star (and due to its growing centrifugal deformation in the case of rotating models). In particular at radii close to the boundary layer between the neutron star and the violently turbulent, SASI-perturbed post-shock region, a gradual increase of the pressure fluctuations with time does not necessarily signal a rising strength of the g-mode driving force at the surface of the neutron star core. Instead, the observed growth of the pressure fluctuations can just be a consequence of the neutron star contraction, in course of which the radial position moves out of the neutron star and deeper into the stirred SASI layer. The range of radii that is affected by this shift depends on the compactness of the neutron star and therefore on the softness of the high-density equation of state and on the depth of the gravitational potential. Since we describe gravitational effects by the effective relativistic potential, our neutron stars are more compact (in particular with the softer EoS of Lattimer & Swesty 1991) than those in the Newtonian simulations of the Tucson group. Comparing simulations performed with different nuclear equations of state and different treatments of gravity (Newtonian or relativistic) is therefore not conclusive when the same radius of evaluation is picked. Simply for this reason a detailed assessment of the similarities and differences between our simulations and those of Burrows et al. (2006) is very difficult on grounds of the limited data published.

Accordingly, an evaluation of the fractional pressure variations at different locations in the neutron stars of our simulations, guided by Fig. 7 in Burrows et al. (2006), leaves too much room for different interpretations and does not really illuminate the g-mode activity in the interior of the nascent neutron star. We therefore decided to present a variety of alternative quantities whose behavior can better reflect nonradial fluid perturbations in different regions of the supernova core.

Figures 16 and 17 show the time evolution of low-mode spherical harmonics amplitudes (for $l = 1, \dots, 5$, defined in agreement with Eq. (3)) of the velocity perturbations, $v_r(r, \theta) - \langle v_r(r, \theta) \rangle_\theta$, in the central regions of

Models M15LS-rot and M15LS-2D, the former figure between the neutron star center and a radius of 60 km, the latter figure at the positions where the laterally averaged density has values of $\langle \rho \rangle_\theta = 10^{11} \text{ g cm}^{-3}$ and $10^{14} \text{ g cm}^{-3}$. It is obvious that the interior of the neutron star at high densities, where the second density location is chosen to be, is much more quiet than the environment of the neutron star and its surface-near layers, which are represented by the first value of the density. The stellar plasma in the neutron star surroundings is stirred by the violent SASI and convective overturn motions, which instigate g-mode activity in the outer layers of the compact remnant. Figures 16 and 17 reveal that the maximum amplitudes of the velocity perturbations deep inside the neutron star are of the order of 10^7 cm s^{-1} , whereas they are up to a factor 100 higher in the SASI region and adjacent shells. The larger values in Model M15LS-rot compared to Model M15LS-2D are a consequence of the rotational flattened compact remnant in the former simulation, which causes the radius for $\langle \rho \rangle_\theta = 10^{11} \text{ g cm}^{-3}$ to reach deeper into the SASI-perturbed layer above the poles of the neutron star.

One should note that the contour for an average density of $10^{14} \text{ g cm}^{-3}$ is located near the inner edge of the convectively unstable shell inside the neutron star, at the transition of this layer to the convectively stable region closer to the center (roughly at $r \sim 10 \text{ km}$). A major fraction of the activity seen at this location is therefore linked to convection and convective overshooting and not to pure gravity waves, but the maximum amplitudes are in the range typically found also at positions deeper inside the core. In Model M15LS-2D the dipole amplitude of the velocity perturbations exhibits a characteristically different low-frequency modulation, which is absent in Model M15LS-rot (see Fig. 17 for $\langle \rho \rangle_\theta = 10^{14} \text{ g cm}^{-3}$), where it is also more difficult to discern the convective region inside the neutron star (Fig. 16). This can probably be explained by the nature of convection in rapidly rotating neutron stars, where due to the Solberg-term in the instability criterion the convective cells are constrained to tube-like, narrow structures oriented parallel to the rotation axis and located in regions where the angular momentum gradient is flat (see also Sects. 3.2.1 and 3.6). The effects of the convection in such an environment are therefore strongly damped compared to the nonrotating case.

Interestingly, at a given density and time, all modes from $l = 1$ to $l = 5$ are similarly strong, with a tendency of slightly (roughly a factor of two) higher amplitudes for $l = 3, 4, 5$ (Fig. 17). In the innermost core of the neutron star (at $r < 10 \text{ km}$) the opposite effect is present and the difference of the amplitudes is larger: the amplitudes for $l = 1$ and $l = 2$ are the clearly dominant ones during most of the post-bounce evolution, $l = 3$ is intermediate, and $l = 4, 5$ are significantly weaker.

Consistent with the activity level observed in the velocity perturbations, we also find very small fractional density variations at given positions, at most some tenths of a percent in the neutron star interior and about 10% just outside of the neutrinosphere. There is no sign of any significant coherent movement of the neutron star core as suggested by Fig. 3 in Burrows et al. (2007c), where the isodensity surfaces show large relative displacements of their geometrical centers instead of being concentric.

In order not to just rely on a potentially misleading interpretation of local fluctuations of the mentioned quantities, we have also evaluated Models M15LS-rot and M15LS-2D for the time-dependent variations of the radial positions of certain density values in chosen directions (Fig. 18). In the case of a coherent translatory movement of some core region, which for symmetry reasons in the 2D simulations has to occur along the z -axis of the polar grid, this would also be a rough measure of spatial shifts of the geometric center of isodensity surfaces. Such variations are not found on the scale of the plots in Fig. 18 for matter at densities above $\rho > 10^{11} \text{ g cm}^{-3}$, while they are around 0.5–1 km for densities between $5 \times 10^{10} \text{ g cm}^{-3}$ and $10^{11} \text{ g cm}^{-3}$ and even larger only for lower densities outside of the neutron star⁸. There, however, they originate from the SASI and convective overturn activity, which also stirs the neutron star surface layer below. This interpretation is consistent with the fact that one detects radius variations with the same behavior and similar or even larger magnitude in equator-near regions, where violent downflow activity is also observed during the accretion phase of the stalled shock (Sect. 3). A direct inspection of the geometrical centers of the isodensity surfaces for the density values considered in Fig. 18 reveals full agreement with the message and quantitative information in this figure: the geometrical centers exhibit z -displacements relative to the coordinate center of less than $\sim 0.1 \text{ km}$ for densities above $10^{11} \text{ g cm}^{-3}$, at most 0.2 km for $\rho = 10^{11} \text{ g cm}^{-3}$, some 0.1 km for $\rho = 5 \times 10^{10} \text{ g cm}^{-3}$, and 1–3 km only for $\rho \lesssim 10^{10} \text{ g cm}^{-3}$. Taking all together we again conclude that there is no evidence for large-amplitude core g-modes in the deep interior of the nascent neutron star in our simulations.

4.1.1. Acoustic energy input to explosion

Although core g-modes do not seem to play a significant role in the discussed models, the surface gravity waves caused by the impact of accretion downflows in the outer layers of the neutron star could still be an important source of sonic waves and secondary shocks, which could contribute energy input to the developing explosion. Because of the violently turbulent and time-dependent conditions in the neutron star surroundings, but also because of the possibility to liberate or absorb energy by changes of the composition of the stellar gas, it is quite difficult to assess in a quantitatively reliable way how important this energy input rate really is. Burrows et al. (2006, 2007c) therefore refer to a crude analytic formula that sensitively depends on the product of several factors whose values are not well constrained by the numerical results (see Eq. (1) in both papers). For checking the plausibility of their assumptions they compare their estimated numbers with the available rate of energy release from gas accretion onto the forming neutron star.

⁸ It is important to note that in Fig. 18 in contrast to Fig. 17, the evaluation is not performed at the position of a laterally averaged density value, but at the local density in a chosen direction. In the case of a rotationally deformed neutron star the polar radius for a certain density is significantly smaller than the radius that corresponds to the same value of the lateral density average. The former position is therefore close the neutron star surface, while the latter position is deeper in the SASI-perturbed surroundings of the neutron star.

Our approach here is different. Making use of our hydrodynamical results, we attempt to estimate the rate of acoustic energy transfer to the ejected matter by sound waves, \dot{E}_{sw} , as the difference of all other energies that play a role in the evolution equation for the volume integral of the total (i.e., internal plus kinetic plus gravitational) energy in some region behind the supernova shock. During the phase of simultaneous accretion and outflow of matter (stage (2) described in Sect. 3.4) one can write:

$$\begin{aligned} \dot{E}_{sw} &\approx \partial_t E_{tot} \\ &+ \oint_{S|v_r>0} d\Omega r^2 v_r \left(\varepsilon_{int} + P + \varepsilon_{kin} - \frac{GM\rho}{r} \right) \\ &- \zeta \int_{V_g} dV \rho \dot{q}_\nu - \oint_{S|v_r>0} d\Omega r^2 v_r \rho e_{bind}^{acc} \\ &\equiv \partial_t E_{tot} + L_{out} - \zeta \dot{Q}_\nu - L_{bind}^{acc}, \end{aligned} \quad (12)$$

where for simplicity (and to a very good approximation) we assume a spherically symmetric, Newtonian gravitational potential. In this equation E_{tot} is the total energy in the volume of integration, v_r the radial velocity component, ε_{int} and ε_{kin} the densities of internal and kinetic energy, respectively, P the gas pressure, ρ the mass density, \dot{q}_ν the local rate of neutrino energy deposition, $d\Omega r^2$ is the surface element for the surface integrals, and dV the volume element for the volume integrals. The surface integrals are carried out over a sphere $S(r)$ at radius r , which is located behind the shock in all parts. The integration includes only material that flows through this sphere with positive radial velocity, a constraint that is indicated by $S|v_r > 0$. The volume integration, which also leads to E_{tot} , has to be performed over the matter that fills the volume between the direction-dependent gain radius, $R_g(\theta)$, and the radius r , and which is ultimately able to leave the gain layer through the surface $S(r)$ with positive radial velocity. The radius r is chosen large enough so that the neutrino energy deposition at bigger radii is negligibly small. If the volume integration was done for *all* matter in the gain layer, i.e. over the whole volume V_g , an extra term would have to be introduced into Eq. (12) to account for the energy loss associated with matter that is advected inward through the gain radius to be accreted onto the neutron star. Because of the highly turbulent flow around the gain radius and the corrugated structure of the gain surface, it is very difficult to evaluate the corresponding surface integral. We therefore avoid this term and instead introduce the factor ζ defining the fraction of the neutrino energy that is deposited in the material swept up by the shock and ultimately ending up as ejected matter (see Eq. (6) and associated discussion). One can relatively easily obtain a time-averaged number for ζ by comparing the mass accretion rate through the shock and the growth rate of the mass below the gain radius.

The first term on the rhs describes the gain of energy in the integration volume, the second term the loss of energy by ejecta mass leaving the surface $S(r)$, the third term the total energy input to the ejecta by neutrino heating, and the last term accounts for the fact that energy input by neutrinos (and possibly other sources like sound waves) does not only have to yield the positive energy carried by the ejecta, but has to provide also the energy

to overcome the gravitational binding of the progenitor gas that enters the gain layer through the shock. Referring to the detailed arguments given in Sect. 3.4, we calculate the internal energy always such that all baryons are assumed to be assembled in iron-group nuclei. This allows us to ignore in Eq. (12) additional terms that describe the sizable amounts of energy that can be exchanged between the reservoirs of rest-mass and internal energy by processes altering the nuclear composition of the medium, i.e. by nuclear burning and photodissociation of nuclei in the accretion flow and by nucleon recombination in the outflow. The quantity e_{bind}^{acc} in the last term on the rhs of Eq. (12) is the (negative) specific binding energy (computed again as the sum of the specific internal, kinetic, and gravitational energies) of matter that flows in accretion funnels from the shock through the surface $S(r)$ towards the neutron star. This energy — with the nuclear binding energy included as mentioned before — is typically around -1 to -2 MeV per nucleon during the considered accretion phase. It is roughly constant when the gas falls inward, because the energy absorbed from neutrinos is relatively small when the matter is still located at large distances from the neutron star and is also small when the accretion flows move with high velocities and thus are exposed to neutrino heating only for a very short period of time. Therefore its value is not very sensitive to the radius where it is determined⁹.

We have performed the evaluation for Model M15LS-rot in a time interval around 690 ms after bounce near the end of our simulation. At this time the mass accretion rate through the shock is $\dot{M}_{acc} \sim 0.23 M_\odot s^{-1}$ and the gas accretion onto the neutron star is still going on. A time-averaged fraction of $\zeta \sim 0.4$ – 0.5 of the infalling mass is fed back into the outflow of ejecta, and the conditions in the region between the gain radius $R_g(\theta)$ and the radius r of the sphere S can be assumed as nearly stationary, in which case $\partial_t E_{tot} = 0$ is a reasonably good approximation. Nevertheless, there are still significant time variations in the different terms in Eq. (12). For a mass outflow rate through S of $\dot{M}_{out} \sim \zeta \dot{M}_{acc} \sim 0.05$ – $0.1 M_\odot s^{-1}$ ($\sim \dot{M}_{gain}$, the growth rate of the mass in the gain layer), we obtain an outflow luminosity of $L_{out} \sim (9$ – $14) \times 10^{50} \text{ erg s}^{-1}$ and a flow rate of gravitational binding energy associated with the infalling and reejected mass of $L_{bind}^{acc} \sim \dot{M}_{out} \langle e_{bind}^{acc} \rangle \sim -(1.5$ – $3) \times 10^{50} \text{ erg s}^{-1}$ (we find an average value of $\langle e_{bind}^{acc} \rangle \sim -1.5$ MeV per nucleon in the accretion funnels of Model M15LS-rot). With a relevant neutrino energy deposition rate of $\zeta \dot{Q}_\nu \sim (10$ – $15) \times 10^{50} \text{ erg s}^{-1}$ the rhs of Eq. (12) yields an upper limit for additional energy input to the developing explosion by acoustic waves of $(0.5$ – $2) \times 10^{50} \text{ erg s}^{-1}$. The acoustic energy flux originating from the violent fluid motions caused by the impact of accretion flows near the neutron star surface is therefore at least a factor of ~ 10 lower than the energy deposition by neutrino heating in our simulations. Until 700 ms after bounce there is no convincing evidence of any significant energy transfer to the shock by pressure waves

⁹ Bernoulli's theorem implies that the constant energy functional includes the specific enthalpy $w = (\varepsilon_{int} + P)/\rho$ instead of the specific internal energy. Thus the constant quantity is actually $e_{bind}^{acc} + P/\rho$ and not e_{bind}^{acc} . This difference, however, is not essential for our discussion.

originating from the neutron star. Our $15 M_{\odot}$ model M15LS-rot as well as the $11.2 M_{\odot}$ progenitor investigated by Buras et al. (2006b) and in this paper (Sect. 3.3) develop neutrino-powered explosions long before the acoustic mechanism was found to cause an explosion in the simulations of Burrows et al. (2006, 2007a,c).

4.1.2. Momentum conservation

But is our code actually able to follow the excitation and evolution of core g-mode oscillations, in particular of $l = 1$ type, in which case the gas in the stellar center participates in the motion? Since a few radial zones in the central $\lesssim 1.7$ km of our numerical grid are treated in spherical symmetry (to get around too restricted CFL timesteps), one might wonder whether a flow pattern with gas motion through the stellar center can be reasonably well described. Such a spherical core might create severe perturbations, for example because the central mass, which cannot move out of the grid center, absorbs linear momentum and thus may cause a significant violation of momentum conservation. In Fig. 19, left plot, the evolution of the total linear momentum of the whole gas on the computational grid (about $2 M_{\odot}$, of which about three quarters are contained in the neutron star) is shown for Model M15LS-rot. The right plot of this figure displays the corresponding displacement that the center of mass of the gas experiences relative to the grid center in the direction of the polar grid axis (which coincides with the rotation and symmetry axis of the 2D model).

The quantities in Fig. 19 exhibit variability on two timescales, which can be easily discerned. A long-period modulation with a typical frequency of 30–80 Hz (timescales of roughly 15–30 ms) is the consequence of the SASI sloshing and convective overturn in the postshock layer (cf. Fig. 5) and the corresponding changes of the mass distribution around the neutron star. This effect is superimposed by high-frequency fluctuations with periods of only milliseconds, which is the typical timescale of small-scale mass motions in the close vicinity of the neutron star and of gravity waves in the neutron star surface and core. Correspondingly, the linear momentum along the z -axis changes its sign with a frequency of several 100 Hz and the associated net displacement is tiny. Slightly larger, but still very small is the displacement caused by the low-frequency variations: the center of mass of the whole gas wobbles around the grid center with an amplitude of usually less than 50 meters, which is much smaller than the radius of our innermost grid cell (300 meters). The separation of the center of mass from the grid center grows larger only when the outward shock expansion becomes very strong and the postshock layer gets inflated with a pronounced global deformation at $t \gtrsim 600$ ms (see Fig. 4). A clear trend in one direction seems to be established towards the end of the computational run (with a final displacement, however, that is still only insignificantly bigger than the first radial grid zone) as a consequence of the clear dipolar asymmetry of the accelerating postshock gas, which attains more momentum in the southern hemisphere (bottom right panel in Fig. 4). We observe a very similar behavior in the case of our $11.2 M_{\odot}$ explosion model, where the z -momentum in the northern hemisphere dominates when the simulation is terminated. The momentum asymmetry of the supernova gas could ultimately

imply a sizable recoil of the neutron star in the opposite direction, which should drive the neutron star away from the coordinate center (possibly leading to numerical problems), but our simulations are not carried on long enough to be conclusive. In Model M15LS-rot the velocity of the compact remnant is only $\sim 20 \text{ km s}^{-1}$ at $t = 700$ ms after bounce, and in the $11.2 M_{\odot}$ model it is 6 km s^{-1} at 300 ms after bounce; the final neutron star kick will be determined only seconds after the onset of the explosion (see Scheck et al. 2006).

A significant drift of the neutron star away from the origin of the grid is likely to lead to numerical problems, because the gravity solver as well as the treatment of the neutrino transport are written for a centrally condensed mass in a polar coordinate grid. Until the end of our simulations, however, neither this problem nor violation of momentum conservation are a serious concern.

Another conceivable restriction of our simulations might be connected to our use of a relativistic monopole potential, whose dominant contribution to the gravitational potential of the neutron star prohibits an accurate response of the gravitational field to the nonradial asymmetry of the mass distribution caused by the SASI oscillations, convective mass motions, and gravity waves. One should note here, however, that we still have included the higher multipoles of the gravitational potential in their Newtonian form, and thus our treatment of the gravitational effects is certainly much less constraining and much less approximative than the so-called Cowling approximation. The latter is widely used for discussing stellar pulsations in the linear regime, although it ignores the influence of the oscillation-induced density variations on the gravitational field.

4.2. Core g-mode tests

In order to test whether our code can handle $l = 1$ core g-modes with large amplitudes in the neutron star if they were excited (e.g. hydrodynamically by pressure variations around the neutron star surface due to anisotropic accretion flows), we artificially instigated a large dipole g-mode by imposing an $l = 1, n = 1$ perturbation (i.e., we assumed one radial node) of the z -component of the velocity field at a time late after bounce (alternatively, we also tested an $l = 1, n = 2$ mode with two radial nodes, obtaining similar results). The velocity field was imposed with a constant absolute value on the matter within a radius of 50 km. It was chosen such that the linear momentum associated with this perturbation was zero (the node was therefore initially located at 15 km). The once perturbed model was followed in its evolution with all (micro)physics being the same as in the long-time supernova runs. For exploring the response to g-modes with different energies, we varied the amplitude of the imposed velocity perturbation by a factor of four, using values of 500 km s^{-1} and 2000 km s^{-1} , corresponding to kinetic energies of 3.7×10^{48} erg and 5.9×10^{49} erg, respectively.

Figure 20 displays results of two such tests in the case of Model M15HW-2D. It shows the time evolution of several low- l mode amplitudes of the spherical harmonics decomposition of the radial velocity field, $(v_r(r, \theta) - \langle v_r(r, \theta) \rangle_{\theta})_{\theta}$, at a chosen radius of 10 km (left panel) and for the $l = 1$ case in the central region with 60 km radius (right panel; for comparison we provide

there also the dipole amplitude of the fractional pressure variations, $(P(r, \theta) - \langle P(r, \theta) \rangle_\theta) / \langle P \rangle_\theta$. One can see that after an initial, short relaxation (caused by the fact that our chosen velocity perturbation did not correspond to an eigenfunction) an essentially pure dipole mode is present with a clean periodicity. The amplitudes of the radial velocity variations are a factor of 10–20 larger than those that we find for the core g-modes in our supernova runs (see Figs. 16 and 17).

The test model with the lower g-mode energy (which is computationally cheaper) was run for many cycles and shows a decrease of the oscillation amplitude at a fixed radius of 10 km by approximately a factor of two on a timescale of about 18 ms, but this decay slows down later. In principle, there can be different reasons for this damping. The central 1D region, though small, might brake the motion because there might be friction and dissipative losses caused in the 2D flow around the central 1D core. This possibility, however, seems to be ruled out for the core sizes chosen and the numerical resolution employed, because test runs with a core radius of 0.8 km instead of 1.7 km and with a full 2D treatment (i.e., no 1D core and thus painfully tiny computational timesteps) show the same frequency, amplitude, and damping behavior (Fig. 20, left lower panel). Only when the radius of the central 1D core is increased to ~ 3 km we can observe a slightly faster damping and a gradually decreasing oscillation frequency.

Another possible reason for the initial damping is the reconfiguration of the mode pattern due to the fact that the imposed perturbation does not correspond to an eigenfunction. This means that oscillation energy will be redistributed within several pulsation periods and therefore amplitude damping is observed in some regions while the amplitudes in other regions increase. We find damping in the whole volume of the neutron star up to a radius of ~ 30 km, so that the motion outside should be amplified. The right panels of Figure 20 indeed reveal such a trend. In contrast, hardly any energy is transferred from the $l = 1$ mode to higher modes (in spite of unavoidable numerical coupling), whose amplitudes remain very small in the whole perturbed volume of the neutron star (Fig. 20, left panel).

Yet another reason for the observed damping, probably enhanced by the just mentioned growth of the g-mode amplitude near the neutron star surface, is the acoustic energy flux that is sent by the moving neutron star into its surrounding medium. Assuming that this ultimately is the most efficient channel for energy loss of the ringing neutron star, we can obtain an upper limit for the corresponding rate of energy outflow. Since roughly 75% of the initial mode energy are lost within 18 ms, we estimate an acoustic energy flux of $\sim 1.5 \times 10^{50}$ erg s $^{-1}$, comparable to the value stated by Burrows et al. (2007c). For the g-mode activity and amplitudes observed in our supernova runs the energy flux from the oscillating neutron star must be expected to be smaller and thus can only make a small addition to the neutrino energy deposition behind the shock, in agreement with our conclusions based on the estimates in Sect. 4.1.1.

The test calculation with the larger excitation amplitude was computationally expensive because of bigger oscillation-induced variations of the thermodynamic quantities that led to shifts of the β -equilibrium between

neutrinos and the stellar gas. The resulting high neutrino source terms enforced small timesteps in the neutrino transport. The test run was therefore continued only for about three full oscillation cycles, but the evolution visible in the upper left panel of Fig. 20 agrees nicely with the run for the reference case.

These tests give us confidence that our long-time simulations should be able to trace also large-amplitude core g-modes, if an efficient mechanism was driving their excitation. We have no reason to suspect that our numerical code might fail to describe the hydrodynamic driving due to turbulence and anisotropic accretion that Burrows et al. (2006, 2007a,c) consider as responsible for instigating the large core g-modes in their models (see also Yoshida et al. 2007). Therefore we are tempted to conclude that until the end of our simulations the conditions for such an efficient excitation of gravity waves in the neutron star core do not seem to be present in the supernova center.

5. DISCUSSION AND CONCLUSIONS

We have presented evidence from our 2D neutrino-hydrodynamic stellar core-collapse simulations that the neutrino-driven mechanism may explain the explosions of progenitor stars in a wider range of masses. In this work we considered a $15 M_\odot$ progenitor (s15s7b2 of Woosley & Weaver 1995) and an $11.2 M_\odot$ model (Woosley et al. 2002). The former is a typical representative of supernova progenitors in the intermediate mass range between somewhat more than $10 M_\odot$ and around $20 M_\odot$, the latter is more typical of stars near the lower mass end of supernova progenitors with iron cores. A neutrino-driven explosion of the $11.2 M_\odot$ star was found before in a 2D simulation by Buras et al. (2006b). Results of a continuation of this run were also discussed here. Similar to the explosion obtained for the $11.2 M_\odot$ star, the delayed shock revival by neutrino heating in the $15 M_\odot$ model was fostered and enabled by the presence of a strong, low-mode SASI oscillations of the postshock layer¹⁰. The SASI modes grow rapidly in the accretion flow to the neutron star even at conditions where buoyancy instabilities are damped in the rapidly infalling gas behind the accretion shock and therefore convection in the gain layer is initially weak (see Fogliizzo et al. 2006, Scheck et al. 2008).

The SASI has two crucial consequences, which are favorable for the possibility of neutrino-driven explosions. On the one hand, the violent sloshing motions of the postshock layer with fast expansion and contraction phases of the shock create steep entropy gradients in the postshock flow, which lead to powerful secondary convection and thus efficient overturn of the gas in the gain region (for a detailed discussion, see Scheck et al. 2008). On the other hand, the SASI also pushes the shock to a larger average radius. This reduces the mean accretion velocity in the gain layer (because the velocity in the infall region ahead of the shock drops inversely with the square root of the shock radius) and thus increases the advection timescale of gas from the shock to the gain

¹⁰ Although our successful explosion for the $15 M_\odot$ star was obtained in a simulation in which we had imposed angular momentum on the progenitor model, our comparison with the other simulations for this progenitor suggests that the presence of rotation was not essential for the development of the explosion (see Sects. 3.5.2 and 3.5.3).

radius. The accreted matter is therefore exposed to neutrino heating for a longer time, a fact that is reflected by a significant increase of the critical ratio of the advection timescale to the neutrino-heating timescale. A strong SASI activity has the consequence that this timescale ratio comes much closer to the value of unity, signaling favorable conditions for a neutrino-driven explosion. The combination of these effects indeed turned out to drive the $15 M_{\odot}$ model (specifically our Model M15LS-rot) towards a runaway instability at about 600 ms after core bounce, while for the $11.2 M_{\odot}$ star this happened roughly 200 ms after bounce.

Unfortunately, due to the considerable demand of computer time with the high numerical resolution needed for converged results, we were so far not able to continue our simulations to the phase where the blast is fully developed and the explosion energy can be determined from our computations. However, several factors are indicators that the $15 M_{\odot}$ Model M15LS-rot considered here just like the investigated $11.2 M_{\odot}$ model is in the process of undergoing the transition from collapse to successful outburst. This is suggested not only by the rapidly accelerating expansion of the shock radius near the end of the simulations and by the fact that the critical timescale ratio exceeds unity permanently with rapidly growing value. It is also suggested by a continuous trend of increasing energy in the gain layer. Before Model M15LS-rot was stopped, a significant and growing gas mass in the gain layer had obtained a positive specific energy and was thus ready to become gravitationally unbound and to promote further outward propagation of the shock against the gravitational pull of the neutron star. The mean shock radius has already reached about 600 km. This is sufficiently large for the temperature in the postshock ejecta to be so low that considerable nucleon recombination to α -particles has set in and for the gas swept up by the shock to be so cool that heavy nuclei do not experience complete dissociation any longer. The release of nuclear binding energy and the reduction of dissociation energy allow for a higher pressure behind the shock and support the shock expansion. Last but not least, the shock has entered the progenitor layer (at about 500 km) where silicon is not yet burned to iron, and its most extended parts reach the shell where oxygen is still unburned (at ~ 700 km). According to Bruenn et al. (2006) and Mezzacappa et al. (2007), shock-initiated nuclear burning and the reduced ram pressure in these layers will assist the ongoing strong neutrino heating in driving the explosion. For all these facts we do not see any reason to suspect that the outward acceleration of the shock near the end of our simulated Model M15LS-rot might break down again.

The energy of such SASI-supported, neutrino-driven explosions is not determined at the moment when the runaway sets in. Instead, accretion of gas towards the gain radius and the neutron star can proceed at the same time as shock acceleration sets in due to the expansion of rising, neutrino-heated, buoyant gas. This characterizes the generically multi-dimensional nature of the developing explosion. The ongoing accretion continuously channels fresh material, which is swept up by the shock, to the region near the gain radius, where neutrino heating is strongest. Roughly half of the gas penetrates to the cooling layer below the gain radius and ultimately settles

onto the neutron star, the other half absorbs with high efficiency energy from the neutrinos radiated by the neutron star. This gas turns around and rises again, driven by buoyancy forces, and contributes to the energy of the explosion. Our estimates show (and hydrodynamic simulations by Scheck et al. 2006 have demonstrated) that simultaneous accretion and shock acceleration can go on for many hundred milliseconds and therefore the final explosion energy can only be determined by computations that cover a much longer time evolution than we were able to follow in our current simulations. Our analytic considerations, based on the situation at the beginning of the explosion, reveal that the $11.2 M_{\odot}$ model can be expected to develop an explosion energy of several 10^{50} erg, while due to the higher mass accretion rate the canonical value of 10^{51} erg is well in reach of the considered $15 M_{\odot}$ star. The final explosion energy should increase sensitively when the initial expansion of the shock is relatively slow and when the progenitor maintains an appreciable mass accretion rate for a longer time.

Because the onset of the discussed SASI-supported neutrino-driven explosions for 11.2 and $15 M_{\odot}$ stars is considerably delayed, the neutrino-heated gas mass in the gain layer at the time when the blast takes off is fairly low and therefore a powerful gas ejection has to rely on a longer lasting phase of simultaneous accretion and outflow. The possibility of such stable accretion with downflows from one (or more) direction(s) and gas outflow in the other direction(s) was indeed seen in the simulations of Scheck et al. (2006). The significance of this generically multi-dimensional phenomenon in powering the explosion to completion and in achieving the necessary energies contradicts the concept of supernovae being energized by a spherically symmetric neutrino-driven wind as suggested by Burrows & Goshy (1993). This has been realized recently also by Burrows et al. and was advocated by them in the context of the acoustic explosion mechanism (Burrows et al. 2007c), which requires the accretion of gravitational/mechanical energy, and in the context of magnetohydrodynamical explosions (Burrows et al. 2007a), which require the accretion of differential kinetic energy.

The strong shock acceleration, which we found to begin about 200 ms after bounce in the $11.2 M_{\odot}$ progenitor and at 600 ms after bounce in the investigated $15 M_{\odot}$ model, is associated with a large dipolar deformation of the shock. This is a clear indication for the dominance of the lowest nonradial SASI mode at the onset of the runaway. It suggests that the developing explosion is likely to be very asymmetric, similar to the artificially initiated neutrino-driven explosions that were computed by Scheck et al. (2006) and led to neutron star kick velocities (with maximum values of more than 1000 km s^{-1}) in agreement with measurements. Also the large-scale anisotropies and mixing processes that can be found in many supernovae and that seem to determine the appearance of their gaseous remnants might be a consequence of the pronounced asymmetry of the developing blast waves in our simulations (see Kifonidis et al. (2006) for studies of the long-time evolution of anisotropic neutrino-driven explosions).

We compared 2D models with and without rotation and with a stiff and a soft nuclear equation of state. Moreover, we tested the influence of different prescriptions of

the effective relativistic gravitational potential in our approximation to fully relativistic calculations. We found that a nascent neutron star that contracts faster and is more compact, which typically happens in the case of a softer high-density equation of state (or a stronger gravitational potential), has a favorable influence on the SASI-supported neutrino-driven mechanism. This is a consequence on the one hand of a more rapid growth of low SASI modes, amplified by the release of gravitational binding energy, and on the other hand of higher luminosities and mean energies of the emitted neutrinos during the accretion phase and correspondingly stronger neutrino heating in the gain layer. The latter also supports the development of violent SASI and convective activity in the postshock region. We stress that the EoS properties that lead to a faster compactification of the nascent neutron star during its post-bounce accretion do not need to be linked to the EoS characteristics at core bounce or to the value of the incompressibility modulus of symmetric nuclear matter at saturation density. The evolutionary changes in the interior of the remnant could also trigger a softening of the EoS by a reduction of the adiabatic index, e.g., as a result of a phase transition.

Rotation, in contrast, can be diagnosed to have the opposite effect. Although centrifugal support leads to a larger average shock radius, a longer advection timescale of the matter falling through the gain layer, and a reduced binding energy of accreted matter, these helpful effects are more than compensated by lower luminosities and mean energies of the neutrinos radiated by the significantly more extended and cooler rotating proto-neutron star. The overall neutrino heating and heating efficiency found in rotating models is considerably lower and the neutrino heating timescale in the gain layer correspondingly longer. The critical ratio of advection timescale to heating timescale therefore signals less favorable conditions for an explosion in comparison to a nonrotating model with otherwise the same physics. This pessimistic judgement of the role of rotation is opposed by the assessment of Yamasaki & Yamada (2005), who found by linear analysis that sufficiently rapid rotation leads to a reduced critical neutrino luminosity for shock revival in the polar direction. Simulations for longer postbounce times are needed to obtain conclusive information about this possibility.

Although we clearly see the presence of gravity-waves in the newly formed neutron star, we cannot detect any important influence on the dynamical evolution of the beginning supernova explosion. On the one hand, the amplitudes of core g-mode oscillations in our supernova runs remain very small. On the other hand, the estimated flux of acoustic power associated mainly with the considerable surface gravity-wave activity is dwarfed by the rate of the neutrino energy deposition. The small amplitudes of core g-modes found in our models are not in disagreement with the calculations of Burrows et al. (2006, 2007b,c), who discovered violent neutron star core motions only at very late times ($t \gtrsim 1$ s) after core bounce, which we are unable to reach in our simulations.

We convinced ourselves by numerical tests with artificially instigated large-amplitude core g-mode vibrations that our supernova code is well able to capture this effect even in the case of sizable core displacements (of order one kilometer and more). Moreover, we do not see any

reason to suspect that our numerics could be unable to track the g-mode excitation by pressure fluctuations due to anisotropic accretion and turbulence in the SASI layer, in particular since we make sure to have good numerical resolution inside the neutron star as well as in the region between the neutron star and the shock. Both facts together make us confident that we should observe large-amplitude core pulsations if the physical conditions were present to drive their excitation.

The $11.2 M_{\odot}$ and $15 M_{\odot}$ simulations discussed in the present work suggest that — at least in this mass range of progenitor stars — the SASI-aided neutrino-driven mechanism can lead to explosions significantly earlier than the acoustic mechanism proposed by Burrows et al. (2006, 2007b,c), a possibility that is not challenged by the latter authors. Naturally, our simulations, which had to be terminated at latest ~ 700 ms after bounce, do not allow us to make any statement about the neutron star g-mode activity at even later times (with the potential to pump additional energy into the already launched blast), nor can we exclude a potentially important role of the vibrating neutron star as an acoustic energy source for triggering the explosion in cases where the neutrino-driven mechanism is too weak and the explosion is as delayed as observed by Burrows et al. (2006, 2007b,c).

Neutrino-driven explosions have recently been also found in 2D simulations with sophisticated, energy-dependent neutrino transport by Bruenn et al. (2006) and Mezzacappa et al. (2007). Their calculations for $11 M_{\odot}$ and $15 M_{\odot}$ stars, which in contrast to ours were Newtonian and were performed with a flux-limited neutrino diffusion scheme, revealed the initiation of an explosion at the time when the inner edge of the oxygen layer accretes through the shock. The authors reported that explosions were only obtained when they used an alpha network of nuclei for following composition changes by nuclear burning in the collapsing stellar layers, but not when they applied a “flashing” treatment with instantaneous conversion of the nuclear abundances from non-NSE to NSE. They diagnosed that effective energy release by oxygen burning in the immediate vicinity of the shock, which in their case happens only with the alpha network, assists the explosion, in particular in case of a weak shock. Their papers do not provide the information that would allow us to conduct a detailed comparison of the composition evolution in their simulations and in ours. However, we emphasise that although we do not use a nuclear reaction network, we still follow composition changes in the non-NSE regime by converting oxygen to silicon and silicon to iron when the corresponding burning temperatures are reached due to compressional (or shock) heating in the infalling stellar layers. In our calculations for the $11.2 M_{\odot}$ and $15 M_{\odot}$ progenitors a variety of important indicators signal the onset of the blast and strong outward shock acceleration already long before the accretion shock has reached the inner boundary of the oxygen-rich layer. This, of course, does not mean that oxygen burning in the collapsing layers has no bearing on the possibility of an explosion, but it means that the inauguration of the blast is not correlated with oxygen combustion happening at the shock. Independent of whether a more accurate network treatment of nuclear reactions and of the transition to NSE instead of our simplified description can make a difference for

the shock propagation or not, the simulations by Bruenn et al. (2006) and Mezzacappa et al. (2007) suggest that any such improvement is likely not to disfavor explosions of the investigated stars. In this sense the fundamental agreement of the outcome of these different simulations, in spite of various differences in numerical aspects and input physics, may be considered as very encouraging.

Certainly, our current simulations can only be suggestive for how neutrino heating and hydrodynamic instabilities in collapsing stellar cores can collaborate to initiate the supernova explosion. The simulations must be continued to later times for determining the explosion properties, and definitely more calculations are needed to obtain a clear understanding how the shock revival depends on the core structure of the progenitor stars and on the physics that plays a role in the supernova core, e.g., the neutrino opacities, equation of state, rotation, the depth of the gravitational potential, and also stochastic elements like chaotic fluctuations of the SASI strength in the nonlinear regime. Also the influence of the numerical resolution has to be more closely studied. Our simulations cannot assess all the interesting questions involved. The results as presented here should only be seen as an indication that the neutrino-driven mechanism is a viable possibility for driving supernova explosions of progenitor stars significantly more massive than $10 M_{\odot}$.

The positive trend towards a SASI-supported, neutrino-driven runaway late after bounce might be linked to a (relatively) soft equation of state for neutron star matter, like the EoS of Lattimer & Swesty (1991) used by us. Our set of calculations for the considered $15 M_{\odot}$ star, although including also a model with a significantly stiffer nuclear EoS, does not provide an answer to the question how robust the success of the SASI-supported neutrino-heating mechanism is to variations of such an important physics ingredient. Systematic long-time simulations for different nuclear equations of state are needed to explore the differences at times later than covered by our present calculations. Also the exact moment when the explosion sets in can well be sensitive to various uncertain aspects like the amount of rotation in the stellar core, the possible influence of amplifying magnetic fields, unsettled details of the subnuclear equation of state and of neutrino-matter interactions, neutrino oscillations, the missing treatment of lateral neutrino fluxes in our simulations, and the approximative description of the effects of relativistic gravity. Even stochastic variations at some fairly low energy level ($\mathcal{O}(10^{49})$ erg in the gain layer) seem to be sufficient to foster an explosion at an earlier time. Simulations in full relativity are certainly desirable, in particular for stellar core collapse with rotation, because in this case the optimal choice of the effective gravitational potential is not obvious (see Marek et al. 2006). Moreover, supernova modeling in three spatial dimensions must be the ultimate goal, because the

growth rate and properties of the hydrodynamic instabilities in 3D must be expected to differ from the axially symmetric 2D case, and new degrees of freedom may play a non-negligible and potentially helpful role, for example spiral waves ($m \neq 0$ modes) and triaxial instabilities (see, e.g., Blondin & Mezzacappa 2007, Ott et al. 2007, Yamasaki & Foglizzo 2007, Iwakami et al. 2008).

In the light of our present results, supernova explosions appear to be an *accretion instability* rather than an aspherical wind as described by Burrows et al. (2007c). The SASI and convective instabilities, and in particular the simultaneous presence of accretion and outflow of neutrino-heated gas, which drives the shock expansion, are crucial ingredients of the explosions described in this paper and constitute the explosions as a generically multi-dimensional phenomenon. The gas outflow during the main phase of shock revival and the build-up of the explosion energy are fed by neutrino-heated, accreted gas. Only much later, after the accretion has ceased, does the gain radius retreat to the neutron star surface and the cooling layer between neutrinosphere and gain radius shrinks to a very narrow region or disappears completely. This marks the onset of the neutrino-driven baryonic wind phase, in which the dilute gas outflow from the nascent neutron star is determined solely by the conditions at the surface of the hot, compact remnant and not by the (accretion) properties of the dying star.

We are very grateful to R. Buras, K. Kifonidis, B. Müller, E. Müller, and M. Rampp for their input to various aspects of the reported project, to R. Johanni for his support in parallelizing our code, and to S. Woosley for data of his progenitor model. We thank A. Burrows, C.D. Ott, and an anonymous referee for their numerous suggestions of how to improve our manuscript and to extend our investigations. This work was supported by the Deutsche Forschungsgemeinschaft through the Transregional Collaborative Research Centers SFB/TR 27 “Neutrinos and Beyond” and SFB/TR 7 “Gravitational Wave Astronomy”, the Collaborative Research Center SFB-375 “Astro-Particle Physics”, and the Cluster of Excellence EXC 153 “Origin and Structure of the Universe” (<http://www.universe-cluster.de>). The computations were performed on the IBM p690 of the John von Neumann Institute for Computing (NIC) in Jülich, on the national supercomputer NEC SX-8 at the High Performance Computing Center Stuttgart (HLRS) under grant number SuperN/12758, on the IBM p690 of the Computer Center Garching (RZG), on the sgi Altix 4700 of the Leibniz-Rechenzentrum (LRZ) in Munich, and on the sgi Altix 3700 of the MPI for Astrophysics. We also acknowledge support by AstroGrid-D, a project funded by the German Federal Ministry of Education and Research (BMBF) as part of the D-Grid initiative.

REFERENCES

- Bethe, H.A. & Wilson, J.R. 1985, ApJ, 295, 14
 Blondin, J.M. & Mezzacappa, A. 2006, ApJ, 642, 401
 Blondin, J.M. & Shaw, S. 2007, ApJ, 656, 366
 Blondin, J.M. & Mezzacappa, A. 2007, Nature, 445, 58
 Blondin, J. M., Mezzacappa, A., & DeMarino, C. 2003, ApJ, 584, 971
 Bruenn, S. W. & Dineva, T. 1996, ApJ, 458, L71
 Bruenn, S.W., Dirk, C.J., Mezzacappa, A., Hayes, J.C., Blondin, J.M., Hix, W.R., & Messer, O.E.B. 2006, in: SciDAC 2006, Scientific Discovery through Advanced Computing, Denver, Colorado, USA, 25–29 June 2006, Eds. W.M. Tang, et al., Journ. Phys. Conf. Ser., 46, p. 393; arXiv0709.0537 (astro-ph)
 Buras, R., Rampp, M., Janka, H.-T., & Kifonidis, K. 2003a, Phys. Rev. Lett., 90, 241101

- Buras, R., Janka, H.-Th., Keil, M.Th., Raffelt, G., & Rampp, M. 2003b, *ApJ*, 587, 320
- Buras, R., Rampp, M., Janka, H.-T., & Kifonidis, K. 2006a, *A&A*, 447, 1049
- Buras, R., Janka, H.-T., Rampp, M., & Kifonidis, K. 2006b, *A&A*, 457, 281
- Burrows, A. & Goshy, J. 1993, *ApJ*, 416, L75
- Burrows, A., Hayes, J., & Fryxell, B.A. 1995, *ApJ*, 450, 830
- Burrows, A., Livne, E., Dessart, L., Ott, C.D., & Murphy, J. 2006, *ApJ*, 640, 878
- Burrows, A., Dessart, L., Livne, E., Ott, C.D., & Murphy, J. 2007a, *ApJ*, 664, 416
- Burrows, A., Livne, E., Dessart, L., Ott, C.D., & Murphy, J. 2007b, *ApJ*, 655, 416
- Burrows, A., Dessart, L., Ott, C.D., & Livne, E. 2007c, *Phys. Rep.*, 442, 23
- Colgate, S.A. & White, R.H. 1966, *ApJ*, 143, 626
- Dessart, L., Burrows, A., Livne, E., & Ott, C.D. 2006, *ApJ*, 645, 534
- Foglizzo, T., 2001, *A&A*, 368, 311
- Foglizzo, T., 2002, *A&A*, 392, 353
- Foglizzo, T., 2008, *ApJ*, submitted; arXiv:0809.2302 (astro-ph)
- Foglizzo, T., Scheck, L., & Janka H.-Th. 2006, *ApJ*, 652, 1436
- Foglizzo, T., Galletti, P., Scheck, L., & Janka H.-Th. 2007, *ApJ*, 654, 1006
- Fryer, C.L. 1999, *ApJ*, 522, 413
- Fryer, C.L. & Warren, M.S. 2002, *ApJ*, 574, L65
- Fryer, C.L. & Warren, M.S. 2004, *ApJ*, 601, 391
- Heger, A., Woosley, S.E., & Spruit H.C. 2005, *ApJ*, 626, 350
- Herant, M., Benz, W., Hix, W.R., Fryer, C.L., & Colgate, S.A. 1994, *ApJ*, 435, 339
- Hillebrandt, W. 1994, in *Supernovae*, ed. S.A. Bludman, R. Mochkovitch, & J. Zinn-Justin (Amsterdam: North-Holland), 251
- Hillebrandt, W. & Wolff, R.G. 1985, in *Nucleosynthesis: Challenges and New Developments*, ed. W.D. Arnett & J.W. Truran (Chicago: Univ. Chicago Press), 131
- Hillebrandt, W., Nomoto, K., & Wolff, R.G. 1984, *A&A*133, 175
- Iwakami, W., Kotake, K., Ohnishi, N., Yamada, S., & Sawada, K. 2008, *ApJ*, 678, 1207
- Janka, H.-T. 2001, *A&A*, 368, 527
- Janka, H.-T. & Mönchmeyer, R. 1989a, *A&A*, 209, L5
- Janka, H.-T. & Mönchmeyer, R. 1989b, *A&A*, 226, 69
- Janka, H.-T. & Müller, E. 1996, *A&A*, 306, 167
- Janka, H.-T., Kifonidis, K., & Rampp, M. 2001, in *Physics of Neutron Star Interiors*, ed. D. Blaschke, N.K. Glendenning, & A. Sedrakian, *Notes in Physics*, Vol. 578 (Berlin: Springer), 333; astro-ph/0103015
- Janka, H.-T., Marek, M., & Kitaura, F.-S. 2007, in: *Supernova 1987A: 20 Years After: Supernovae and Gamma-Ray Bursters*. AIP Conference Proceedings, Vol. 937, p. 144 (2007); arXiv:0706.3056 (astro-ph)
- Janka, H.-Th., Langanke, K., Marek, A., Martínez-Pinedo, G., & Müller B. 2007, *Phys. Rep.*, 442, 38
- Janka, H.-Th., Müller, B., Kitaura, F.S., & Buras, R. 2008, *A&A*, 485, 199
- Keil, M.Th., Raffelt, G., & Janka, H.-Th. 2003, *ApJ*, 590, 971
- Kifonidis, K., Plewa, T., Scheck, L., Janka, H.-Th., & Müller, E. 2006, *A&A*, 453, 661
- Kitaura, F. S., Janka, H.-T., & Hillebrandt, W. 2006, *A&A*, 450, 345
- Köhler, H.S. 1975, *Nucl. Phys.* A258, 301
- Langanke, K., Martínez-Pinedo, G., Sampaio, J.M., Dean, D.J., Hix, W.R., Messer, O.E.B., Mezzacappa, A., Liebendörfer, M., Janka, H.-Th., & Rampp, M. 2003, *Phys. Rev. Lett.*, 90, 241102
- Lattimer, J.M. & Swesty, F.D. 1991, *Nucl. Phys.* A535, 331
- Lattimer, J.M. & Prakash, M. 2007, *Phys. Rep.*, 442, 109
- Lattimer, J.M., Pethick, C.J., Ravenhall, D.G., & Lamb, D.Q. 1985, *Nucl. Phys.*, A432, 646
- Liebendörfer, M., Rampp, M., Janka, H.-Th., & Mezzacappa, A. 2005, *ApJ*, 620, 840
- Marek, A. 2007, PhD Thesis, TU München
- Marek, A., Janka, H.-Th., & Müller, E. 2008, *A&A*, submitted; arXiv:0808.4136 (astro-ph)
- Marek, A., Janka, H.-Th., Buras, R., Liebendörfer, M., & Rampp, M. 2005, *A&A*, 443, 201
- Marek, A., Dimmelmeier, H., Janka, H.-Th., Müller, E., & Buras, R. 2006, *A&A*, 445, 273
- Mayle, R. & Wilson, J.R. 1988, *ApJ*, 334, 909
- Mezzacappa, A., Bruenn, S.W., Blondin, J.M., Hix, W.R., & Messer, O.E.B. 2007, in: *The Multicolored Landscape of Compact Objects and Their Explosive Origins*. AIP Conference Proceedings, Vol. 924, p. 234 (2007); arXiv:0709.1484 (astro-ph)
- Müller, E. & Steinmetz, M. 1995, *Computer Phys. Commun.*, 89, 45
- Müller, E., Rampp, M., Buras, R., Janka, H.-Th., & Shoemaker, D.H. 2004, *ApJ*, 603, 221
- Murphy, J.W. & Burrows, A. 2008, *ApJ*, in press; arXiv:0805.3345 (astro-ph)
- Nomoto, K. 1984, *ApJ*, 277, 791
- Nomoto, K. 1987, *ApJ*, 322, 206
- Ohnishi, N., Kotake, K., & Yamada, S. 2006, *ApJ*, 641, 1018
- Ott, C.D., Dimmelmeier, H., Marek, A., Janka, H.-Th., Hawke, I., Zink, B., & Schnetter, E. 2007, *Phys. Rev. Lett.*, 98, 261101
- Qian, Y.-Z., & Woosley, S.E. 1996, *ApJ*, 471, 331
- Raffelt, G.G. 2001, *ApJ*, 561, 890
- Rampp, M., Janka, H.-Th. 2002, *A&A*, 396, 361
- Scheck, L., Kifonidis, K., Janka, H.-Th., & Müller, E. 2006, *A&A*, 457, 963
- Scheck, L., Janka, H.-Th., Foglizzo, T., & Kifonidis, K. 2008, *A&A*, 477, 931
- Shen, H., Toki, H., Oyamatsu, K., & Sumiyoshi K. 1998, *Nucl. Phys.*, A637, 435
- Thompson, T.A., Burrows, A., & Meyer, B.S. 2001, *ApJ*, 562, 887
- Thompson, T. A., Quataert, E., & Burrows, A. 2005, *ApJ*, 620, 861
- Weinberg, N.N. & Quataert, E. 2008, *MNRAS*, 387, L64
- Wilson, J.R. 1985, in *Numerical Astrophysics*, ed. J.M. Centrella, J.M. LeBlanc, & R.L. Bowers (Boston: Jones and Bartlett Publ.), 422
- Wilson, J.R. & Mayle, R. 1988, *Phys. Rep.*, 163, 63
- Wilson, J.R. & Mayle, R. 1993, *Phys. Rep.*, 227, 97
- Woosley, S. E. & Weaver, T. A. 1995, *ApJS*, 101, 181
- Woosley, S. E., Heger, A., & Weaver, T. A. 2002, *Reviews of Modern Physics*, 74, 1015
- Yamasaki, T. & Yamada, S. 2005, *ApJ*, 623, 1000
- Yamasaki, T. & Yamada, S. 2007, *ApJ*, 656, 1019
- Yamasaki, T. & Foglizzo, T. 2008, *ApJ*, 679, 607
- Yoshida, S., Ohnishi, N., & Yamada, S. 2007, *ApJ*, 665, 1268

TABLE 1. INVESTIGATED $15 M_{\odot}$ MODELS.

Model	Dimension	N_r ^a	N_{θ} ^b	N_{ϵ} ^c	Φ_{eff} ^d
M15LS-1D	1D	600–960	1	17	new
M15HW-1D	1D	600–750	1	17	new
M15LS-rot	2D & rotation	400–850	128	17	old
M15LS-2D	2D	600–960	192	17	new
M15HW-2D	2D	600–700	192	17	new
M15LS-rot9	2D & rotation	400–500	128	9	new

^aNumber of radial grid points, increasing with time.

^bNumber of lateral grid points from pole to pole.

^cNumber of energy grid points for the neutrino transport.

^dEffective relativistic potential; “old” corresponds to definition introduced by Rampp & Janka (2002), which is equivalent to Case R of Marek et al. (2006); “new” corresponds to Case A of Marek et al. (2006).

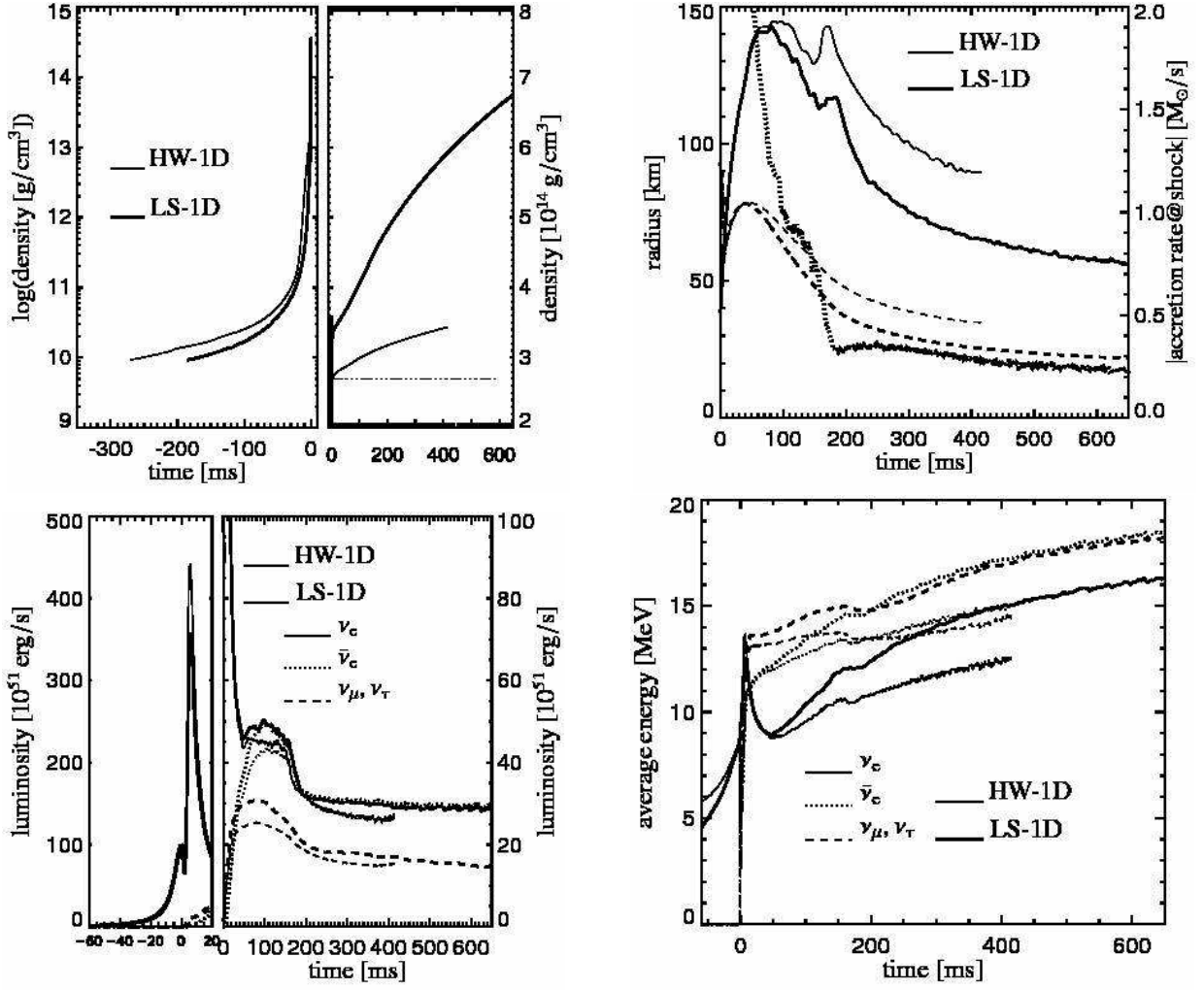


FIG. 1.— Results of our two 1D models, M15LS-1D (bold lines) and M15HW-1D. Time is normalized to the moment of core bounce. *Top left:* Central densities as functions of time. The horizontal dash-triple-dotted line marks the value of the nuclear saturation density, $\rho_0 \approx 2.7 \times 10^{14} \text{ g cm}^{-3}$. *Top right:* Radii of shock (solid lines) and electron neutrinosphere (dashed lines) as functions of time. The transient shock expansion around 170 ms after bounce is caused by a composition interface with sudden decrease of the mass accretion rate arriving at the shock. The mass accretion rate is displayed by the bold dotted line. *Bottom left:* Luminosities of electron neutrinos, electron antineutrinos, and muon or tau neutrinos (or their antiparticles) as functions of time. *Bottom right:* Mean energies of radiated neutrinos (computed as the ratio of energy to number flux) for electron neutrinos, electron antineutrinos, and heavy-lepton neutrinos and antineutrinos. The luminosities and mean energies are shown as measured by an observer at rest relative to the stellar center at 400 km (from where the gravitational redshift to infinity is negligibly small). The softer LS-EoS leads to a much larger central density, a significantly more compact neutron star and therefore considerably higher luminosities and mean energies of the radiated neutrinos.

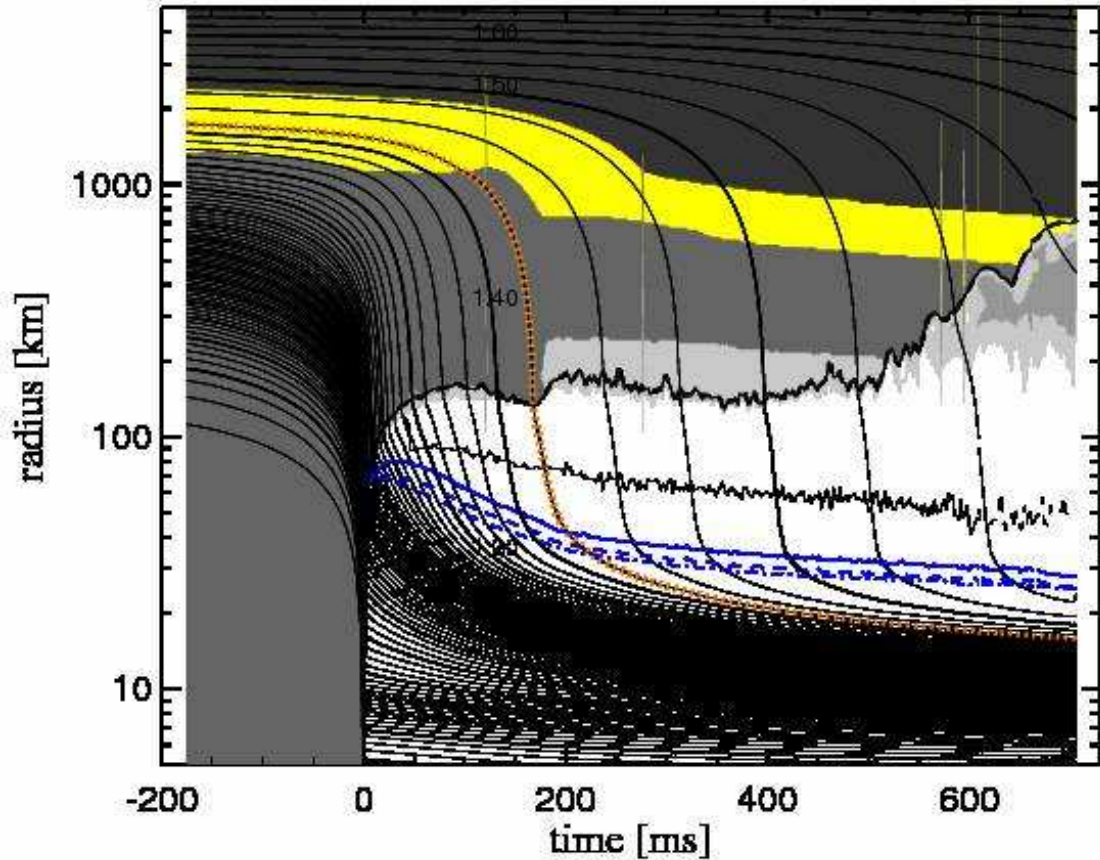


FIG. 2.— Time evolution of Model M15LS-rot visualized by mass shell trajectories. In this 2D simulation with rotation, the mass-shell lines mark the radii of spheres that contain certain values of the rest mass (the plot is based on an evaluation of the mass-weighted lateral average of the 2D data set). They are spaced in steps of $0.025 M_{\odot}$ with bold lines every $0.1 M_{\odot}$. The thick solid line starting at $t = 0$ denotes the mass-averaged shock position, the blue lines represent the mean neutrinospheres of ν_e (solid), $\bar{\nu}_e$ (dashed), and heavy-lepton neutrinos (dash-dotted), the black dashed curve shows the mean gain radius, and the location of the composition interface between the silicon shell and the oxygen-enriched Si-layer of the progenitor star at $1.42 M_{\odot}$ is highlighted by a red dashed line. Different shadings indicate regions with different chemical composition. Dark grey marks the layer where the mass fraction of oxygen is larger than 10% (which corresponds to the inner boundary of the layers that contain significant amounts of oxygen), medium grey the region where the mass fraction of heavy nuclei with mass numbers $A \geq 56$ exceeds 70%, the yellow band in between is the layer where both abundance constraints are not fulfilled (in this region silicon and sulfur are abundant), light grey indicates those regions where more than 30% of the mass is in α -particles, and the white areas enclosed by the shock front contain mostly free nucleons and only a small mass fraction (less than 30%) of α -particles. At times $t \gtrsim 600$ ms post bounce, slightly darker grey patches in the light-grey postshock regions contain a mass fraction of more than 60% helium nuclei. This signals that the nucleon recombination becomes more complete and/or that the dissociation of alpha particles to free nucleons is less complete in the matter expanding behind the outgoing shock because of low postshock temperatures when the shock reaches larger radii. Note that compressional heating triggers nuclear burning (described in our simulations by a “flashing treatment”, see Sect. 2.1) and leads to changes of the chemical composition in the infalling stellar layers.

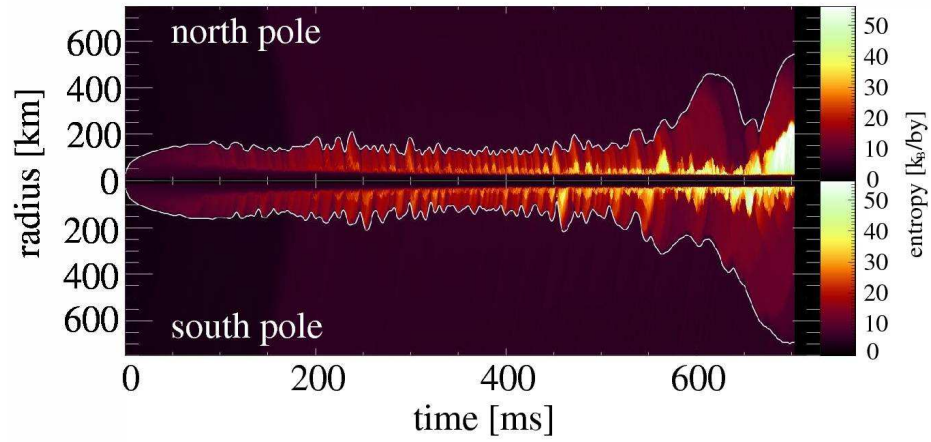


FIG. 3.— Radial positions of the shock near the north and south poles of Model M15LS-rot as functions of post-bounce time (white lines). The color coding represents the entropy per nucleon of the stellar gas. The quasi-periodic, bi-polar shock expansion and contraction due to the SASI can be clearly seen.

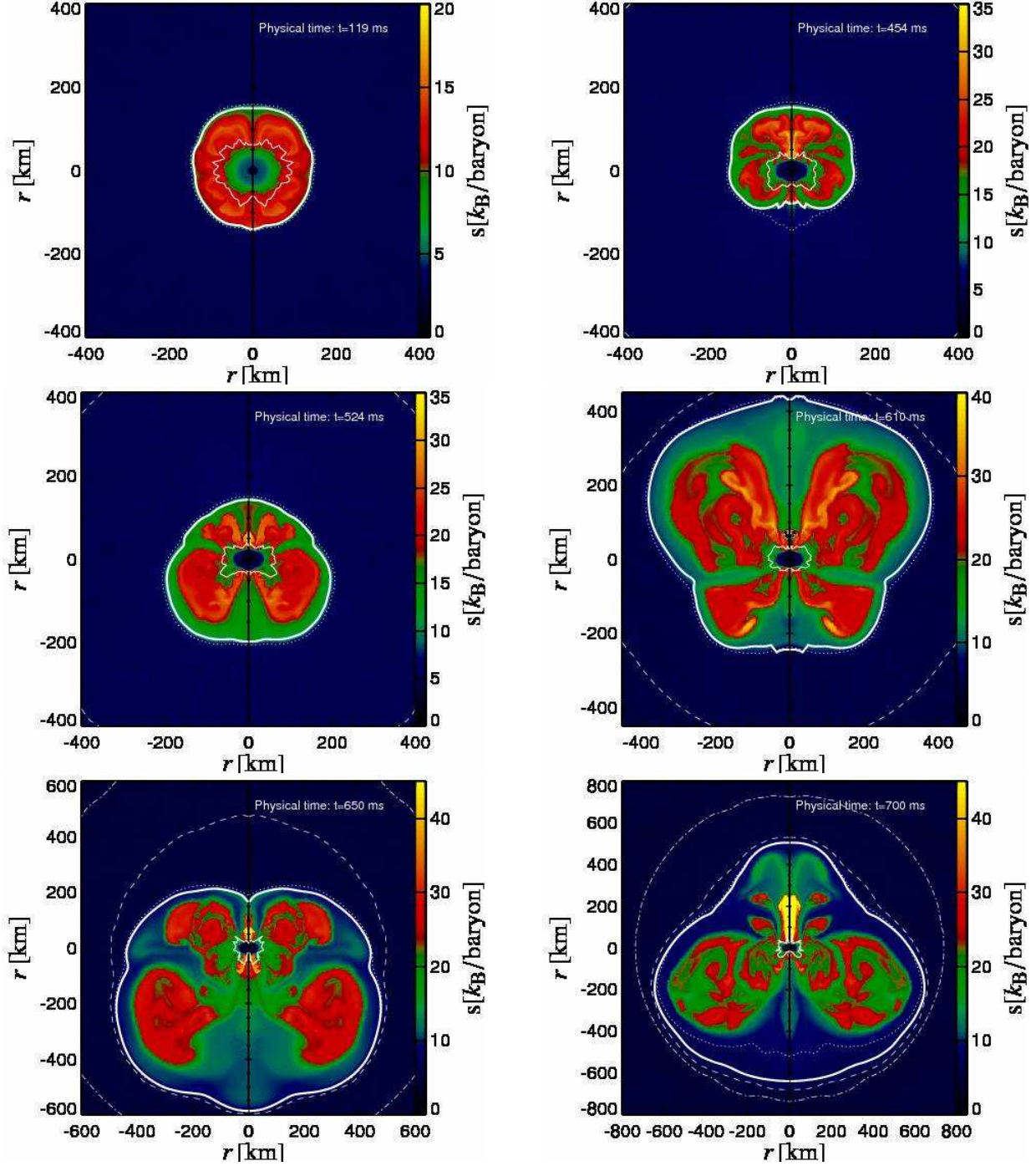


FIG. 4.— Six snapshots from the post-bounce evolution of Model M15LS-rot. The color coding represents the entropy of the stellar gas. The shock is visible as deformed sharp discontinuity between low-entropy, infalling matter in the upstream region and high-entropy, boiling matter behind the shock; its position is highlighted by a bold, solid white contour. The top left plot shows the entropy distribution at $t = 119$ ms after bounce, about 40 ms after the postshock convection has reached the nonlinear regime and the shock develops first small nonsphericities. The top right and middle left plots ($t = 454$ ms and 524 ms after bounce, respectively) demonstrate the presence of very strong bipolar oscillations due to the SASI, the middle right plot ($t = 610$ ms p.b.) displays the beginning of a rapid outward expansion, and the lower two plots (for $t = 650$ ms and 700 ms post bounce) show the onset of the explosion with a largely aspherical shock that possesses a dominant $l = 1$ deformation mode. Note that the radial scale was adjusted in the last three snapshots and that the contracting nascent neutron star exhibits a growing prolate deformation because of the rotation considered in this simulation. The thin, solid white line in each panel marks the direction-dependent location of the gain radius, and the thin dotted, dashed, and dash-dotted white lines indicate the inner boundaries of the regions where iron-group elements, silicon, or oxygen, respectively, dominate the composition (the contours are defined by mass fractions of 30% iron-group elements, 30% silicon, and 10% oxygen, respectively). In some of the panels not all these composition interfaces are located within the plotted area, and the iron-dissociation line or the iron-silicon interface can (at least partly) overlap with the shock contour. We point out that the rotation of the model is so slow that the composition interfaces in the preshock region exhibit no visible centrifugal deformation.

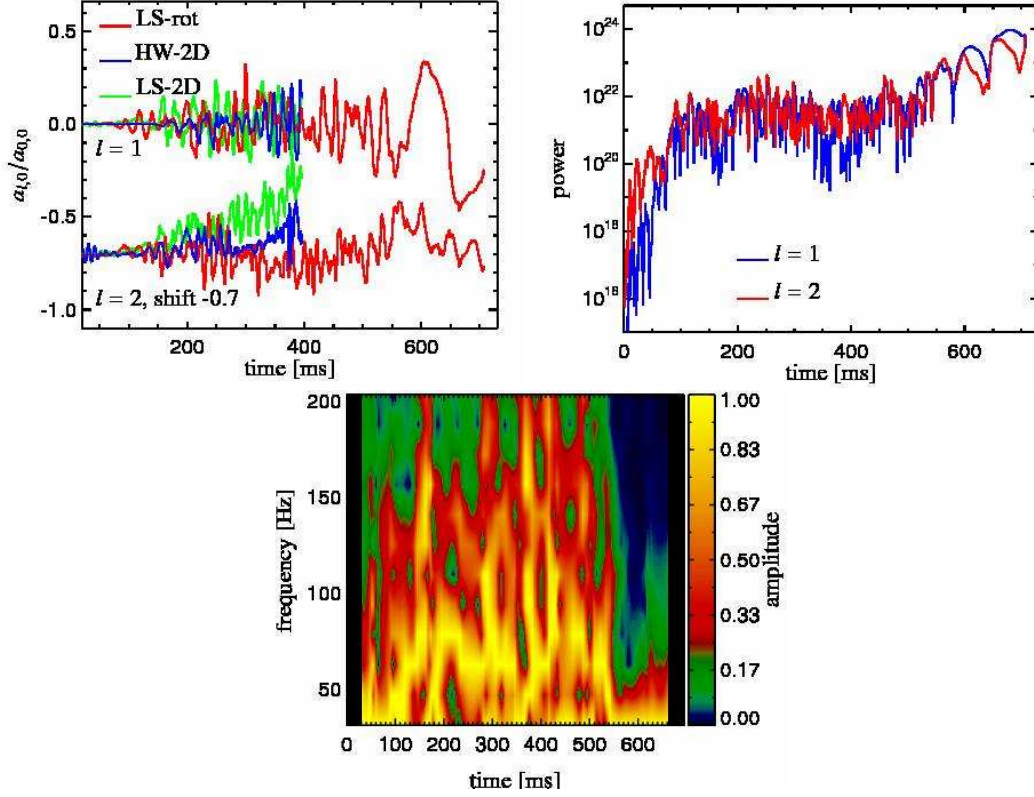


FIG. 5.— SASI and convective activity in Model M15LS-rot versus post-bounce time. *Top*: Coefficients of the dipole ($l = 1$) and quadrupole ($l = 2$) modes of the spherical harmonics expansion of the angle-dependent shock position, normalized to the amplitude of the $l = 0$ mode. For better visibility the curve of the $l = 2$ mode is shifted downward by 0.7 units. The results for Models M15LS-2D and M15HW-2D are also shown for comparison. *Middle*: Power of the $l = 1$ and $l = 2$ modes of the spherical harmonics expansion of the fractional pressure variations $[P(r, \theta) - \langle P(r, \theta) \rangle_\theta] / \langle P \rangle_\theta$, integrated over the volume between average electron neutrinosphere and average shock radius. *Bottom*: Frequency spectrum versus time of the combined power in $l = 1$ and $l = 2$ modes shown in the middle panel. The fourier analysis was performed every two milliseconds, sampling information in time windows of 64 ms width (which leads to discrete frequencies of 15.6 Hz and multiples), and the spectra were normalized on each time slice.

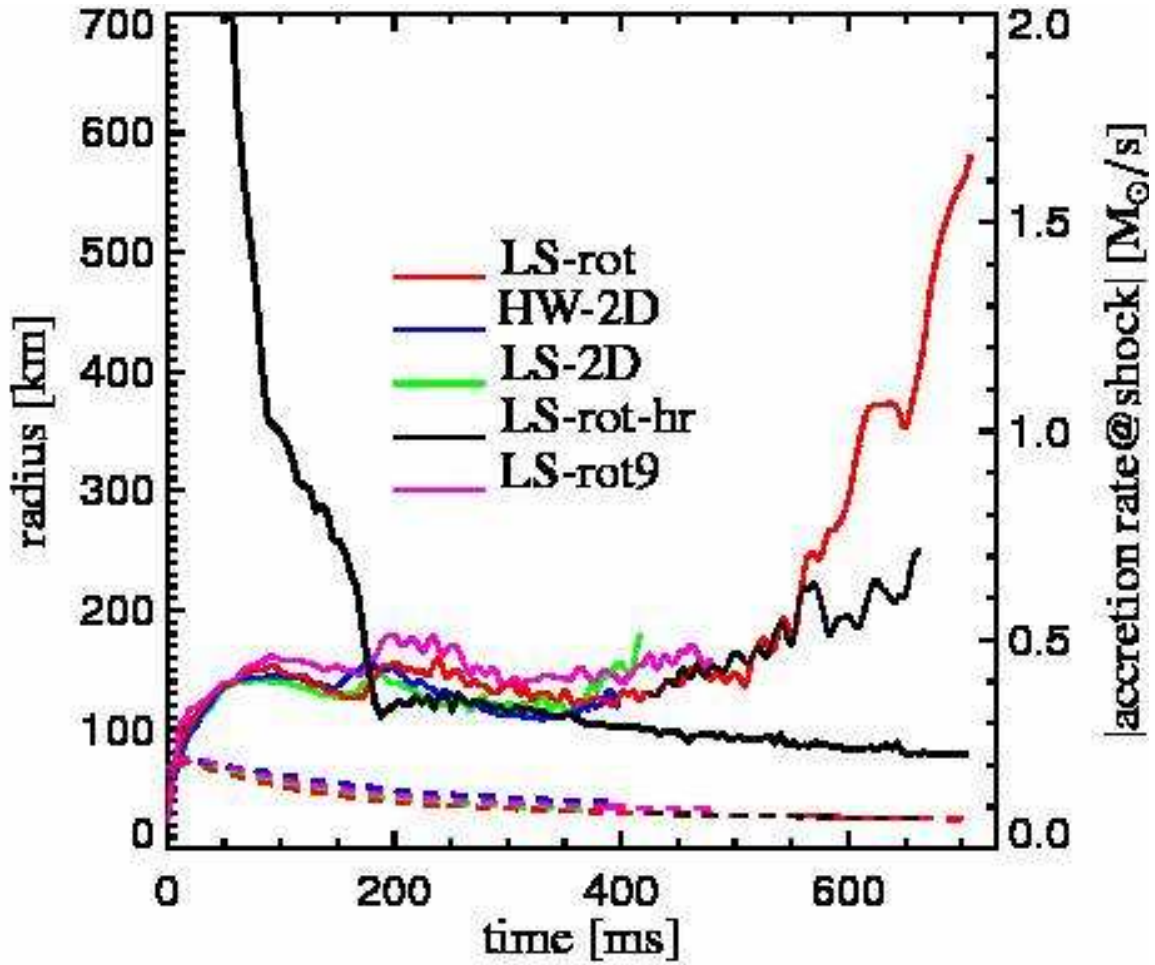


FIG. 6.— Average shock radii (solid) and average neutron star radii (dashed) for the set of computed 2D models with the $15 M_{\odot}$ progenitor as functions of post-bounce time (left vertical scale of the figure). The shock position is defined as the arithmetical average over all directions, and the mean radius of the (in case of rotation, deformed) neutron star is determined as the arithmetical mean of all radial positions where the density equals $10^{11} \text{ g cm}^{-3}$. The bold black curve shows the time-dependent mass accretion rate just ahead of the shock in Model M15LS-rot (scale on the right vertical axis of the plot). The additional black line between 420 and about 670 ms corresponds to Model M15LS-rot-hr, which is a test calculation of Model M15LS-rot with significantly increased radial resolution in the neutron star surface and neutrino-heating layer.

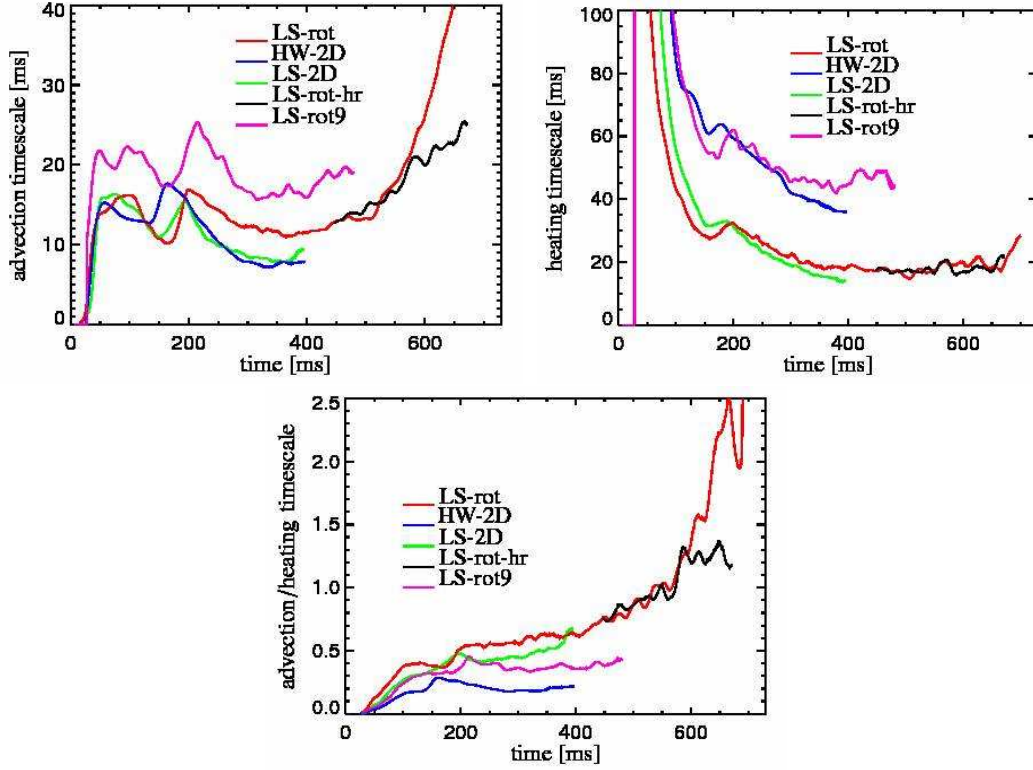


FIG. 7.— Dynamically important timescales for the set of computed 2D models with the $15 M_{\odot}$ progenitor as functions of post-bounce time. *Top:* Mean timescale for advection of accreted matter from the shock to the gain radius. *Middle:* Neutrino-heating timescale of matter in the gain layer. *Bottom:* Ratio of advection to heating timescale. The additional black line between 420 and about 670 ms corresponds to Model M15LS-rot-hr, which is a test calculation of Model M15LS-rot with significantly increased radial resolution in the neutron star surface and neutrino-heating layer. Note that towards the end of our explosion simulation (Model M15LS-rot) the advection timescale and the timescale ratio increase steeply because a dominant fraction of the mass in the gain layer begins to expand outward behind the shock instead of falling towards the gain radius (this is also reflected by a steep growth of the mass in the gain layer, see Fig. 8).

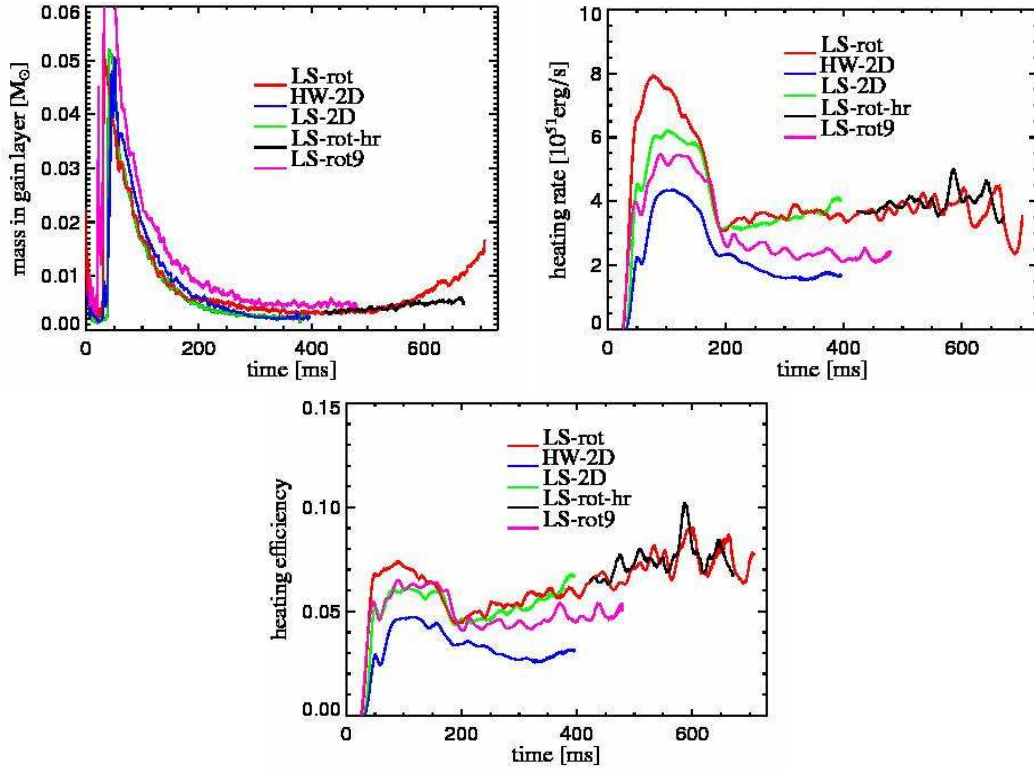


FIG. 8.— Neutrino heating conditions in the gain layer for the set of computed 2D models with the $15 M_{\odot}$ progenitor. Mass (*top*), total net rate of neutrino heating (*middle*), and neutrino heating efficiency (*bottom*) as functions of post-bounce time. The net rate of neutrino heating is defined as the difference of the neutrino energy deposition rate in the gain layer and the energy loss rate by the reemission of neutrinos. The heating efficiency is computed as the ratio of the total net heating rate to the sum of ν_e and $\bar{\nu}_e$ luminosities as seen in the observer frame. The additional black line between 420 and about 670 ms corresponds to Model M15LS-rot-hr, which is a test calculation of Model M15LS-rot with significantly increased radial resolution in the neutron star surface and neutrino-heating layer.

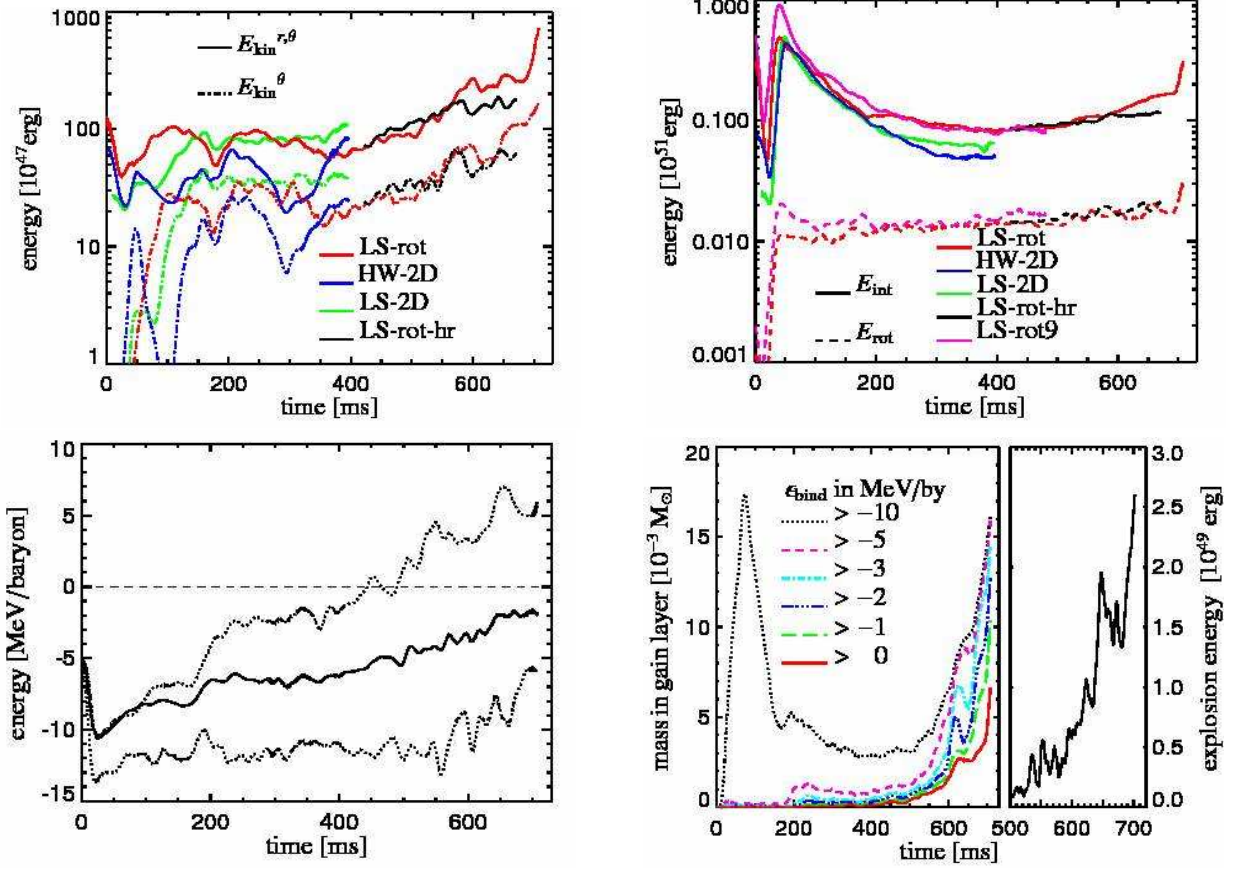


FIG. 9.— Evolution of energies in the $15 M_{\odot}$ models. The upper plots display integrated energies in the gain layer as functions of post-bounce time for several models of our set of 2D simulations, the lower plots show energies per nucleon and corresponding masses in the gain layer as functions of time for Model M15LS-rot. *Top left:* Kinetic energies $E_{\text{kin}}^{r,\theta}$ and E_{kin}^{θ} associated with the gas motion in radial and in radial plus lateral direction, respectively. *Top right:* Internal energy and rotational energy. *Bottom left:* Mean total (kinetic, including rotational, plus internal plus gravitational) energy per baryon (thick line) and energy range that contains 90% of the mass in the gain layer of Model M15LS-rot (dotted). *Bottom right:* Masses in the gain layer of Model M15LS-rot with total energies per nucleon above certain values (left panel) and increase of the “explosion energy” of the model, defined as total energy of all matter in the gain layer with positive radial velocity (right panel). In the upper two plots, the additional black line between 420 and about 670 ms corresponds to Model M15LS-rot-hr, which is a test calculation of Model M15LS-rot with significantly increased radial resolution in the neutron star surface and neutrino-heating layer. The rise of the curves for Model M15LS-rot towards the end of the simulation is a signal of the beginning explosion, which is also accompanied by a steep increase of the mass in the gain layer (see Fig. 8).

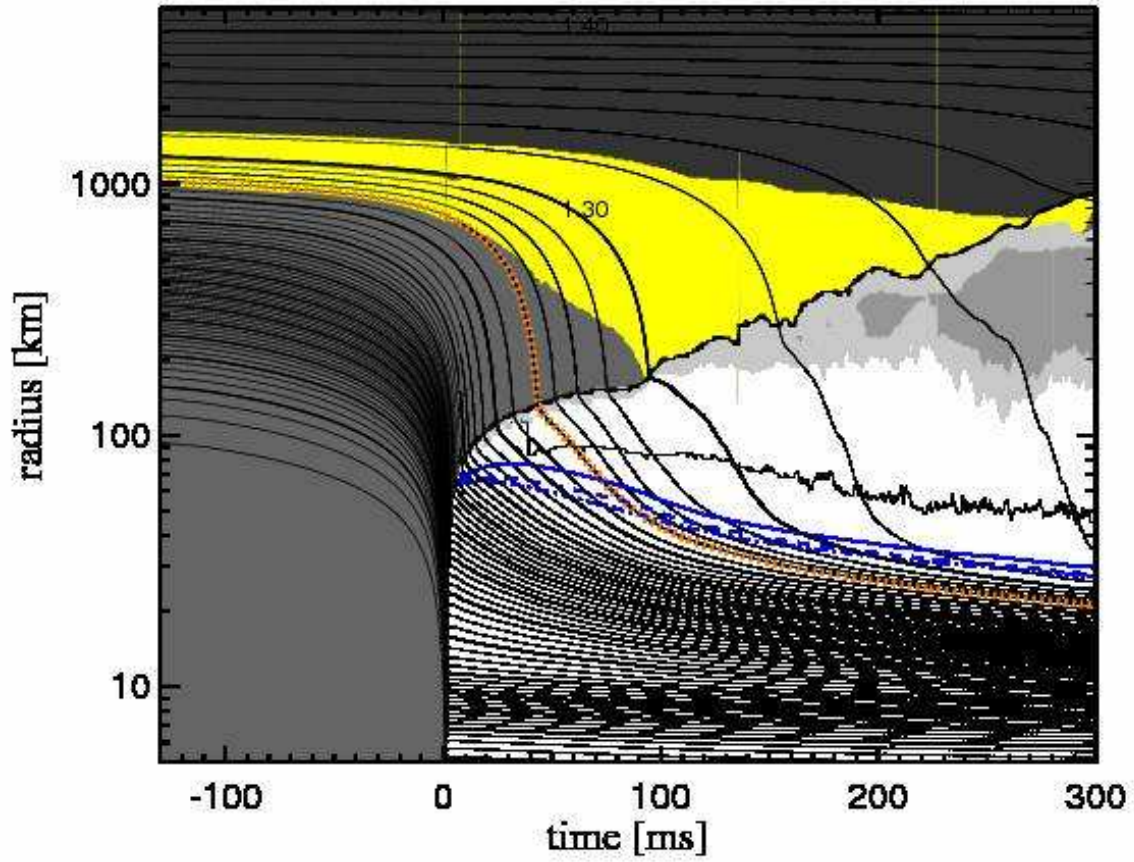


FIG. 10.— Same as Fig. 2 but for our 2D explosion simulation of an $11.2 M_{\odot}$ progenitor star. Note that the mass-shell spacing outside of the red dashed line at an enclosed mass of $1.25 M_{\odot}$ (marking the composition interface between the silicon layer and the oxygen-enriched Si-shell) is reduced to steps of $0.0125 M_{\odot}$ instead of $0.025 M_{\odot}$.

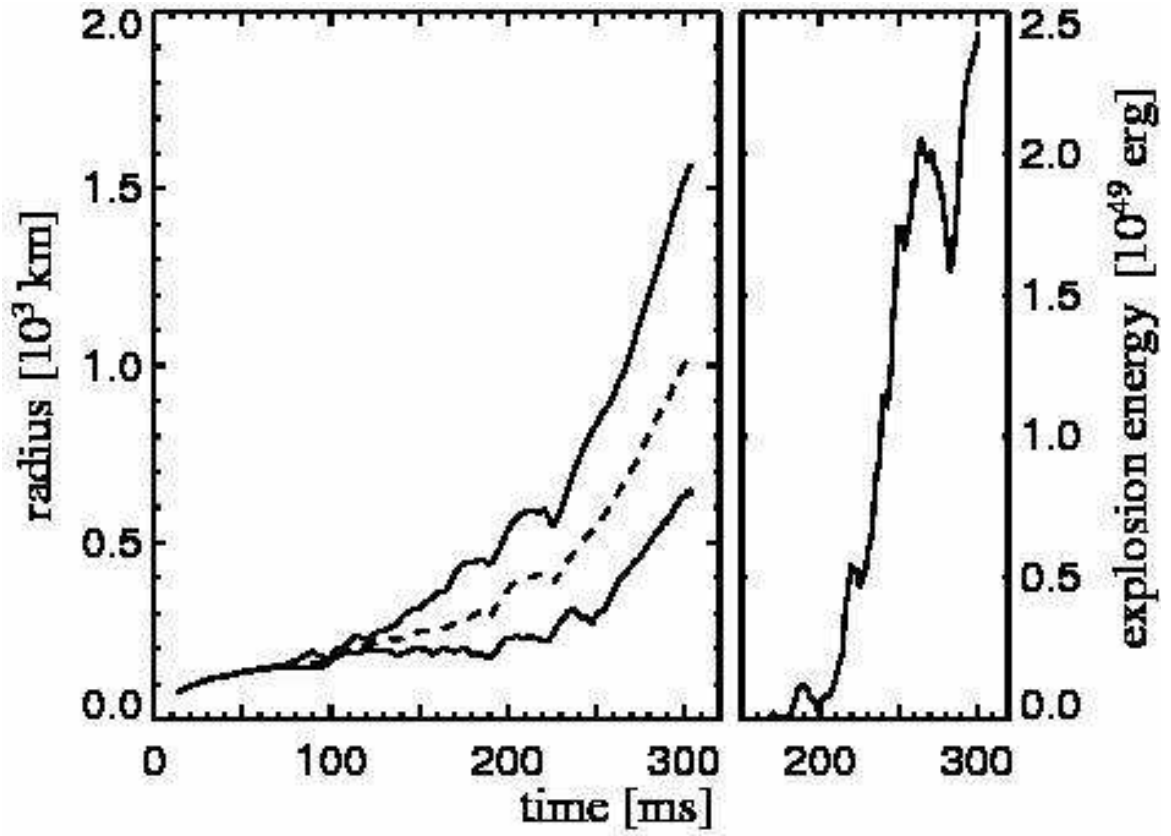


FIG. 11.— *Left panel:* Mean shock radius (arithmetical average over all lateral directions, dashed line) and maximum and minimum shock positions as functions of post-bounce time for our 2D explosion simulation of an $11.2 M_{\odot}$ progenitor. *Right panel:* “Explosion energy” of the $11.2 M_{\odot}$ star, defined as the total energy (internal plus kinetic plus gravitational) of all mass in the gain layer with positive radial velocity, as function of post-bounce time.

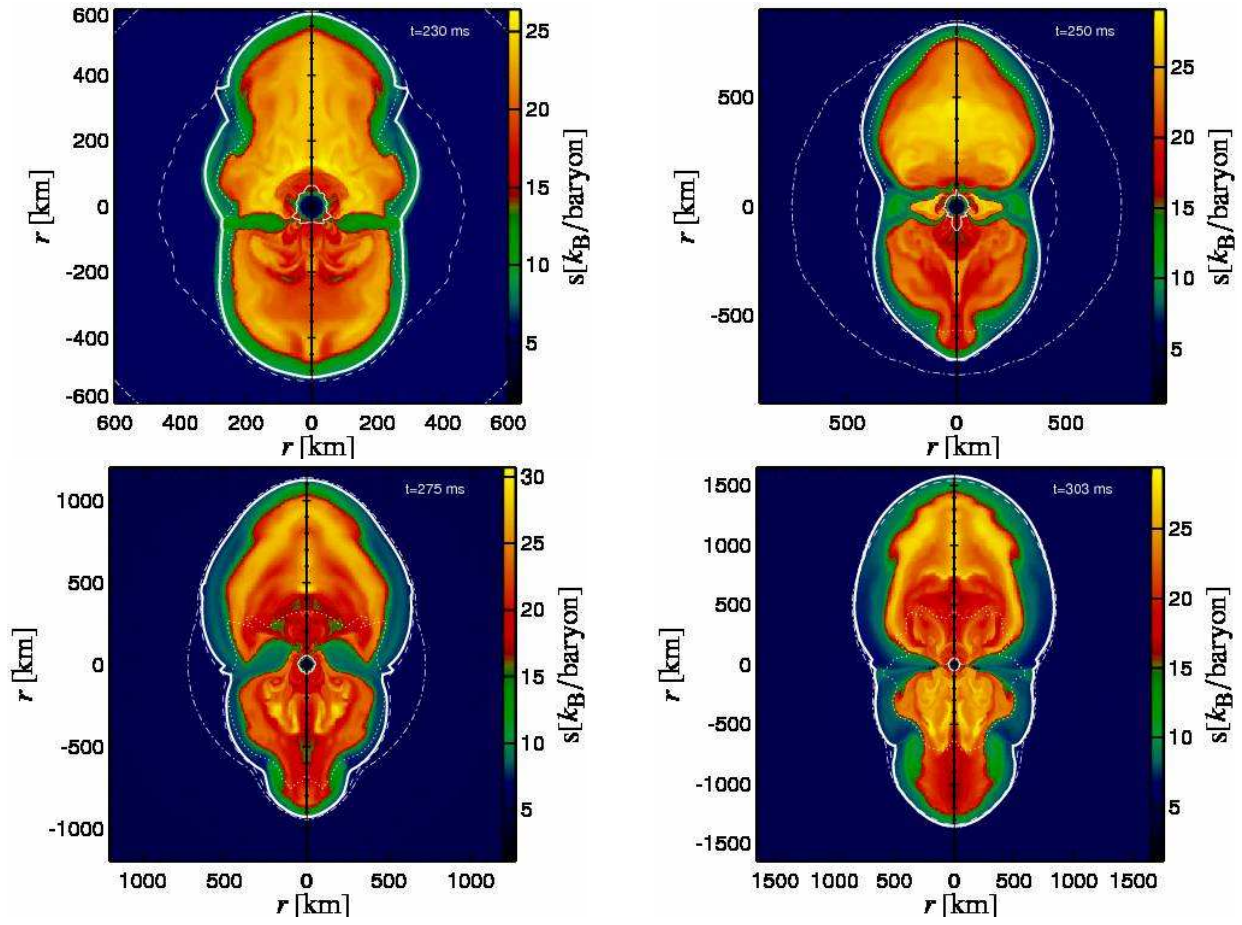


FIG. 12.— Four snapshots from the evolution of our $11.2 M_{\odot}$ explosion model at times $t = 230$ ms, 250 ms, 275 ms, and 303 ms after core bounce. The figures contain the same features as shown in Fig. 4.

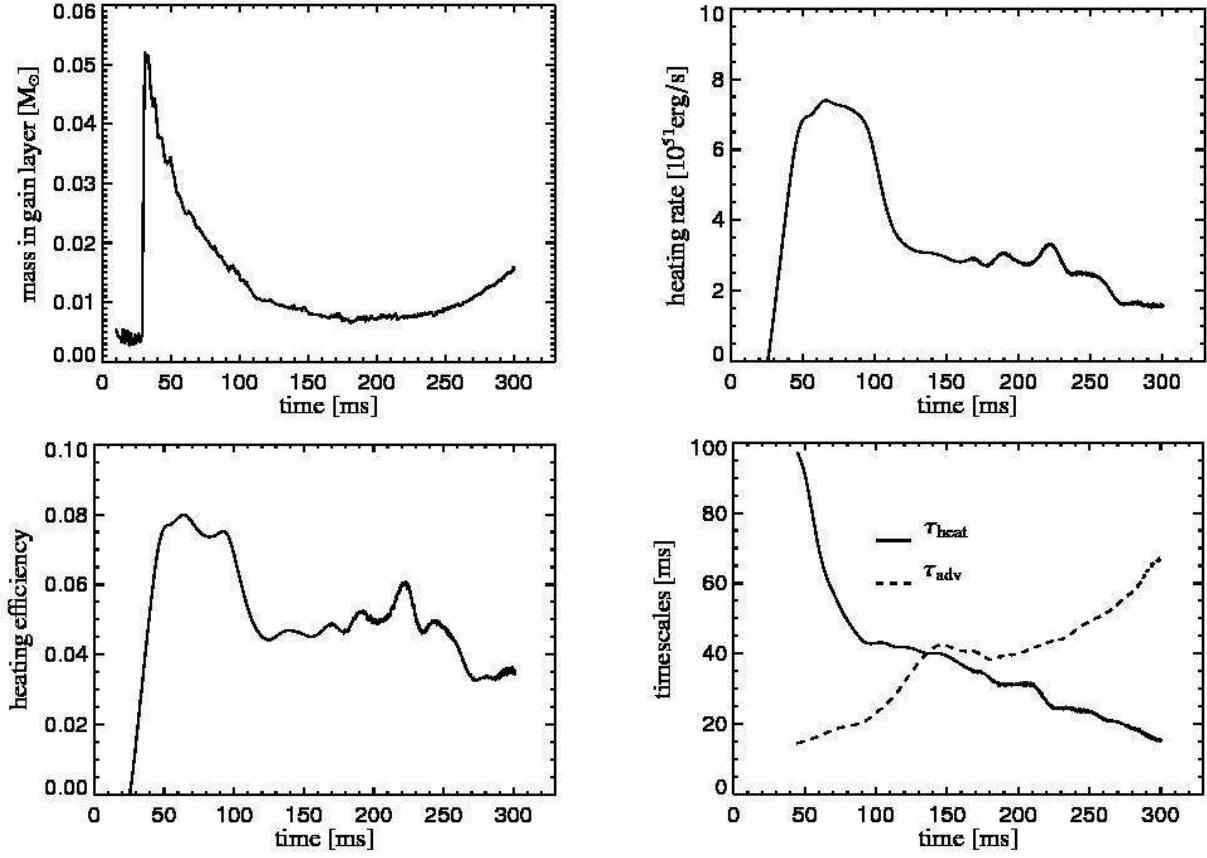


FIG. 13.— Mass (*top left*), neutrino-heating rate (*top right*), heating efficiency (*bottom left*), and heating and advection timescales (*bottom right*) in the gain layer as functions of time for our $11.2 M_{\odot}$ explosion model.

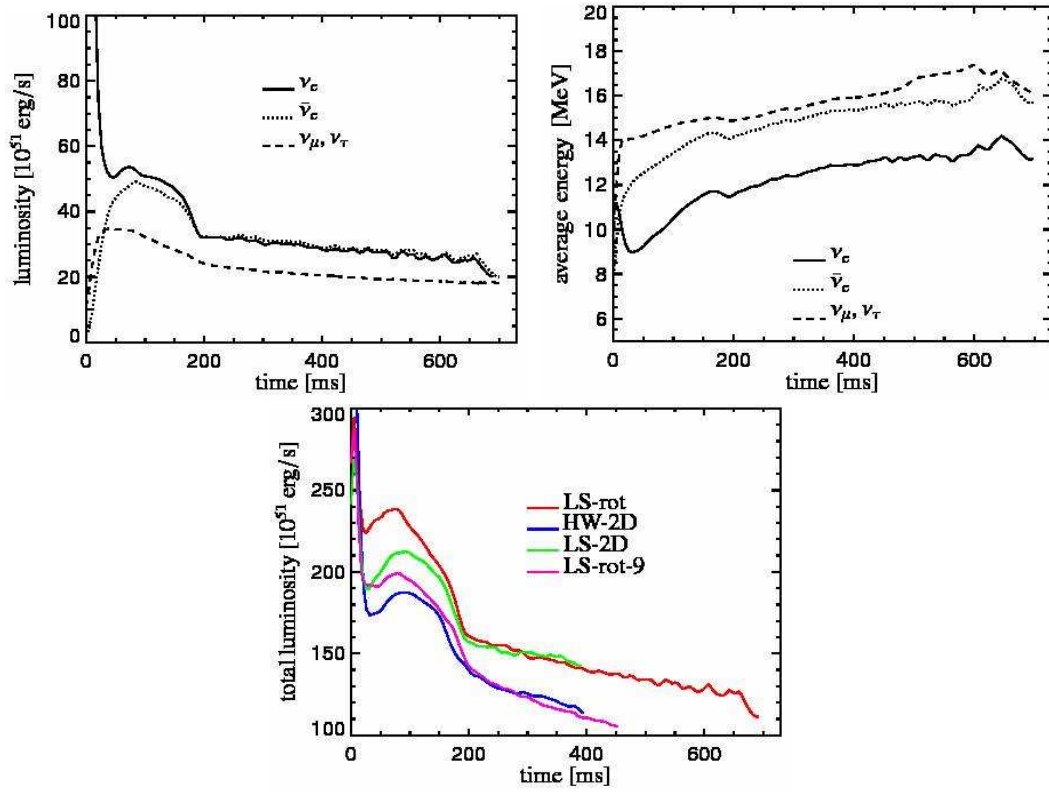


FIG. 14.— Luminosities (*top*) and mean energies (*middle*) of radiated neutrinos in Model M15LS-rot, and total luminosities (summed for neutrinos and antineutrinos of all flavors) for all 2D simulations with the $15 M_\odot$ progenitor (*bottom*) as functions of time after bounce. All quantities are evaluated at a radius of 400 km for an observer in the rest frame of the stellar center, and the average energies are defined as ratio of energy flux to number flux. The decline of the curves near the end of the simulation of Model M15LS-rot signals the onset of the explosion, which leads to reduced accretion luminosities of ν_e and $\bar{\nu}_e$ from the nascent neutron star.

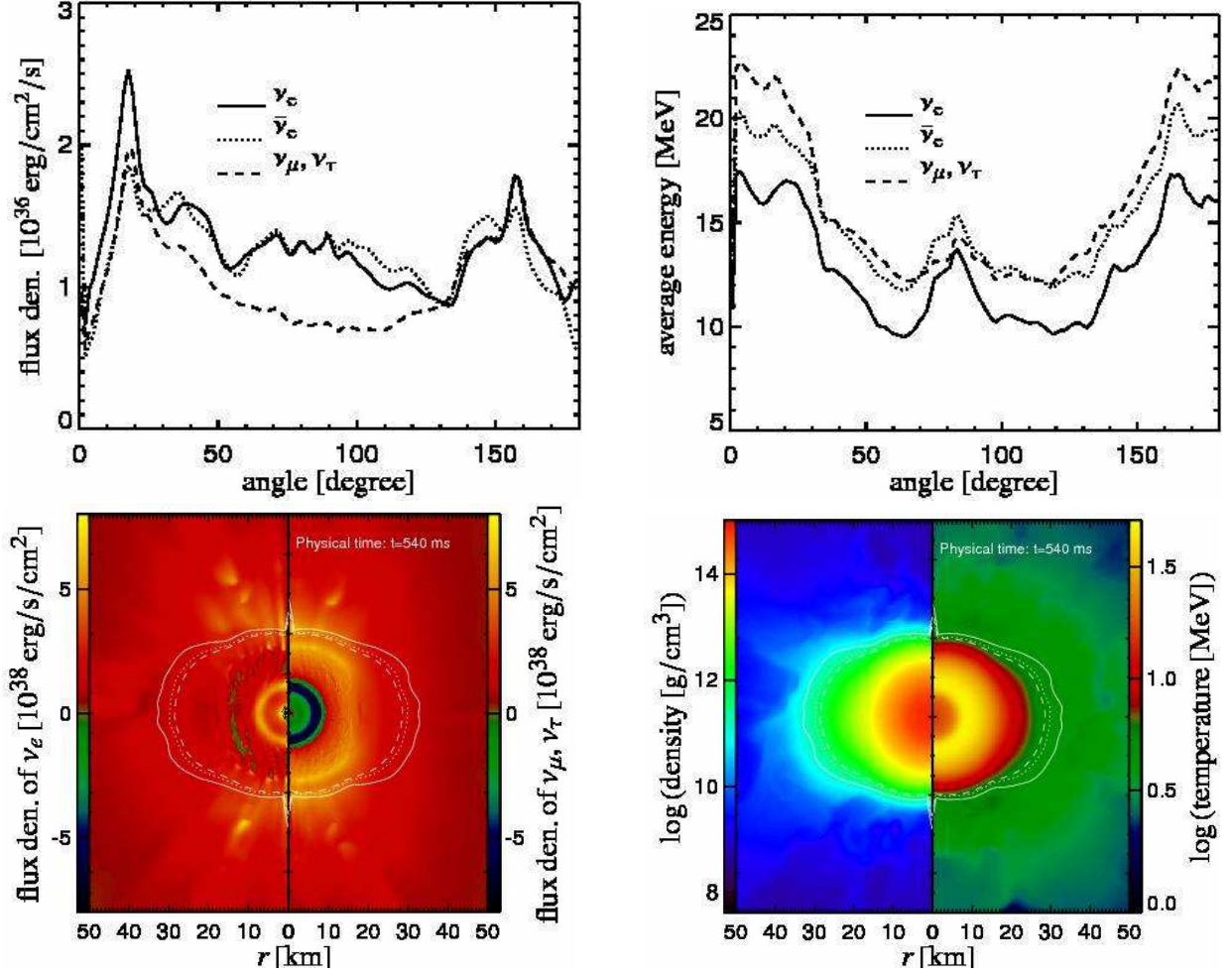


FIG. 15.— *Top:* Neutrino energy flux densities (*left*) and mean energies (*right*) as functions of polar angle at 540 ms after bounce for Model M15LS-rot. The quantities are measured at 400 km and given in the observer frame, and the average energies are defined as ratio of energy flux density to number flux density. *Bottom, left:* Energy flux densities of electron neutrinos and (one kind of) heavy-lepton neutrinos in and around the nascent neutron star. The mean neutrinospheres, which are marked by white lines for ν_e (solid), $\bar{\nu}_e$ (dotted), and ν_μ (dashed), are significantly deformed because of the presence of rotation. *Bottom, right:* Density and temperature in the vicinity of the forming neutron star.

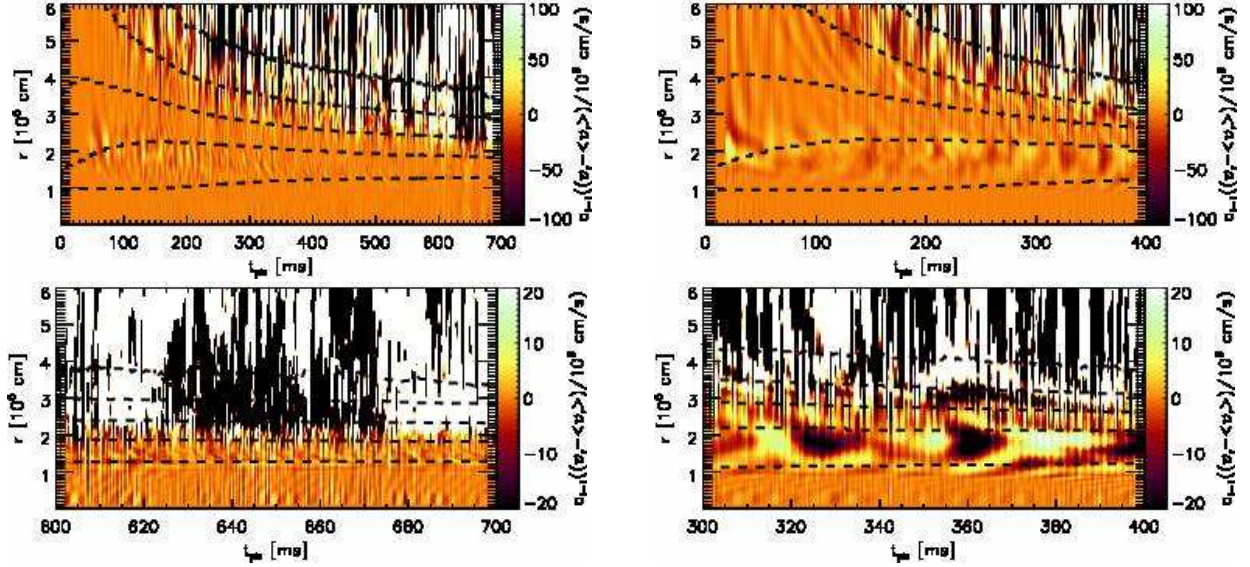


FIG. 16.— Amplitude of the $l = 1$ -mode component of the spherical harmonics decomposition of the velocity variations normalized by 10^6 cm s^{-1} , $(v_r(r, \theta) - \langle v_r(r, \theta) \rangle_\theta) / 10^6 \text{ cm/s}$, as a function of radius and post-bounce time in our simulation of the rotating $15 M_\odot$ model M15LS-rot (left) and in the corresponding simulation without rotation, M15LS-2D (right), once for the whole post-bounce evolution (top) and another time for the last ~ 100 ms of both simulations (bottom). In both cases the central region with a radius of 60 km is shown, but the color scale for the amplitude is constrained to a different range of values (much more narrow than the absolute maxima and minima) in order to visualize activity in different regions. The interior of the neutron star at $r \lesssim 10$ km is much more quiet than the outer layers where SASI and convective motions perturb the surroundings of the proto-neutron star and stir g -mode activity in its surface layers. In particular, there is no sign of any sizable core g -mode oscillations in the neutron star core. The dashed lines mark the positions where the laterally averaged density has values of $\langle \rho \rangle_\theta = 10^{14}$, 10^{13} , 10^{12} , 10^{11} , and $10^{10} \text{ g cm}^{-3}$ (from bottom to top).

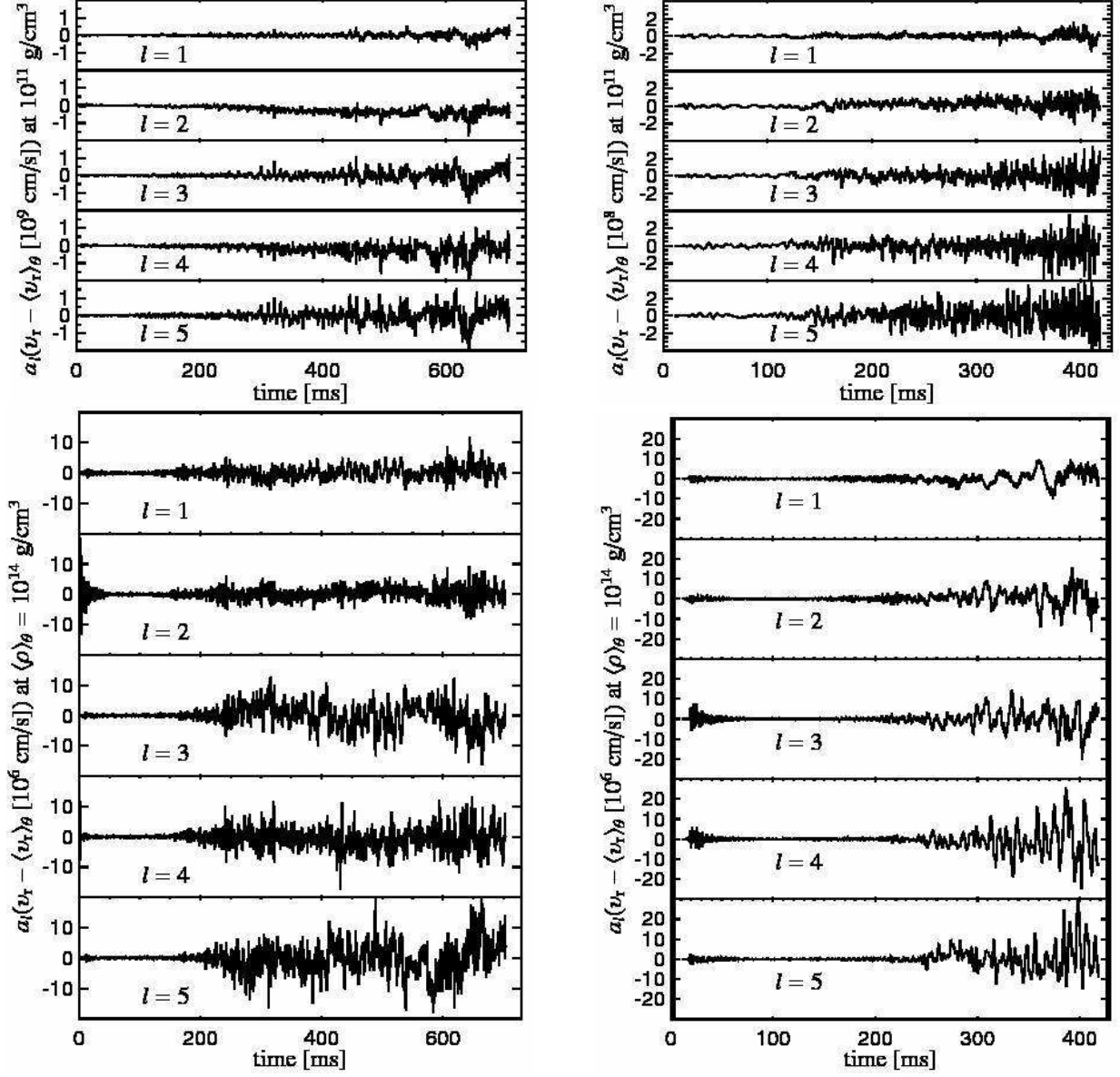


FIG. 17.— Amplitudes of the $l = 1, 2, 3, 4, 5$ -modes of the spherical harmonics decomposition of the velocity variations, $(v_r(r, \theta) - \langle v_r(r, \theta) \rangle_\theta)$, as functions of post-bounce time at fixed values of the laterally averaged density (see the dashed lines in Fig. 16) for our Models M15LS-rot (*left*) and M15LS-2D (*right*). The upper panels show the amplitudes at a density of $\langle \rho \rangle_\theta = 10^{11} \text{ g cm}^{-3}$ with a normalization by 10^9 cm s^{-1} (left) and 10^8 cm s^{-1} (right), the lower panels at $\langle \rho \rangle_\theta = 10^{14} \text{ g cm}^{-3}$ with a normalization by 10^6 cm s^{-1} .

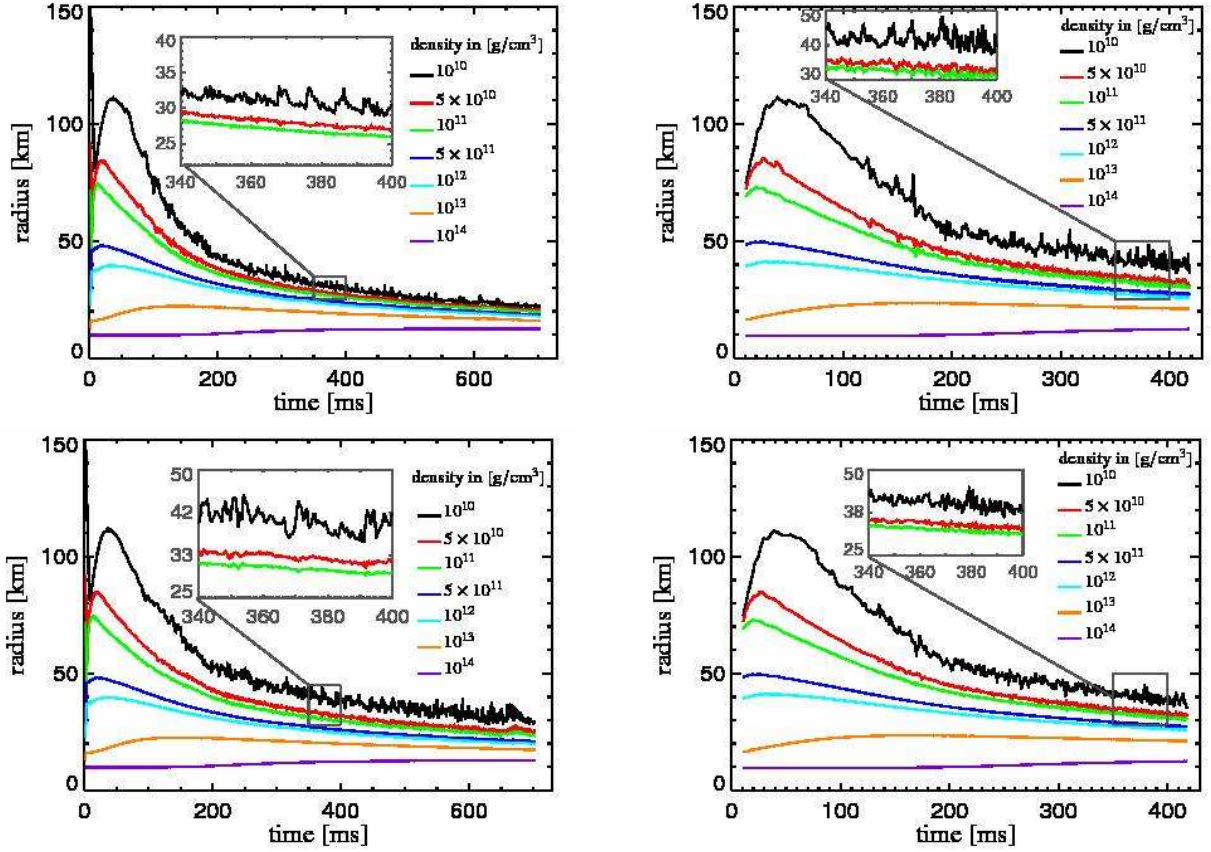


FIG. 18.— Radius variations $r_\rho(t)$ as functions of post-bounce time of the locations for different values of the local density (as specified in the plots) at a position near the pole of the spherical coordinate grid (*upper panels*) and at a latitudinal angle of 45 degrees (*lower panels*) in the nascent neutron star of Model M15LS-rot (*left*) and Model M15LS-2D (*right*). The displayed variations are indicative for major mass motions and mass displacements associated for example with convective overturn or g-mode oscillations. One can see that large amplitudes are present only in the outermost layers of the neutron star at densities below some 10^{10} g cm⁻³ (see also the zoom in the inset), where the violent SASI and convective activity in the postshock layers around the neutron star makes an impact. The interior of the neutron star is essentially quiet, in particular there is no sign of any sizable core g-mode oscillations or pulsational motions of the neutron star core.

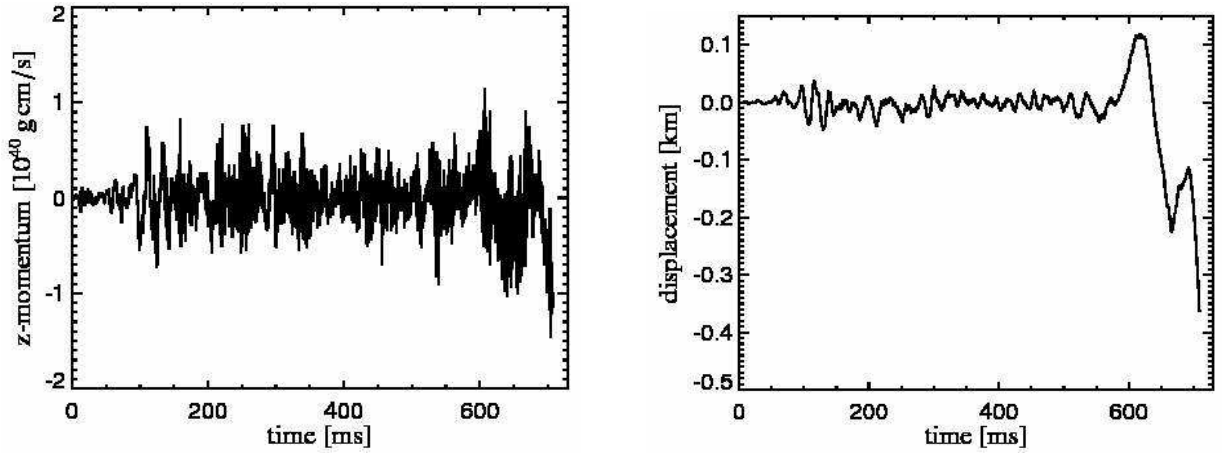


FIG. 19.— Momentum conservation in Model M15LS-rot. The left plot shows the fluctuating total momentum in the direction of the polar (rotation) axis for all gas on the grid, the right plot displays the corresponding displacement of the center of mass from the grid center as function of post-bounce time. Until near the end of the computed evolution, this displacement is far less than the radial width of the innermost grid zone (0.3 km). Only when the postshock gas gains momentum as the explosion takes off, which happens with more strength in the southern hemisphere and thus corresponds to a growing negative momentum value, the z -displacement exhibits a clear trend and becomes slightly larger than the innermost grid zone.

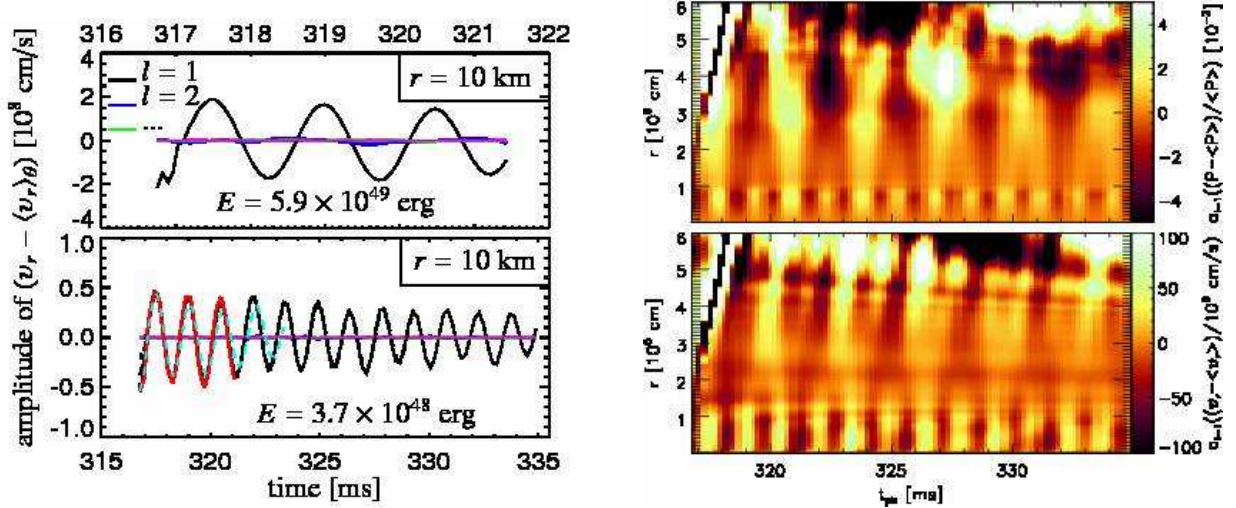


FIG. 20.— *Left:* Test simulations with artificially excited core g-mode oscillations of dipole ($l = 1$) character in the neutron star (here in the case of Model M15HW-2D). Two different amplitudes were considered for an initially imposed velocity field, 5×10^7 cm/s and 2×10^8 cm/s, corresponding to a factor of 16 different kinetic energies (as indicated in the plot). The time evolution of different spherical harmonics components of $(v_r(r, \theta) - \langle v_r(r, \theta) \rangle_\theta)$ is shown at a radius of 10 km. The instigated oscillation remains basically of dipole character. The clear presence of many cycles of the oscillation demonstrates the ability of our numerical code to follow such gravity waves, if they are instigated. In the lower panel three overlapping curves are displayed. The dashed (hardly visible) black line gives the result of a 2D simulation with our standard central 1D-core of $\lesssim 1.7$ km radius, the black solid line is the result with a 1D-core of ~ 0.8 km radius, and the red bold line shows a simulation in which the whole star down to the center was computed in 2D. Neither the frequency nor the amplitude nor the damping behavior are affected by the spherically symmetric treatment of a central region when this 1D core is as small as chosen. Slightly faster damping and a slowly evolving frequency shift are observed when the 1D-core is increased to 3.0 km radius (dashed cyan line). *Right:* The amplitude of the $l = 1$ mode shown in the lower left panel (with a 1D-core radius of 0.8 km) is displayed as a function of time and radius. The upper panel displays the fractional pressure variations (in percent), $(P(r, \theta) - \langle P(r, \theta) \rangle_\theta) / \langle P \rangle_\theta$, the lower panel the velocity variations normalized by 10^6 cm, $(v_r(r, \theta) - \langle v_r(r, \theta) \rangle_\theta) / 10^6$ cm. Note that in both panels the range of values on the color bar is limited (cutting off the true maxima and minima of the amplitudes) for visualizing activity in all regions. Interior to about 10 km the core oscillates with twice the frequency of the mantle outside of $r \approx 25$ km. In the intermediate, convective layer the gravity waves are damped and a frequency change happens. At radii $r \gtrsim 50$ km one can see the presence of gravity waves produced by the violent and chaotic influence of convective overturn and SASI activity in the layers between the neutron star and the shock.